Project Title:	Baltic+ SeaLaBio
Document Title:	Algorithm Theoretical Basis Document (ATBD) V2
Version:	2.4 Final version
Author(s) and affiliation(s):	Constant Mazeran, SOLVO Dagmar Müller, Carole Lebreton, Carsten Brockmann, BC Sampsa Koponen, Jenni Attila, Kari Kallio, Sakari Väkevä, SYKE Thomas Neumann, IOW
Version history:	2.0 Jan 23, 2020. Version for ESA review 2.2 June 22, 2020. Version for ESA review 2.3 Sep 30, 2020. Version for ESA review 2.4 Nov 20, 2020. Final version
Distribution:	Public

Contents

Abstract 4
Glossary 4
List of Symbols 6
1 Introduction 8
2 Algorithm description 9
2.1 Atmospheric correction 9
2.1.1 Processing outline 9
2.1.2 Geometric and spectral processing 9
2.1.3 Data masking 10
2.1.4 Radiance to reflectance conversion 10
2.1.5 Gaseous correction 10
2.1.6 Sun glint correction 11
2.1.7 Rayleigh correction 12
2.1.8 Aerosol correction 12
2.1.9 BRDF normalization 21
2.1.10 Uncertainty 21
2.2 Bio-optical model for the Baltic Sea 23
2.2.1 Parameterization of particulate scattering 26
2.2.2 Parameterisation of detritus absorption 27
2.2.3 Parameterisation of gelbstoff absorption 28
2.2.4 Parameterisation of chlorophyll absorption 28
2.2.5 Finalising the IOP selection 28
2.2.6 Simulations of water leaving reflectances 30
2.2.7 Forward Neural Network 31
2.2.8 Backward NN with minimization on rhow 33
2.3 In-water processing 34
2.3.1 Backward NN with minimization on IOPs 35
2.4 S2 and S3 data merging 36
2.4.1 Synergy approach 36
2.4.2 Algorithm calibration 37
2.4.3 Level-3 generation 38
2.5 BGC model 38
2.5.1 Spatial resolution 39
2.5.2 Explicit CDOM state variable 40
3 Quality assessment and diagnostic 41
3.1 Quality flags 41
3.2 Product uncertainty 42

3.3 BGC model validation 42
4 Scientific analysis 48
4.1 Atmospheric correction 48
4.1.1 OLCI match-ups analysis 48
4.1.2 Representativity of the marine model 48
4.1.3 Chi-square and uncertainty analysis 48
4.1.4 Consistency of Baltic+ AC for S2 55
4.2 Bio-optical model simulations 57
4.2.1 Validating simulation spectra of water leaving reflectance against in-situ spectra 57
4.2.2 Validating the normalisation approach based on simulation data 58
4.3 In-water processing 58
4.4 BGC model 58
5 Practical considerations 60
5.1 Input and output description 60
5.1.1 Atmospheric correction 60
5.1.2 BGC model 60
5.2 Auxiliary data 60
5.2.1 Atmospheric correction 60
5.2.2 BGC model 61
5.3 Software implementation 61
5.3.1 Atmospheric correction 61
5.3.2 BGC model 61
5.4 CPU time 61
5.4.1 Atmospheric correction 61
5.4.2 BGC model 61
6 Assumptions and limitations 62
6.1 Atmospheric correction 62
6.2 BGC model 62
7 References 63

Abstract

This document describes the algorithms developed in WP3 of the Baltic+ SeaLaBio project. It covers four main and sequential parts: the atmospheric correction, the in-water processing, the S2-S3 data merging and the biogeochemical modelling.

Glossary

AC	Atmospheric correction
ADF	Auxiliary Data File
API	Application Programming Interface
ATBD	Algorithm Theoretical Basis Document
BGC	Bio Geo Chemical
BRDF	Bidirectional Reflectance Distribution Function
C2RCC	Care 2 Regional Coast Color
CDOM	Coloured Dissolved Organic Matter
CGT	Code Generation Tool
Chl a	Chlorophyll a
CO2	Carbon dioxide
DOC	Dissolved Organic Carbon
DOM	Dissolved Organic Matter
FUB	Free University of Berlin (EO data processor)
ECMWF	European Centre for Medium-Range Weather Forecasts
EO	Earth Observation
ERGOM	Ecological Regional Ocean Model
ESA	European Space Agency
EUMETSAT	European Organisation for the Exploitation of Meteorological Satellites
FR	Full Resolution (OLCI)
FT	Flow Through
GUM	Guide to the expression of Uncertainty in Measurement
H_2O	Water vapour
HELCOM	Helsinki Commission
HZG	Helmholtz-Zentrum Geesthacht
GEMS	Geostationary Environment Monitoring Spectrometer
GHG	Green-house gas
ICES	International Council for the Exploration of the Sea
IOCS	International Ocean Colour Science meeting
IOP	Inherent Optical Properties
IOW	Leibniz Institute for Baltic Sea Research Warnemünde
LUT	Look-up table
MERIS	Medium Resolution Imaging Spectrometer
MODIS	Moderate Resolution Imaging Spectroradiometer
MOM	Modular Ocean Model
MSI	MultiSpectral Instrument
MTR	Mid Term Review
NCEP	National Centers for Environmental Prediction
NIR	Near infrared
NLLSQ	Non-Linear Least-SQuares
NN	Neural Network
NO_2	Nitrogen dioxide
O3	Ozone
OLCI	Ocean and Land Color Imager
OMI	Ozone Monitoring Instrument (Aura mission)

ONNS	OLCI Neural Network Swarm
PAR	Photosynthetically Active Radiation
POC	Particulate Organic Carbon
POLYMER	POLYnomial based algorithm applied to MERIS
RD	Requirement Baseline Document
RR	Reduced Resolution (OLCI)
SeaLaBio	Sea-Land Biogeochemical linkage
S2	Sentinel-2
S3	Sentinel-3
SAG	Scientific Advisory Group
SNAP	Sentinel Application Platform
SRF	Spectral Response Function
TEMPO	Tropospheric Emissions: Monitoring of Pollution
TOA	Top of Atmosphere
TROPOMI	TROPOspheric Monitoring Instrument
TSM	Total Suspended Matter
WP	Work Package

List of Symbols

Group	Symbol	Definition	Dimension/Unit
wavelength	λ	Wavelength	nm
geometry	θ_s	Solar zenith angle	degrees
	θ_v	View zenith angle	degrees
	μ_s	Cosine of solar zenith angle	dimensionless
	$\Delta\varphi$	Relative azimuth angle	degrees
	M	Air mass fraction (downward + upward)	dimensionless
radiometry	$F_0(\lambda)$	Extraterrestrial Solar irradiance	W m^{-2} nm^{-1} sr^{-1}
	$L_t(\lambda)$	TOA radiance	W m^{-2} nm^{-1} sr^{-1}
	$\rho_a(\lambda)$	Aerosol reflectance, including multiple scattering with Rayleigh	dimensionless
	$\rho_a^{mod}(\boldsymbol{x}_a, \lambda)$	Model of aerosol reflectance as a function of atmospheric unknowns	dimensionless
	$\rho_G(\lambda)$	Sun glint reflectance	dimensionless
	$\rho_{gc}(\lambda)$	TOA reflectance corrected for gaseous absorption and sun glint	dimensionless
	$\rho_{ng}(\lambda)$	TOA reflectance corrected for gaseous absorption	dimensionless
	ρ_{path}	Path reflectance ($\rho_a + \rho_R$)	dimensionless
	$\rho_R(\lambda)$	Rayeigh reflectance (molecular)	dimensionless
	$\rho_{Rc}(\lambda)$	TOA reflectance corrected for gaseous absorption, sun glint and Rayleigh scattering	dimensionless
	$\rho_{Rc}^{mod}(\boldsymbol{x}_a, \boldsymbol{x}_w, \lambda)$	Model of Rayleigh corrected reflectance as a function of atmospheric and marine unknowns	dimensionless
	$\rho_t(\lambda)$	TOA reflectance	dimensionless
	$\rho_w(\lambda)$	Marine reflectance	dimensionless
	$\rho_w^{mod}(\boldsymbol{x}_w, \lambda)$	Model of marine reflectance as a function of marine unknowns	dimensionless
optical thickness	$\tau_{NO2}(\lambda)$	Effective absorption coefficient of NO2 for a unit content	kg^{-1} m^2
	$\tau_{O3}(\lambda)$	Effective absorption coefficient of O_3 for a unit content	kg^{-1} m^2
	$\tau_R(\lambda)$	Rayleigh optical thickness	dimensionless
transmittance	$t(\lambda)$	Total diffuse transmittance, accounting for aerosol and Rayleigh contribution, downward + upward	dimensionless

Group	Symbol	Definition	Dimension/Unit
	$T(\lambda)$	Direct transmittance, accounting for aerosol and Rayleigh contribution, downward + upward	dimensionless
	$t_{H2O}(\lambda)$	H_2O transmittance, downward + upward	dimensionless
	$t_{NO2}(\lambda)$	NO_2 transmittance, downward + upward	dimensionless
	$t_{O3}(\lambda)$	O_3 transmittance, downward + upward	dimensionless
Ancillary data	H_2O	Water vapour content	kg m^{-2}
	NO_2	Dioxide nitrogen content	kg m^{-2}
	O_3	Ozone content	kg m^{-2}
	P	Pressure at sea level	hPa
	w_u	Zonal wind speed	m s^{-1}
	w_s	Longitudinal wind speed	m s^{-1}
Minimization algoritm	c_o, c_1, c_2	Coefficients of POLYMER atmospheric model	dimensionless
	a_φ	Absorption coefficient of phytoplankton pigment	m^{-1}
	a_{det}	Absorption coefficient of detrital particles	m^{-1}
	a_g	Absorption coefficient of yellow substance	m^{-1}
	b_p	Scattering coefficient of particles (non-white)	m^{-1}
	b_w	scattering coefficient of white particles	m^{-1}
	$bwdNN(\boldsymbol{\rho}_w)$	In-water backward NN expressed as a function of a spectral marine reflectance	dimensions of the IOPs
	$fwdNN(\boldsymbol{x}_w)$	In-water forward NN expressed as a function of marine unknowns (IOPs)	dimensionless
	n	number of wavelengths used in the AC inversion	dimensionless
	p	number of degrees of freedom of the AC inversion	dimensionless
	$\boldsymbol{x}_a$	Generic notation for the degrees of freedom of the atmospheric correction related to the atmospheric model	dependent on the exact variables
	$\boldsymbol{x}_w$	Generic notation for the degrees of freedom of the atmospheric correction related to the marine reflectance model	dependent on the exact variables
	$\chi^2(\boldsymbol{x}_a, \boldsymbol{x}_w)$	Cost function of the minimization algorithm as a function of atmospheric and marine unknowns	dimensionless

1 Introduction

This document describes the algorithms developed in WP3 of the Baltic+ SeaLaBio project. It covers four main and sequential parts:

- The atmospheric correction (AC): processing of the satellite data from top-of-atmosphere radiometry to fully-normalized marine reflectance;
- The in-water processing: computation of marine geophysical product from the marine reflectance;
- The S2-S3 data merging: synergetic combination of both missions to extend spatial and temporal range of the EO products;
- The biogeochemical modelling: final processing giving access to the biogeochemical processes in the Baltic Sea (primary production, carbon cycle, linkage with terrestrial loads…)

For each step, this document describes in detail the algorithm: models, data sources, processing steps, output data. A scientific analysis justifies the specific methodology proposed in the project. The requirements on the algorithms were preliminary described in the Requirement Baseline document (RB) and are not further detailed in this ATBD.

This is the version V2.3 of the ATBD including updates made until Sep 30, 2020.

2 Algorithm description

2.1 Atmospheric correction

2.1.1 Processing outline

The computation of marine reflectance from top-of-atmosphere (TOA) radiance requires a number of corrections, the most challenging being associated to the aerosol identification. Each step in the processing outline (Figure 2-1) is described in detail in the following sections.

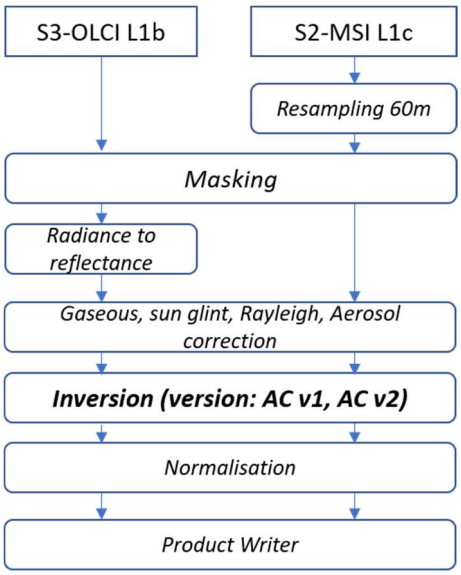

Figure 2-1. Processing outline of the atmospheric correction starting from OLCI L1 and S2-MSI L1c data.

2.1.2 Geometric and spectral processing

OLCI has been specifically designed for ocean colour processing so that its radiometry at pixel level can be used in a straightforward manner in the processing, for a given spatial resolution (Full Resolution, FR or Reduced Resolution, RR) and for all spectral bands, which have a small width. The exact wavelength of each OLCI detector is used in the processing, i.e. there is no "smile correction".

Sentinel-2/MSI, on the other hand, inherits from the Land application and has a different resolution for each band, and also larger bandwidths. The first characteristic requires a data resampling. The choice is made to downsample the MSI radiometry at 60 m resolution. This is done by the SNAP module S2Resampling (resampling with spatial mean for the radiometry, and logical operator "or" for the flags). Regarding spectral resolution, an equivalent wavelength is computed for each band, using MSI spectral response function (SRF). We use the most recent SFRs of S2-A and S2-B provided by ESA on 19 December 2017 (Figure 2-2), ref. COPE-GSEG-EOPG-TN-15-0007 version 3, available online at https://earth.esa.int/web/sentinel/user-guides/sentinel-2-msi/document-library/-/asset_publisher/Wk0TKajiISaR/content/sentinel-2a-spectral-responses. These equivalent wavelengths can then be used in the downstream processing similarly to OLCI for Rayleigh and aerosol correction (monochromatic formulation).

The bands potentially used in the atmospheric correction correspond to bands provided by the forward in-water NN (see section 2.2.6 for more description on the marine radiometric model):

- OLCI: 400, 412, 443, 490, 510, 560, 620, 665, 674, 681, 709, 754, 779, 865, 885, 1020
- MSI: 443, 490, 560, 665, 705, 740, 783, 865

The actual bands selected in the inversion can be a subset, as described hereafter.

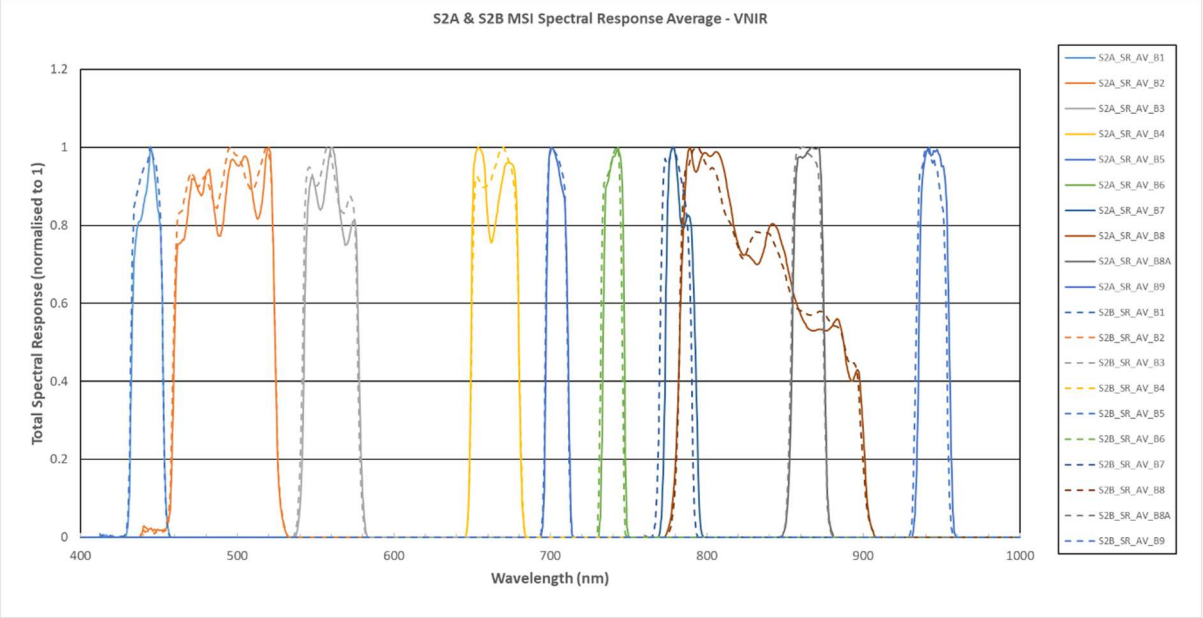

Figure 2-2. S2A and S2B SRF for visible bands from 400 to 1000 nm. Source: ESA file ref. S2-SRF_COPE-GSEG-EOPG-TN-15-0007_3.0.xlsx

2.1.3 Data masking

For OLCI, pixels flagged in the Level1 product as either INVALID, LAND, COASTLINE or BRIGHT are masked and not further processed. To process properly inland waters, systematically flagged as LAND and not WATER in the Level1 product, the LAND mask is actually handled as LAND AND NOT INLAND_WATER.

For MSI, pixels are masked if the radiometry at band B8 (842 nm) is negative or above 0.1.

The IdePix processor provides a dedicated pixel classification for both sensors, which allows to identify e.g. opaque and semitransparent clouds, snow/ice or cloud shadows. It is applied in the AC code, before the identification of the aerosol, and helps to find valid pixels which can be processed successfully.

2.1.4 Radiance to reflectance conversion

The OLCI TOA radiometry, L_t, is converted to reflectance by:

$$\rho_t(\lambda) = \pi \frac{L_t(\lambda)}{\mu_s F_0(\lambda)} \quad (1)$$

Where μ_s is the cosine of the sun zenith angle and F_0 the solar illumination given in the OLCI Level1b product, already corrected for the Earth-sun distance at the acquisition time (see Sentinel-3 OLCI Marine User Handbook, 2018). MSI data are already provided in reflectance values.

2.1.5 Gaseous correction

The TOA reflectance is corrected for absorption of O_2, O_3, NO_2 and H_2O at relevant bands as done in the standard OLCI processing (Fischer et al., 2010):

$$\rho_{ng}(\lambda) = \frac{\rho_t(\lambda)}{t_{O2}(\lambda) * t_{O3}(\lambda) * t_{NO2}(\lambda) * t_{H2O}(\lambda)} \quad (2)$$

Transmittance of O_3 is computed by:

$$t_{O3}(\lambda) = e^{-\tau_{O3}(\lambda) * O3 * M} \quad (3)$$

Where $\tau_{O3}(\lambda)$ is the effective absorption coefficient of ozone for a unit content (1 DU), O_3 is the actual ozone content (in DU; converted from kg/m^2 for OLCI) and M is the total air mass compute by

$$M = \frac{1}{\cos\theta_s} + \frac{1}{\cos\theta_v} \quad (4)$$

Where θ_s and θ_v are the solar and viewing zenith angle, respectively.

Similarly, transmittance of NO_2 is given by

$$t_{NO2}(\lambda) = e^{-\tau_{NO2}(\lambda)*NO2*M} \quad (5)$$

Where $\tau_{NO2}(\lambda)$ is the effective absorption coefficient of nitrogen dioxide for a unit content (1 kg/m^2) and NO_2 a climatological value of nitrogen dioxide content (in kg/m^2) computed per latitude, longitude and day in the year, as tabulated in the operational OLCI Level-2 ground segment (Fischer et al., 2010).

Among the bands currently involved in the AC, only 709 nm is significantly affected by water vapour (H_20). The OLCI water vapour correction, inherited from MERIS, is known to be inaccurate over turbid waters, such as the river estuaries encountered in the SeaLaBio project. The reason is that the correction neglects the albedo of the surface and overestimate the H2O content over bright waters. An alternative computation of H_2O transmittance was proposed by FUB (J. Fischer), based on ancillary data of H2O (ECMWF):

$$t_{H2O}(\lambda) = \sum_{i=1}^{n} w_i e^{-\tau_{H2O,i}(\lambda)*H2O*M} \quad (6)$$

Where w_i are weighting coefficients, $\tau_{H2O,i}(\lambda)$ are effective absorption coefficients of water vapour for a unit content and H_2O the actual water vapour in kg/m^2. These coefficients are all stored in a LUT of early OLCI reprocessing. The advantage of this formulation is to be independent of the surface reflectance, but it has been reported that it could be globally biased (S3-MPC, personal communication). For this reason, it is currently decided to discard 709 nm for OLCI AC (similarly to what does POLYMER). Further inspection beyond the scope of the project would be required with OLCI data to check the problem at 709 nm (comparison between the observed and predicated radiometry) and to see whether this bands could improve the inversion.

Transmittance of O_2 absorption, only relevant for OLCI band 779 nm, is implemented as in the operational ground segment through a Look-up table depending on normalized radiometry at 779, pressure, wavelength and geometry.

The meteorology data (O_3, H_2O) are directly given in OLCI Level1b product (ECMWF data, Sentinel-3 OLCI Marine User Handbook, 2018). For MSI, this data is automatically downloaded from a repository at https://oceandata.sci.gsfc.nasa.gov/Ancillary/Meteorological/ , which provides O_3 data (24h Aura OMI) and water vapour data (6h NCEP). The auxiliary data required by MSI (τ_{O3}, τ_{NO2}) are taken from the OLCI LUTs and interpolated to MSI bands.

2.1.6 Sun glint correction

The sun glint reflectance is corrected through the statistical model of sea surface roughness of Cox and Munk (1954a, 1954b):

$$\rho_{gc}(\lambda) = \rho_{ng}(\lambda) - T(\lambda)\rho_G(w_u, w_v) \quad (7)$$

Where ρ_G is given by the Cox and Munk model for a directional wind speed (w_u, w_v) and T is the direct transmittance (upward and downard). At this stage the aerosol amount is unknown and thus neglected; only the attenuation due to Rayleigh is included:

$$T(\lambda) = e^{-\tau_R(\lambda)*M} \quad (8)$$

Where τ_R is the optical thickness, corrected for pressure (see section 2.1.7).

This correction is known to suffer from inaccurate estimate of the wind speed. Furthermore, the statistical relationship between surface wind and sea roughness might be not applicable s to decameter scales sensor such as

Sentinel-2 (Harmel et al. 2017). It must be seen as a first order correction, and residual sun glint (or overcorrection) is expected to be further handled in the aerosol correction through a spectrally white term, similarly to POLYMER.

2.1.7 Rayleigh correction

Rayleigh correction removes the effect of the air molecules:

$$\rho_{Rc}(\lambda) = \rho_{gc}(\lambda) - \rho_R(\lambda) \quad (9)$$

The Rayleigh reflectance, ρ_R, is interpolated in a pre-computed LUT as a function of geometry and Rayleigh optical thickness. This is a pure Rayleigh computation, without any other atmospheric component. Rayleigh optical thickness is itself corrected for pressure (ratio of actual to standard pressure) and account for the depolarization factor of Bodhaine et al. (1999), with a fixed amount of CO2 of 400 ppm. This correction is in mature state and we do not expect large uncertainties for the ρ_R term. Nevertheless, the Rayleigh LUTs will be checked for the next version of this document. See section 5.2 for more details on the Rayleigh LUT.

2.1.8 Aerosol correction

Aerosol identification and correction is the core of the AC. A key idea of the present approach is that the spectral shape of the aerosol signal is smooth and does not vary as much as the marine spectra. It can be also expressed analytically with strong accuracy (see below). Thus, it should be more robust to obtain ρ_w by removing the aerosol reflectance from the Rayleigh-corrected signal, rather than by a complex non-linear regression with the TOA signal (current end-to-end NN approach of C2RCC). When the aerosol reflectance ρ_a^{mod} is identified in the AC (including the coupling with Rayleigh) as well as the total transmittance t (accounting for the Rayleigh, and ideally including the aerosol contribution), the marine reflectance is computed by:

$$\rho_w(\lambda) = \frac{\rho_{Rc}(\lambda) - \rho_a^{mod}(\lambda)}{t(\lambda)} \quad (10)$$

The challenge of the AC is to distinguish the aerosol and marine signals, especially over the Baltic Sea where both components may have same amplitude (see RB). Aerosol detection relies on a coupled ocean-atmosphere model ρ_{Rc}^{mod}:

$$\rho_{Rc}^{mod}(\boldsymbol{x}_a, \boldsymbol{x}_w, \lambda) = \rho_a^{mod}(\boldsymbol{x}_a, \lambda) + t(\boldsymbol{x}_a, \lambda)\rho_w^{mod}(\boldsymbol{x}_w, \lambda) \quad (11)$$

Where $\boldsymbol{x}_a$ refers to the generic unknowns of the aerosol model and $\boldsymbol{x}_w$ to the unknowns of the marine model.

Aerosol modelling - Two atmospheric models for ρ_a^{mod} have been implemented and tested. First, the model originally developed in POLYMER (Steinmetz et al., 2011), defined with three linear coefficients $\boldsymbol{x}_a = (c_o, c_1, c_2)$

$$\rho_a^{mod}(\lambda) = c_o T(\lambda) + c_1\lambda^{-1} + c_2\rho_R(\lambda) \quad (12)$$

The interest of this model is to represent a large set of aerosols, including the coupling with Rayleigh scattering (Figure 2-3), as well as correcting residual effects for sun glint.

The problem however is that the fitting coefficients have no physical meanings and can vary very much, potentially leading to unrealistic aerosol signal when there is a problem of decoupling with the marine reflectance. For this reason, we have developed and studied another model with physical constraint, based on a Multiple Scattering Approximation (MSA in the following). This model starts from the single scattering reflectanceρ_{as} (Gordon and Wang, 1994):

$$\rho_{as}(\lambda) = \frac{\omega_0(\lambda)\tau_a(\lambda)P(\Theta, \lambda)}{4\cos\theta_s \cos\theta_v} \quad (13)$$

Where ω_0 is the aerosol single scattering albedo and $P(\Theta, \lambda)$ the phase function depending on the scattering angle Θ. We then consider the classical power-law for AOT, with respect to a reference wavelength λ_0:

$$\tau_a(\lambda) = \tau_a(\lambda_0)\left(\frac{\lambda}{\lambda_0}\right)^{\alpha} \quad (14)$$

Assuming that ω_0 and $P(\Theta)$ do not vary spectrally, we have

$$\rho_{as}(\lambda) = c * \left(\frac{\lambda}{\lambda_0}\right)^{\alpha} \tag{15}$$

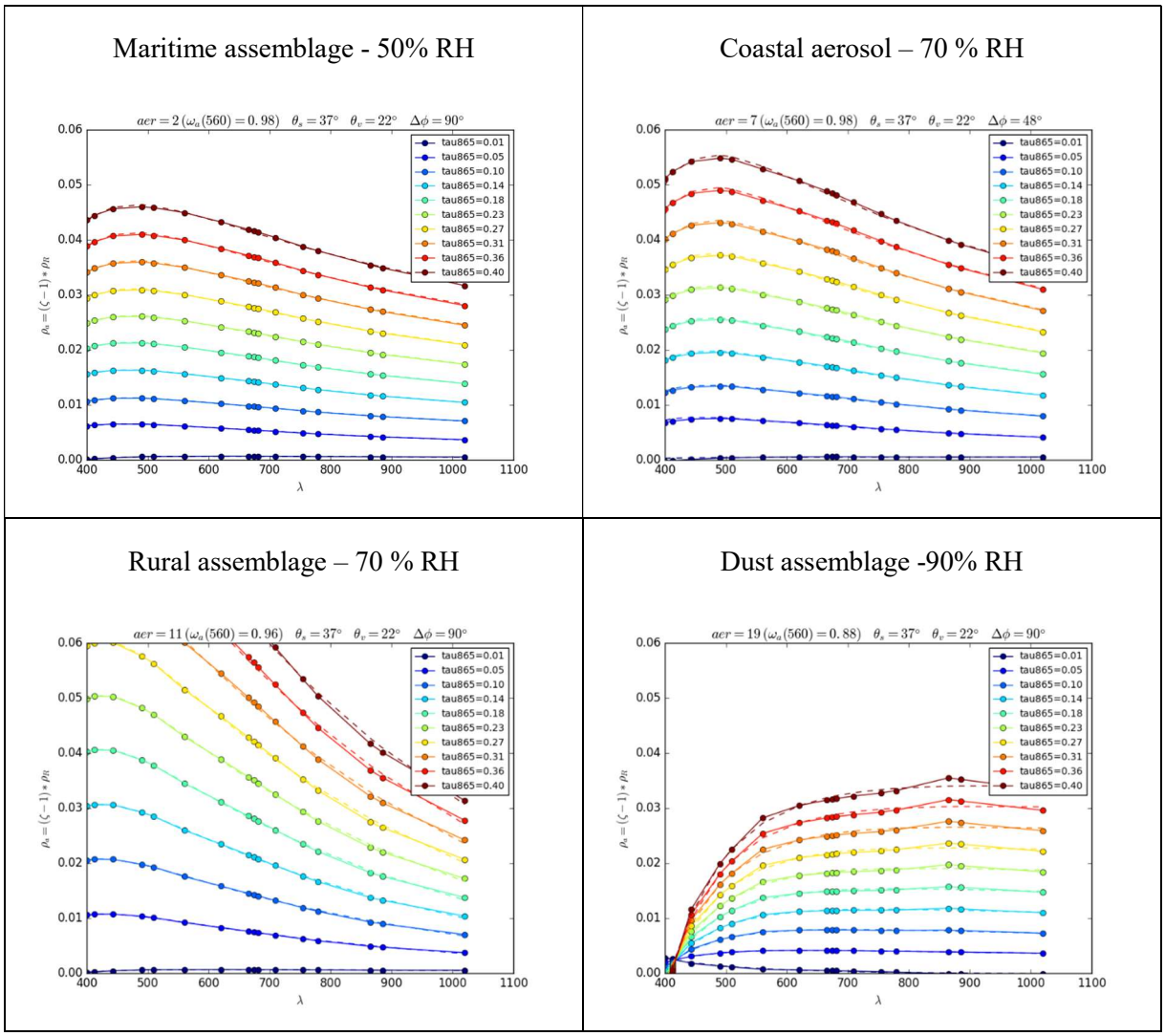

Figure 2-3. Aerosol reflectance ρ_a versus wavelength (solid lines) computed by radiative transfer modelling (OLCI Look-up tables) for four aerosol assemblages (see titles) and various optical thicknesses (colours, see legend). Dashed lines represent the fit by the polynomial shape used in POLYMER. Note that this signal includes coupling with Rayleigh (multiple-scattering).

where c varies pixel-per-pixel as function of geometry, aerosol type (phase function) and AOT. The Multiple Scattering Approximation (MSA) is introduced as a 2nd order relationship between ρ_a and ρ_{as}:

$$\rho_a(\lambda) = a * c * \left(\frac{\lambda}{\lambda_0}\right)^{\alpha} + b * \left(c * \left(\frac{\lambda}{\lambda_0}\right)^{\alpha}\right)^2 \tag{16}$$

where a and b are fitting coefficients depending on the geometry and aerosol model. Using the value $\rho_a(\lambda_0)$, we can rewrite $\rho_a(\lambda)$ as:

$$\rho_a(\lambda)(\lambda) = \rho_a(\lambda_0) * \left(\frac{\lambda}{\lambda_0}\right)^{\alpha} \left(\frac{1 + k * \left(\frac{\lambda}{\lambda_0}\right)^{\alpha}}{1 + k}\right) \quad (17)$$

Where $k = bc/a$. Coefficient k is negative and will adjust for multiple scattering and absorption (decay near blue bands; through term ω_0). With little multiple scattering, k tends towards zero. Assuming the multiple scattering is smaller than the single scattering, its amplitude is lower than unity. The function $\rho_a(\lambda)$ is not monotonous. With $k = 0$ it increases from NIR to blue (single scattering), but in its general form it will decrease from a given wavelength λ_L up to the blue bands. Indeed, the derivative is:

$$\frac{\partial \rho_a(\lambda)}{\partial \lambda} = \frac{\rho_a(\lambda_0)}{1 + k} \frac{\alpha}{\lambda_0} \left(\frac{\lambda}{\lambda_0}\right)^{\alpha} \left(1 + 2k \left(\frac{\lambda}{\lambda_0}\right)^{\alpha}\right) \quad (18)$$

And the optimum is found for λ_L such that $k = -1/2 \left(\frac{\lambda_L}{\lambda_0}\right)^{-\alpha}$. Hence the final formulation of the MSA modelling with λ_L instead of k write:

$$\rho_a^{mod}(\lambda) = \rho_a(\lambda_0) * \left(\frac{\lambda}{\lambda_0}\right)^{\alpha} \left(\frac{1 - \frac{1}{2}\left(\frac{\lambda}{\lambda_L}\right)^{\alpha}}{1 - \frac{1}{2}\left(\frac{\lambda_0}{\lambda_L}\right)^{\alpha}}\right) \quad (19)$$

The three unknowns of the MSA modelling are $\boldsymbol{x}_a = (\rho_a(\lambda_0), \alpha, \lambda_L)$. For most aerosol, with little multiple scattering and absorption, λ_L is close to a wavelength in the blue (where we only observe this decay, still at large AOT). For absorbing aerosol, λ_L goes to the green/red. The important advantage of this modelling compared to POLYMER is that the three unknowns are physically bounded. Taking for instance $\lambda_0 = 865\ nm$, we have:

$$\begin{cases} 10^{-6} < \rho_a(\lambda_0) < 0.08 \\ -2.5 < \alpha < 0.5 \\ 400 < \lambda_L < 600 \end{cases} \quad (20)$$

Although this modelling is based on various approximations, it also perfectly fits the radiative computations

Maritime assemblage - 50% RH	Coastal aerosol – 70 % RH
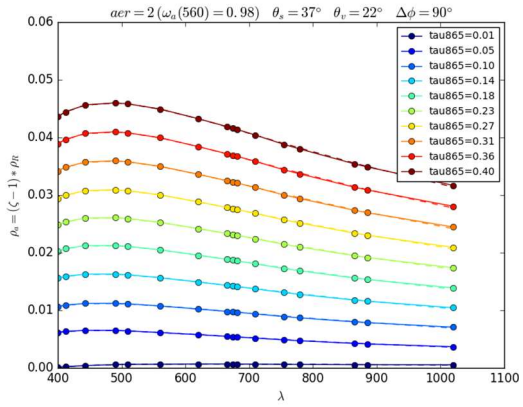	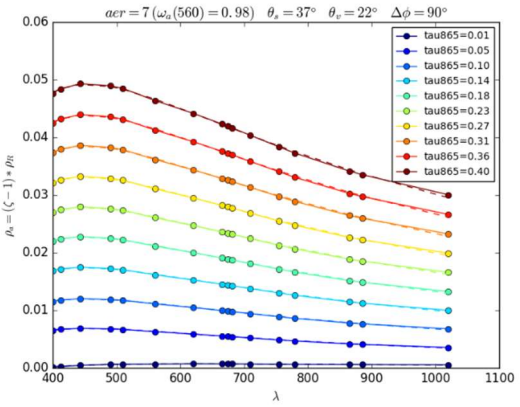
Rural assemblage – 70 % RH	Dust assemblage -90% RH

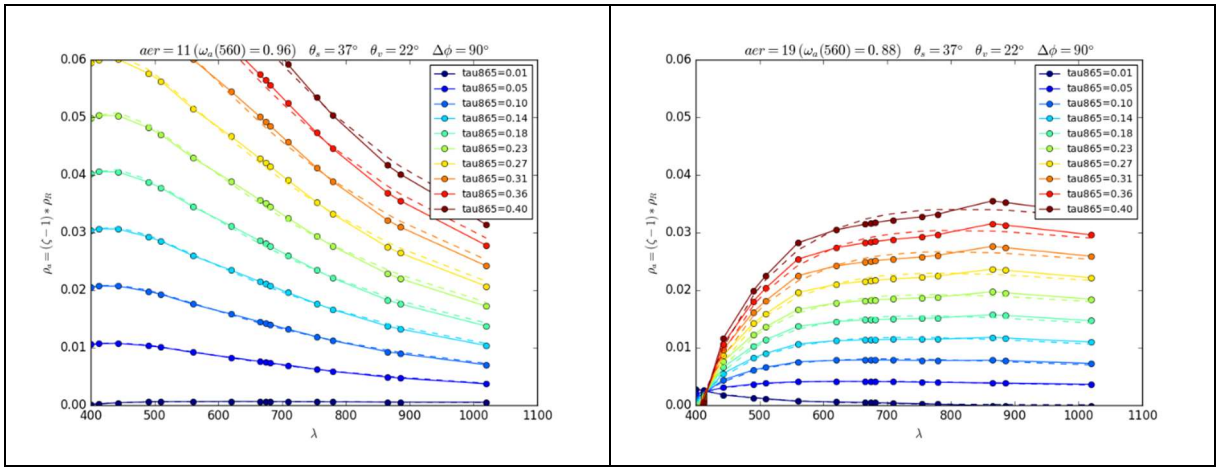

Figure 2-4. Same as Figure 2-3 but for the MSA aerosol model fitting (dashed lines).

A drawback of the MSA approach is however that it requires a non-linear inversion and is much slower than the POLYMER matrix inversion.

The diffuse transmittance t is limited to the Rayleigh contribution and is fixed throughout the AC, as done in POLYMER. The difficulty is that the functional description of ρ_a^{mod} through a polynomial does not give direct access to the physics of the aerosol. A further difficulty is that this term may include surface effects independent of the aerosol (residual glint). Outside the glint, an option could be to compare ρ_a^{mod} to a database of radiative transfer simulation (e.g. OLCI LUTs), identify the best model aerosol model and optical thickness, and compute a more realistic value of t through other LUTs of total transmittance. The impact of this simplified transmittance on the final marine reflectance is not straightforward but may be limited due to uncertainties compensation. Indeed, the same transmittance is used in the final computation of ρ_w, see Eq. (10), and in the computation of ρ_a through the spectral fit of $\rho_{Rc} - t\rho_w^{mod}$. The uncertainty analysis of section 2.1.10 can theoretically handle the uncertainty of t and potential compensation through covariances between t and ρ_a. Currently, the results of the Baltic+ AC do not suggest to further improve this modelling.

Marine model - The marine model ρ_w^{mod} is described by an in-water forward neural network (NN), where the degrees of freedom are given by five IOPs:

$$\boldsymbol{x}_w = \left(a_\varphi, a_{det}, a_g, b_p, b_w\right) \tag{21}$$

where a_φ, a_{det}, and a_g are the absorption coefficients for phytoplankton, detrital matter and gelbstoff (yellow substance), respectively, and b_p and b_w are the scattering coefficients for non-white and white particulates, respectivelly. These coefficients are all defined at a given reference band, here omitted to simplify the notation of the AC, and their spectral variations are fixed in the NN modelling. This model depends also on other known parameters (geometry, temperature, salinity) which are omitted in the following, so that the marine reflectance is computed formally as:

$$\rho_w^{mod}(\lambda) = fwdNN(\boldsymbol{x}_w) \tag{22}$$

Spectral matching - The inversion of the unknown variables $(\boldsymbol{x}_a, \boldsymbol{x}_w)$ consists in minimizing the discrepancy between the observation, ρ_{Rc}, and the model ρ_{Rc}^{mod}, over a set of n wavelengths $\lambda_1 \cdots \lambda_n$ by non-linear least-squares (NLLSQ):

$$\chi^2(\boldsymbol{x}_a, \boldsymbol{x}_w) = \frac{1}{n-p}\sum_{i=1}^{n} \frac{\left(\rho_{Rc}^{mod}(\boldsymbol{x}_a, \boldsymbol{x}_w, \lambda_i) - \rho_{Rc}(\lambda_i)\right)^2}{var\left(\rho_{Rc}^{mod}(\lambda_i)\right) + var\left(\rho_{Rc}(\lambda_i)\right)} \tag{23}$$

This χ^2 is scaled by the number of degrees of freedom $(n-p)$, which does not change the minimization itself but is used further to compute uncertainties. It should be noted that the cost function corresponds also to the residual between the modelled and retrieved marine signal at TOA, since by Eq (10) one has $\rho_{Rc}^{mod} - \rho_{Rc} = t\rho_w^{mod} - t\rho_w$.

As shown above, the spectral shape of the aerosol signal is smooth and does not vary as much as the marine spectra. It can be also expressed analytically with strong accuracy. Thus, it should be more accurate to obtain ρ_w by removing the path reflectance from the TOA signal, rather than by a complex non-linear regression with the TOA signal (current end-to-end NN approach used by default). Hence at convergence of the minimization process, the final marine reflectance is given by

$$\rho_w(\lambda) = \frac{\rho_{RC}(\lambda) - \rho_a^{mod}(\boldsymbol{x}_a, \lambda)}{t(\boldsymbol{x}_a, \lambda)} \quad (24)$$

In this equation the marine unknown $\boldsymbol{x}_w$ does not appear, although it is linked to $\boldsymbol{x}_a$ retrieved in the same optimization process. In fact, this ρ_w combines $\rho_w^{mod}(\boldsymbol{x}_w)$ and the residual of the minimization:

$$\rho_w(\lambda) = \rho_w^{mod}(\boldsymbol{x}_w, \lambda) + res(\lambda) \quad (25)$$

Assigning the residual to ρ_w rather than to ρ_a is important because the marine signal is much more variable in shape, by nature. This lets a chance to retrieve spectra not represented by the initial in-water training.

This cost function χ^2 takes into account the squared uncertainties of the model and of the observation, through $var(\rho_{Rc}^{mod})$ and $var(\rho_{Rc})$, respectively. If the uncertainties are not assigned (current version), the denominator is simply set to one (no spectral weighting). The chi-square is also normalized by the number of degrees of freedom, $n - p$, where p is the number of independent unknowns. This normalization does not impact the minimization process but gives an insight on the performance of the spectral fitting: the χ^2 should be lower than unity for a successful inversion.

The bands chosen in the χ^2 are essentially driven by the availability of the forward model to provide realistic reflectance and the trustiness of the input ρ_{RC} signal. For OLCI, 709 is removed as explained previously due to dubious water vapour correction and because fluorescence is not included in the NN simulations (yet, after the atmosphere is identified, the correction is done to provide ρ_w at that band). Also, 1020 nm is removed because of dubious calibration at TOA (between 5 and 10%). For MSI, the number of bands is limited, so all bands available in the NN between the blue and NIR are selected. Hence, 14 bands are used for OLCI and 8 for MSI:

- OLCI: 400, 412, 443, 490, 510, 560, 620, 665, 674, 681, 754, 779, 865, 885
- MSI: 443, 490, 560, 665, 705, 740, 783, 865

The direct minimization of the chi-square function for eight unknowns (three for $\boldsymbol{x}_a$ and five for $\boldsymbol{x}_w$) is numerically complex. To decrease the dimensionality of the problem, an iterative approach is proposed, decoupling the inversion in the marine and atmospheric unknowns. Two versions are proposed (Figure 2-5) and described hereafter.

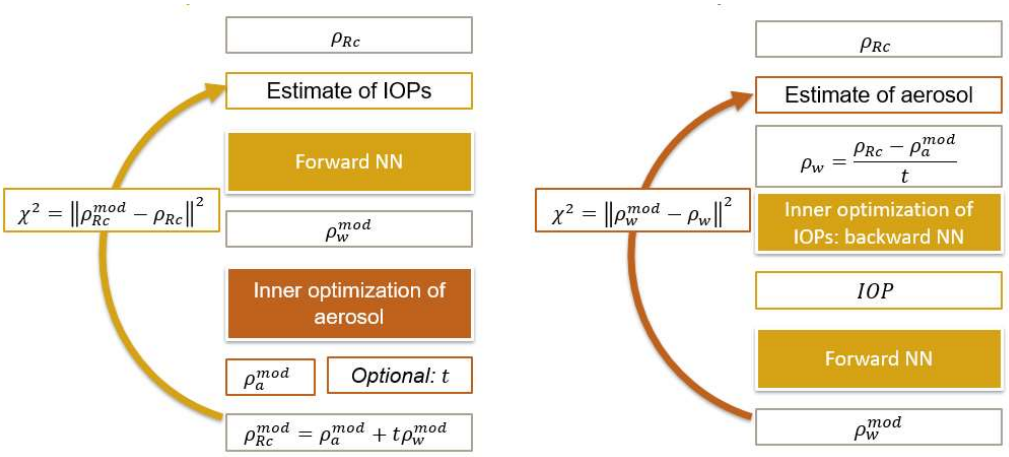

Figure 2-5. Numerical methods for the aerosol detection. Left: inversion using the forward in-water NN (used in Baltic+ results); right: inversion using the backward in-water NN (investigated, not used in Baltic+ results).

Inversion using forward in-water NN (AC currently used in Baltic+ results)

This method iterates over a set of IOPs ($\boldsymbol{x}_w$), to identify the best match at the TOA level (Figure 2-5, left). It is formally analogous to POLYMER, except that the marine model is expressed through a NN. For a given $\boldsymbol{x}_w$, the forward NN computes ρ_w^{mod}. Given this marine signal, and a first estimate of the transmittance (see below) limited to the Rayleigh contribution, the best aerosol reflectance ρ_a^{mod} is deduced (i.e. best $\boldsymbol{x}_a$), by fitting the polynomial against $\rho_a = \rho_{Rc} - t\rho_w^{mod}$. When taking the POLYMER formulation with $\boldsymbol{x}_a = (c_o, c_1, c_2)$, the spectral fitting writes as an overdetermined linear system ($n > 3$):

$$\Lambda \begin{pmatrix} c_0 \\ c_1 \\ c_2 \end{pmatrix} = \begin{pmatrix} \rho_a(\lambda_1) \\ \vdots \\ \rho_a(\lambda_n) \end{pmatrix} \quad \text{where } \Lambda = \begin{pmatrix} T(\lambda_1) & {\lambda_1}^{-1} & \rho_R(\lambda_1) \\ \vdots & \vdots & \vdots \\ T(\lambda_n) & {\lambda_n}^{-1} & \rho_R(\lambda_n) \end{pmatrix} \tag{26}$$

The optimal solution in least-square sense is given by introducing the pseudo-inverse matrix of Λ:

$$\begin{pmatrix} c_0 \\ c_1 \\ c_2 \end{pmatrix} = (\Lambda'\Lambda)^{-1}\Lambda' \begin{pmatrix} \rho_a(\lambda_1) \\ \vdots \\ \rho_a(\lambda_n) \end{pmatrix} \tag{27}$$

When taking the MSA formulation, we resolve $\boldsymbol{x}_a = (\rho_a(\lambda_0), \alpha, \lambda_L)$ by a curve fitting algorithm with bounded constraints (the Trust Region Reflective method, Branch et al., 1999), starting from $\boldsymbol{x}_a = (0.005, -1{,}443)$ and the bounds given in Eq 20.

The retrieved $\boldsymbol{x}_a$ is then used to reconstruct the modelled TOA signal through Eq. (11), ρ_{Rc}^{mod}, to be compared to the observation ρ_{Rc}. The aerosol unknown $\boldsymbol{x}_a$ is thus seen as an intermediate variable, depending on $\boldsymbol{x}_w$. The χ^2 is also only written as a function of $\boldsymbol{x}_w$. The minimization is achieved with the Nelder-Mead algorithm (Nelder and Mead, 1965), using only evaluations of the χ^2 for various sets of $\boldsymbol{x}_w$. The method is based on the concept of simplex, i.e. the simplest multidimensional polytope made of l+1 vertices for a minimisation problem in dimension l. The cost function is evaluated on the initial vertices of the simplex, and the algorithm iteratively transforms the worst vertex (highest cost function) through a series of transformation (reflection, expansion, contraction) or possibly transforms the whole simplex (shrink), see Figure 2-6. The initial simplex is here given by a first vertex (first guess in $\boldsymbol{x}_w$), and l other vertices by a variation of step +2% in each dimension. The first guess comes from application of the backward NN directly on ρ_{Rc}.

Although widely used in science, the NM algorithm has little theoretical foundation and convergence property, except in small dimension (Lagarias et al., 1998). In POLYMER, there are 2 marine unknowns and a maximum of 100 iterations is allowed. In the present case, there are 5 marine unknowns. When dimension is growing, it is known that the rate of convergence may strongly deteriorate (Han et al., 2006). A heuristic approach is to restart the algorithm several times while keeping a few iterations per run. Convergence over some pixels may be relatively fast (100 iterations), but other slower. For OLCI, a total of 300 iterations have been split into 30 main NM runs (i.e. 30 restarts) of 10 iterations each. For MSI, whose processing is longer due to the increased number of pixels despite the TensorFlow package, the number of iterations has been reduced to 100 (10 restarts of 10 iterations) without showing degradation.

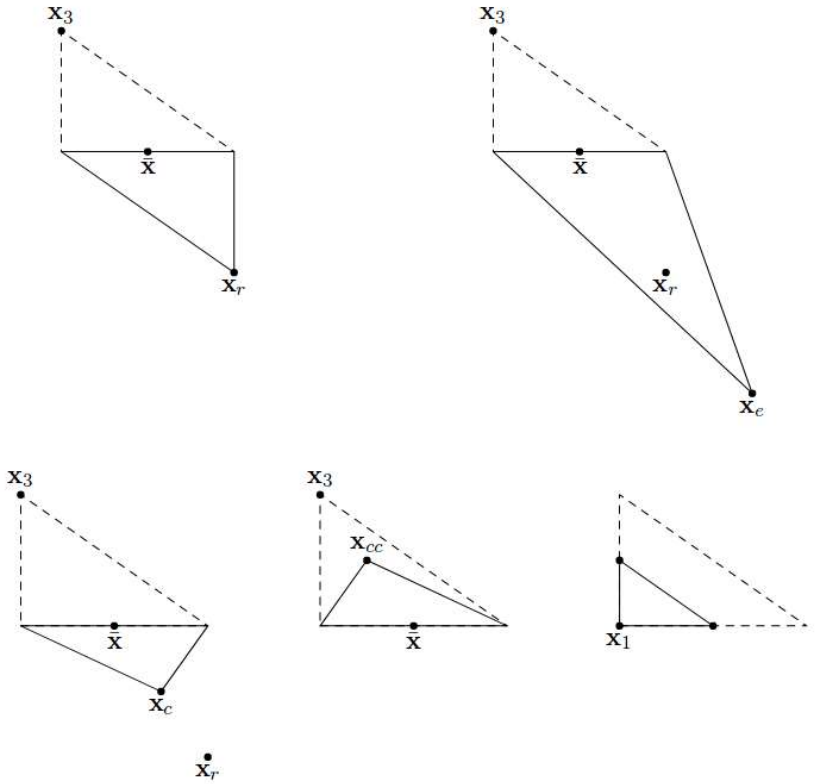

Figure 2-6. Nelder-Mead transformations in dimension 2. The initial simplex is in dashed line with best vertex x_1 and worst vertex x_3. Top-left: reflection; top-right: extension; bottom left: external contraction; bottom middle: internal contraction; bottom right: shrink. From Lagarias et al. (1998).

The AC implemented in Baltic+ is based on this formulation and the POLYMER atmospheric modelling. The interest of this approach is to require only a forward model for the marine part, and a direct inversion of the atmospheric unknowns faster than any iterative algorithm (matrix product). In practice, the forward NN is launched with the TensorFlow library, extremely fast to process the full image at once (at least for OLCI images). Similarly, the linear algebra for the aerosol term can be applied simultaneously on all pixels (Einstein summation in Python). To benefit from this global processing, the Nelder-Mead algorithm has been fully recoded with capability to optimize all pixels simultaneously: the forward model and χ^2 are not computed iteratively on each pixel (Figure 2-7, left), but only once on the full image, for the required transformations of the relevant vertices (Figure 2-7, right). This procedure is mathematically equivalent to the per-pixel case, i.e. each pixel has its own simplex transformed independently of the other pixels, and is extremely fast.

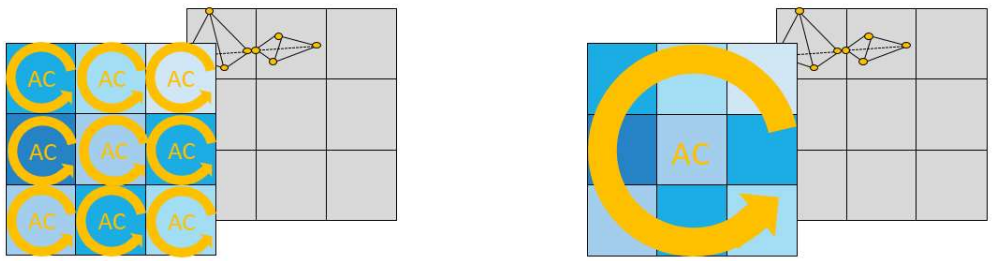

Figure 2-7. Symbolic representation of the NM implementation requiring the launch of AC either on each single pixel (left) or on the full image (right).

Inversion using backward in-water NN (AC investigated, currently not used in Baltic+ results)

The logic of this method is the opposite of the previous one: for a given aerosol content modelled through $\boldsymbol{x}_a$, the marine reflectance ρ_w can be directly retrieved by applying Eq (10). The best $\boldsymbol{x}_a$ is supposed to be the one for which ρ_w best follows to the marine model ρ_w^{mod} (i.e. there exists an optimal $\boldsymbol{x}_w$ able to reproduce ρ_w). The iteration thus runs over $\boldsymbol{x}_a$, and $\boldsymbol{x}_w$ is simply an intermediate variable given by the backward in-water NN:

$$\boldsymbol{x}_w = bwdNN(\boldsymbol{\rho}_w) \tag{28}$$

The interest of this procedure is that the overall iteration involves lower dimensionality (three instead of five). The price is the use of the backward NN.

The training of the backward NN is achieved over a large set of simulated pairs $\left(\boldsymbol{x}_w^{sim}, \boldsymbol{\rho}_w^{sim}\right)$ where $\boldsymbol{\rho}_w^{sim}$ come from a model: $\boldsymbol{\rho}_w^{sim} = \boldsymbol{\rho}_w^{mod}\left(\boldsymbol{x}_w^{sim}\right)$. Currently the in-water NN is trained such that it minimizes the difference between its output $\boldsymbol{x}_w = bwdNN\left(\boldsymbol{\rho}_w^{sim}\right)$ and the actual $\boldsymbol{x}_w^{sim}$, over all cases. An issue is that different concentrations of a marine component may lead to same ρ_w at a given band (saturation effect) and furthermore different set of IOPs $\boldsymbol{x}_w$ may lead to same spectrum $\boldsymbol{\rho}_w$ (masking effect, see Figure 2-8).

It follows that the training is impacted by ambiguities (non-univocal link between the free parameters $\boldsymbol{x}_w$ and $\boldsymbol{\rho}_w$) whereas atmospheric correction only requires a realistic spectrum $\boldsymbol{\rho}_w$, whatever the IOPs, to be decoupled with the atmospheric path reflectance. We thus propose to train the backward NN with a cost function defined in term of marine spectrum, i.e.:

$$\boldsymbol{\rho}_w^{sim} \rightarrow\ bwdNN\left(\boldsymbol{\rho}_w^{sim}\right) = \boldsymbol{x}_w \text{ such that } \boldsymbol{x}_w = \underset{\boldsymbol{x}_w}{\operatorname{argmin}} \left\| fwdNN(\boldsymbol{x}_w) - \boldsymbol{\rho}_w^{sim} \right\|^2 \tag{29}$$

Where the squared norm $\| \quad \|^2$ represents a quadratic summation over all wavelengths and all cases, with inputs defined either in linear or logscale and possibly normalised to their min/max range. Such new training ensures that the NN fits optimally to the input spectrum $\boldsymbol{\rho}_w$, whatever the underlying IOPs. Minimisation of the marine reflectance residual, instead of the IOPs residual, is an important property used in this AC v2. To understand this aspect, the cost function is rewritten in term of marine reflectance, to distinguish the atmospheric and marine parameters:

$$\chi^2(\boldsymbol{x}_a, \boldsymbol{x}_w) = \left\| \boldsymbol{\rho}_w^{mod}(\boldsymbol{x}_w) - \frac{\boldsymbol{\rho}_{RC} - \boldsymbol{\rho}_a^{mod}(\boldsymbol{x}_a)}{\boldsymbol{t}(\boldsymbol{x}_a)} \right\|^2 \tag{30}$$

By definition of the new in-water backward NN constructed as an optimal interpolator, for any marine spectra $\boldsymbol{\rho}_w$ and any $\boldsymbol{x}_w$ the following inequality applies:

$$\left\| \boldsymbol{\rho}_w^{mod}\left(bwdNN(\boldsymbol{\rho}_w)\right) - \boldsymbol{\rho}_w \right\|^2 \leq \left\| \boldsymbol{\rho}_w^{mod}(\boldsymbol{x}_w) - \boldsymbol{\rho}_w \right\|^2 \tag{31}$$

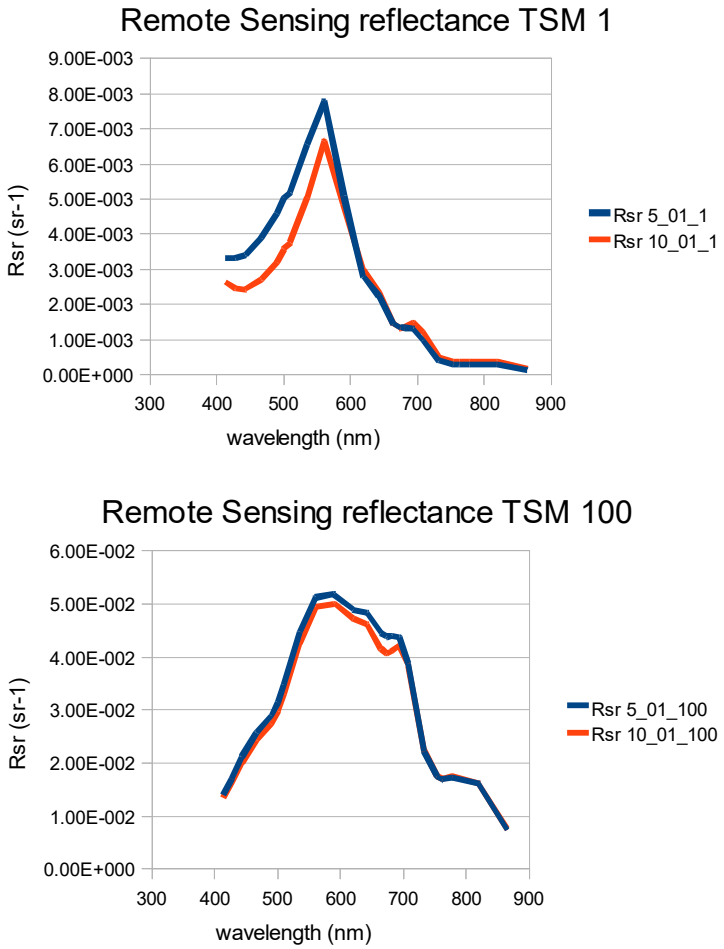

Figure 2-8. Masking effect: both plots show two different surface reflectance spectra for two chlorophyll concentrations of 5 and 10µg/m³, but for a TSM concentration of 1 mg/m³ (top) and for 100 mg/m³ (bottom). The high TSM is masking the changes in Chl.

If we apply this inequality for $\boldsymbol{\rho}_w$ defined above, we have:

$$\left\| \boldsymbol{\rho}_w^{mod}\left(bwdNN\left(\frac{\boldsymbol{\rho}_{RC} - \boldsymbol{\rho}_a^{mod}(\boldsymbol{x}_a)}{\boldsymbol{t}(\boldsymbol{x}_a)} \right) \right) - \frac{\boldsymbol{\rho}_{RC} - \boldsymbol{\rho}_a^{mod}(\boldsymbol{x}_a)}{\boldsymbol{t}(\boldsymbol{x}_a)} \right\|^2 \leq \chi^2(\boldsymbol{x}_a, \boldsymbol{x}_w) \tag{32}$$

This is true for any $(\boldsymbol{x}_a, \boldsymbol{x}_w)$ and demonstrates that minimizing the cost function in the $(\boldsymbol{x}_a, \boldsymbol{x}_w)$ plane is achieved by minimising the left hand-side term in the $\boldsymbol{x}_a$ dimension only:

$$\chi^2_{atm}(\boldsymbol{x}_a) = \left\| \boldsymbol{\rho}_w^{mod}\left(bwdNN\left(\frac{\boldsymbol{\rho}_{RC} - \boldsymbol{\rho}_a^{mod}(\boldsymbol{x}_a)}{\boldsymbol{t}(\boldsymbol{x}_a)} \right) \right) - \frac{\boldsymbol{\rho}_{RC} - \boldsymbol{\rho}_a^{mod}(\boldsymbol{x}_a)}{\boldsymbol{t}(\boldsymbol{x}_a)} \right\|^2 \tag{33}$$

Hence an iterative spectral matching approach on $\boldsymbol{x}_a$ can theoretically solve the problem. To summarise, the AC v2 writes:

i. Start from a first guess of $\boldsymbol{x}_a$ (for instance through average value of AOT and Angstrom coefficient)
ii. Iterate on $\boldsymbol{x}_a$ to minimize the cost function χ^2_{atm} define as:
    a. Translate if necessary $\boldsymbol{x}_a$ in physical atmospheric property to compute and $\boldsymbol{t}(\boldsymbol{x}_a)$
    b. Compute $\boldsymbol{\rho}_w = \frac{\boldsymbol{\rho}_{RC} - \boldsymbol{\rho}_a^{mod}(\boldsymbol{x}_a)}{\boldsymbol{t}(\boldsymbol{x}_a)}$

c. Apply the in-water backward NN: $\boldsymbol{x}_w = bwdNN\left(\frac{\boldsymbol{\rho}_{RC}-\boldsymbol{\rho}_a^{mod}(\boldsymbol{x}_a)}{\boldsymbol{t}(\boldsymbol{x}_a)}\right)$
d. Estimate marine reflectance by the in-water forward NN: $\boldsymbol{\rho}_w^{est} = fwdNN(\boldsymbol{x}_w)$
e. Compute $\chi^2_{atm} = \|\boldsymbol{\rho}_w^{est} - \boldsymbol{\rho}_w\|^2$

iii. Stop on convergence criterion (number of iterations, threshold on cost function)
iv. Return $\boldsymbol{\rho}_w$ (main output) and $\boldsymbol{x}_w$ (estimate of in-water properties, to be used as downstream products)

Improved robustness is expected thanks to robustness of the in-water NN itself and the optimization of $\boldsymbol{x}_a$ limited to a 3-dimensional space. When considering the MSA aerosol model, the optimization is conducted as previously with bounded-constraints.

A crucial assumption of this AC is that the forward and backward NNs are reciprocal, see Eq (29). It has been checked that it is not the case of current NNs and this explains current issues in the optimization process. Investigation of so-called invertible neural network is on-going and will be tested when ready

2.1.9 BRDF normalization

The non-isotropy of the upward radiance field emerging from the ocean with respect to the sun and observation geometries is characterized by the Bidirectional Reflectance Distribution Function (BRDF; see e.g. Morel et al. 2002). Because the amplitude of BRDF effects can be largely above the specified accuracy of remote-sensing reflectance (uncertainty of 5%), a correction is required to allow comparison with in-situ data and merge spectra of various sensors.

During radiative transfer modelling, a wide range of geometries has been calculated for each combination of IOPs, including the fully normalized condition (sun at zenith, nadir view). A neural network has been trained with these spectra, so that from a given geometry and spectrum the normalized spectrum can be derived. The normalization NN requires log-transformed spectra. This is a limitation when the reflectance is negative at one or several bands. In such a case, the negative marine reflectances are constrained to the lower limit of the trainings range of the NN. Afterwards log-transformation is possible and the spectra can be normalized. This procedure should not introduce a bias when the signal is effectively very low, like in the blue or in the NIR bands for absorbing waters.

An alternative solution not using the normalization NN consists in taking the IOPs as determined by the AC, $\boldsymbol{x}_w$, and launch the foward NN in two geometries (actual, and normalized geometry with all angles set to zero) to get the BRDF factor:

$$\rho_{wN}(\lambda) = \left(\frac{\rho_w^{mod}(\boldsymbol{x}_w, \lambda, 0, 0, 0)}{\rho_w^{mod}(\boldsymbol{x}_w, \lambda, \theta_s, \theta_s, \Delta\varphi)}\right) * \rho_w(\lambda) \quad (34)$$

This approach is physically based and much easier to implement, since it does not need to train a normalization NN every time a new forward NN is designed. It also keep any residual in the ρ_w that would not be modelled by the NN. The Baltic+ normalization is currently based on this solution.

2.1.10 Uncertainty

Our uncertainty estimate relies on the Quality Assurance framework for Earth Observation (QA4EO; Fox, 2010), providing a clear framework for uncertainty propagation in remote-sensing data and based on the GUM: Guide to the expression of Uncertainty in Measurement (JCGM, 2008). In this formalism, our main measurement (or calculation) equation is given Eq.(10), which can be rewritten in a vector notation for the spectral dimension:

$$\boldsymbol{\rho}_w = T^{-1}\left(\boldsymbol{\rho}_{Rc} - \boldsymbol{\rho}_a^{mod}(\boldsymbol{x}_a)\right) \quad (35)$$

Where T is simply the diagonal matrix of transmittance, i.e. $T_{ii} = t(\lambda_i)$ for $1 \leq i \leq n$. Considering the forward AC, the aerosol term ρ_a^{mod} actually only depends on $\rho_w^{mod}(\boldsymbol{x}_w)$, through the atmospheric matrix Λ:

$$\begin{aligned} \boldsymbol{\rho}_a^{mod}(\boldsymbol{x}_a) &= \Lambda\, \boldsymbol{x}_a \\ &= \Lambda(\Lambda^T\Lambda)^{-1}\Lambda^T\left(\boldsymbol{\rho}_{Rc} - T\boldsymbol{\rho}_w^{mod}(\boldsymbol{x}_w)\right) \\ &= M_{atm} * \left(\boldsymbol{\rho}_{Rc} - T\boldsymbol{\rho}_w^{mod}(\boldsymbol{x}_w)\right) \end{aligned} \quad (36)$$

Where M_{atm} is a matrix of size $n * n$ combining Λ and its pseudo-inverse:

$$M_{atm} = \Lambda(\Lambda^T\Lambda)^{-1}\Lambda^T \quad (37)$$

Assuming that most of the uncertainties of the atmospheric correction are due to the aerosol reflectance $\boldsymbol{\rho}_a^{mod}$, hence the inversion of the marine IOP $\boldsymbol{x}_w$, and neglecting radiometric uncertainty on ρ_{Rc}, application of the GUM yields the variance-covariance matrix of ρ_w as a function of the variance covariance-matrix of $\boldsymbol{x}_w$:

$$C_{\rho_w} = \left(T^{-1}M_{atm}T\frac{\partial\boldsymbol{\rho}_w^{mod}}{\partial\boldsymbol{x}_w}\right)C_{x_w}\left(T^{-1}M_{atm}T\frac{\partial\boldsymbol{\rho}_w^{mod}}{\partial\boldsymbol{x}_w}\right)^T \quad (38)$$

This variance-covariance matrix of size $n * n$ gives the complete uncertainty of ρ_w, including the spectral correlation on the extra-diagonal terms:

$$C_{\rho_w} = \begin{pmatrix} var\big(\rho_w(\lambda_1)\big) & \cdots & cov\big(\rho_w(\lambda_1),\rho_w(\lambda_n)\big) \\ \vdots & \ddots & \vdots \\ cov\big(\rho_w(\lambda_1),\rho_w(\lambda_n)\big) & \cdots & var\big(\rho_w(\lambda_n)\big) \end{pmatrix} \quad (39)$$

Similarly, C_{x_w} is of size $n_w * n_w$ with $n_w = 5$ and represents the full uncertainty of the 5 IOPs.

In Eq. (38), the transmittance vanishes on the diagonal term, but are kept for the sake of completeness of the covariance, and also because the output bands of T^{-1} are not necessarily identical to the bands used in T for the aerosol detection. The Jacobian matrix $\frac{\partial\boldsymbol{\rho}_w^{mod}}{\partial\boldsymbol{x}_w}$ is of size $n * n_w$ and represents the sensitivity of the marine model to the IOPs; it is noted J hereafter:

$$J = \frac{\partial\boldsymbol{\rho}_w^{mod}}{\partial\boldsymbol{x}_w} \quad (40)$$

Computation of uncertainties of marine reflectance hence amounts to computation of J and C_{x_m}, both at convergence of the minimization process, as described below. The uncertainties given in the output product at all bands are the square root of the diagonal terms of C_{ρ_w}.

The Jacobian matrix can be approximated by first order Taylor expansion, thanks to the evaluation of $\boldsymbol{\rho}_w^{mod}$ on the $n_w + 1$ vertices of the final simplex. Let us note $\boldsymbol{x}^{(1)}$ the best vertex at convergence (i.e. retrieved $\boldsymbol{x}_w$), and $\boldsymbol{x}^{(2)} \cdots \boldsymbol{x}^{(n_w+1)}$ the n_w other vertices of the simplex. Then for a given wavelength λ_k, the vector column $J_k = \frac{\partial\boldsymbol{\rho}_w^{mod}(\lambda_k)}{\partial\boldsymbol{x}_w}$ is solution of the $n_w * n_w$ linear system:

$$\begin{pmatrix} x_1^{(2)} - x_1^{(1)} & \cdots & x_{n_w}^{(2)} - x_{n_w}^{(1)} \\ \vdots & \ddots & \vdots \\ x_1^{(n_w+1)} - x_1^{(1)} & \cdots & x_{n_w}^{(n_w+1)} - x_{n_w}^{(1)} \end{pmatrix} J_k = \begin{pmatrix} \rho_w^{mod}\big(\boldsymbol{x}^{(2)},\lambda_k\big) - \rho_w^{mod}\big(\boldsymbol{x}^{(1)},\lambda_k\big) \\ \vdots \\ \rho_w^{mod}\big(\boldsymbol{x}^{(n_w+1)},\lambda_k\big) - \rho_w^{mod}\big(\boldsymbol{x}^{(1)},\lambda_k\big) \end{pmatrix} \quad (41)$$

The matrix of the linear system, $(\Delta X)_{ij} = x_j^{(i)} - x_j^{(1)}$, does not depend on wavelength and can be inversed once only for a given pixel to retrieve all columns of the Jacobian matrix J. Furthermore, the efficient inversion of array of matrices in Python (module linalg.inv) allows to do it for all pixels of the image at once, as far as ΔX and the right-hand side of Eq. (41) are defined for all pixels in a single array. The computation of J is thus extremely fast over the full image, and matrix multiplication in Eq. (38) can be done similarly on all pixel simultaneously to compute rigorously and efficiently the per-pixel uncertainties of ρ_w.

Last, computation of the uncertainty of $\boldsymbol{x}_w$, i.e. matrix C_{x_w}, is the core of the uncertainty propagation.

NLLSQ are very advantageous for uncertainty propagation and have already been exploited in ocean colour data processing (Van der Woerd and Pasterkamp, 2008; Maritorena et al., 2010; Werdell et al. 2013).As done previously for $\boldsymbol{\rho}_a^{mod}$, the minimization problem Eq. (23) can be rewritten in a generic matrix notation (dimension refers to wavelength) as a function of $\boldsymbol{x}_w$ only:

$$\chi^2(\boldsymbol{x}_w) = \frac{1}{n - n_w}\left(\boldsymbol{\rho}_{Rc}^{mod}(\boldsymbol{x}_w) - \boldsymbol{\rho}_{Rc}\right)^T C^{-1}\left(\boldsymbol{\rho}_{Rc}^{mod}(\boldsymbol{x}_w) - \boldsymbol{\rho}_{Rc}\right) \tag{42}$$

With

$$\boldsymbol{\rho}_{Rc}^{mod}(\boldsymbol{x}_w) = M_{atm} * \left(\boldsymbol{\rho}_{Rc} - T\boldsymbol{\rho}_w^{mod}(\boldsymbol{x}_w)\right) + T\boldsymbol{\rho}_w^{mod}(\boldsymbol{x}_w) \tag{43}$$

The χ^2 is here written in a generic form with C accounting for spectral weights. When the input uncertainties are known, C is taken as the variance-covariance matrix of $\boldsymbol{\rho}_{Rc}$. Then the theory on NLLSQ gives access to the uncertainty of the retrieved parameters by:

$$\boldsymbol{C}_{\boldsymbol{x}_w} = \left(\left(\frac{\partial \boldsymbol{\rho}_{Rc}^{mod}}{\partial \boldsymbol{x}_w}\right)^{\boldsymbol{T}} \boldsymbol{C}^{-1}\left(\frac{\partial \boldsymbol{\rho}_{Rc}^{mod}}{\partial \boldsymbol{x}_w}\right)\right)^{-1} \tag{44}$$

where $\frac{\partial \boldsymbol{\rho}_{Rc}^{mod}}{\partial \boldsymbol{x}_w}$ is the Jacobian matrix of the model $\boldsymbol{\rho}_{Rc}^{mod}$ with respect to $\boldsymbol{x}_w$, computed when the minimum of χ^2 is reached. In the present situation, we have not identified any spectral shape in the uncertainty of the input radiometry (nor on the model), so that matrix C is formally set to identity. In this particular case, the uncertainty propagation on $\boldsymbol{x}_w$ must rely on the scalar estimate of the uncertainty on $\boldsymbol{\rho}_{Rc}$, assessed through the χ^2 metric at convergence (see e.g. Werdell et al., 2013 for a similar application in IOP inversion). In other word, the theory amounts to $C = \chi^2(\boldsymbol{x}_w) * I_d$. As a result, we have:

$$\boldsymbol{C}_{\boldsymbol{x}_w} = \chi^2(\boldsymbol{x}_w) * \left(\left(\frac{\partial \boldsymbol{\rho}_{Rc}^{mod}}{\partial \boldsymbol{x}_w}\right)^{\boldsymbol{T}} \frac{\partial \boldsymbol{\rho}_{Rc}^{mod}}{\partial \boldsymbol{x}_w}\right)^{-1} \tag{45}$$

The Jacobian matrix $\frac{\partial \boldsymbol{\rho}_{Rc}^{mod}}{\partial \boldsymbol{x}_w}$ is simply expressed with term already computed:

$$\frac{\partial \boldsymbol{\rho}_{Rc}^{mod}}{\partial \boldsymbol{x}_w} = (I_d - M_{atm})TJ \tag{46}$$

Once again, the matrix inversion in Eq. (45) is done globally for all pixels at once.

In summary, the uncertainty propagations defined by Eqs. (38)- (41)- (45)-(46) amounts to linear algebra, implemented in an efficient way in the code over the full scene at once. We emphasize that any improved knowledge on the input or model uncertainties could immediately be applied in this generic formalism. For instance, the uncertainties of ρ_w^{mod}, currently assumed as spectrally white, could be determined either statistically (validation of the in-water forward NN against in situ radiometric measurements) or theoretically (e.g. sensitivity of ρ_w^{mod} with respect to the fixed spectral slopes of the underlying IOP model) and used to define the variance-covariance matrix C both in the χ^2minimization, Eq. (42), and in the IOPs uncertainty, Eq. (44).

2.2 Bio-optical model for the Baltic Sea

Based on the in-situ data gathered over previous years in the Baltic Sea in Finland, Sweden and a special estuary campaign, the ranges and correlations of inherent optical properties are studied (Table 1 and Figure 2-9). The data suggests a weak correlation between TSM and chlorophyll concentration, which is modelled with a linear relationship and a wide range of scattering. For other IOPs only their ranges are considered.

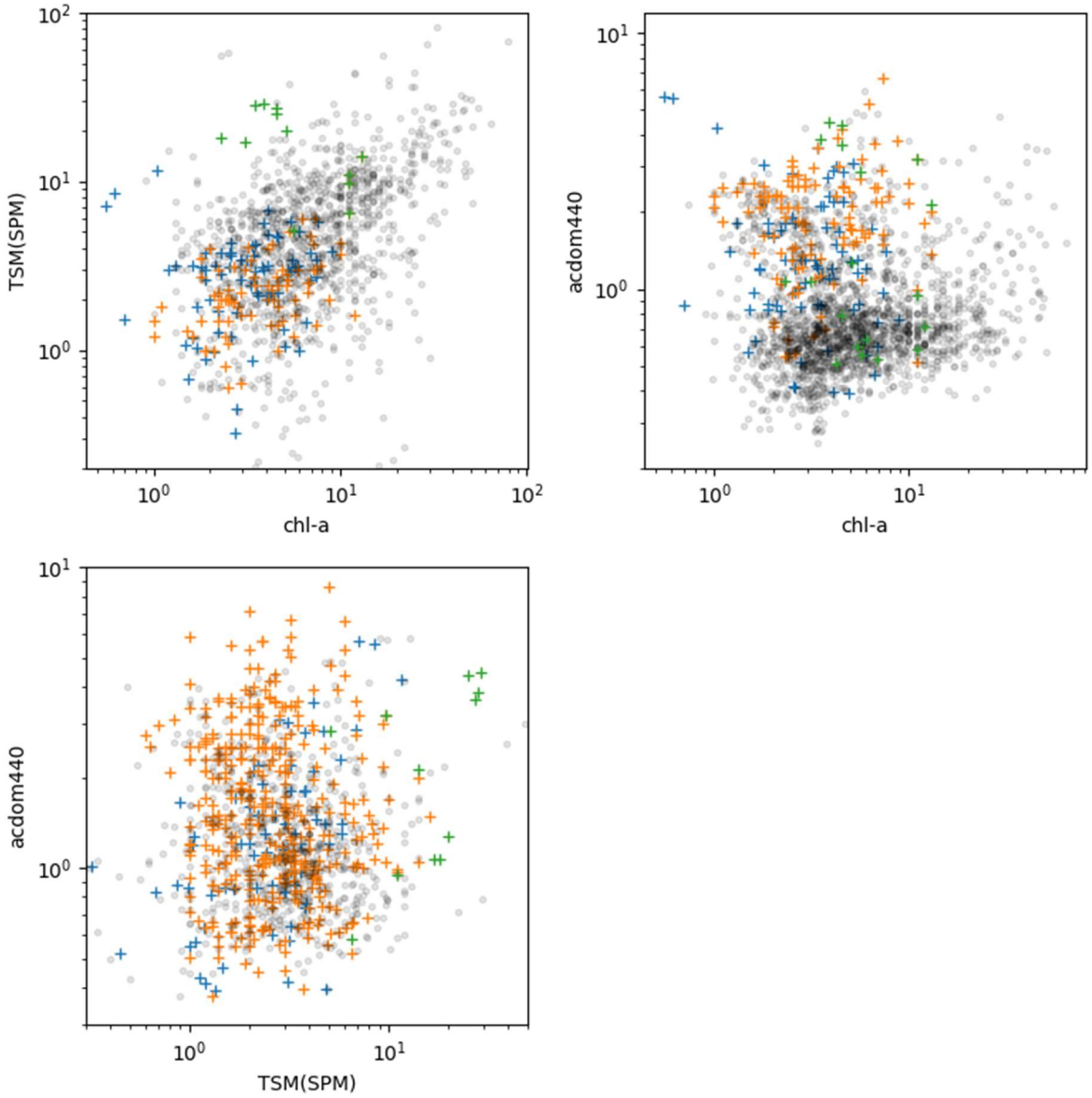

Figure 2-9. Relationships of IOPs or in-water constituent concentrations of in-situ measurements. Sources: from Finland (orange), from Sweden (blue), from estuary campaign (green). Other samples (transparent, grey circles) are estimated from secondary variables: TSM (mg/l) from turbidity, acdom440 (m^{-1}) converted from acdom400 (m^{-1}), acdom440 (m^{-1}) estimates from PtColor and Salinity. Chlorophyll concentration in µg/l.

Table 1: Overview of ranges of IOPs of Baltic Sea. Notes:
apig_max is 8.7 , if default C2RCC aph* is used (from SNAP conversion C1 = 21 C2 = 1.04)
***Max1: Extreme cases (educated guess) are higher than reliable observed maximum in water sampling data.**
***Max2: Exceptional extreme (educated guess) = this may be possible in some river mouths (a400: Bay of Bothnian rivers, TSM: South-Western Finland rivers)**

443 nm 1/m	Phase fct, Fournier Forand	SIOP	min	max1*	max2*				Reference
a_pig			0.0119	2.37		Chl_min	0.2	µg/l	aph* from Ylöstalo et al. 2014, package effect included
						Chl_max1*	200	µg/l	
						Chl_max2*	No	µg/l	
a_d		exp mean=0.0101 SD=? min= 0.0075 max=0.0128	0.016	8.1	24.3	a_dg_min	0.16	1/m	a_d slope from Ylöstalo et al. 2014
a_g		exp mean=0.0164 SD=? min= 0.013 max=0.0193	0.15	14.6	21.9	a_dg_max1*	22.7	1/m	a_g slope from Ylöstalo et al. 2014
						a_dg_max2*	46.2	1/m	
b_tsm	+	exp mean=0.80 SD=0.32 min=0.30 max=1.48	0.19	95	285	TSM_min	0.2	mg/l	Exp: Kallio (unpublished SALMON data)
						TSM_max1*	100	mg/l	
						TSM_max2*	300	mg/l	
b_p	+	exp=1.87							
b_w	+	exp=0.0							

The bio-optical model is the description how to compose realistic combinations of IOPs for the Baltic Sea. These combinations fulfill the following relationships:

- IOP values are within the tabled ranges of a_{pig}, a_d, a_g, a_{dg}, b_{tsm}
- Backscattering of TSM is modelled as a coloured part and a white scatterer. $b_{tsm} = b_p + b_w$
- Absorption of detritus a_d is coupled with the particle backscattering b_p. The model combines relationships defined by Ylöstalo and Doerffer.
- a_g depends on a_d, within range of $a_{dg} = a_d + a_g$
- a_{phi} is selected depending linearly on TSM / b_p

The combinations of IOPs are used to simulate water leaving reflectance spectra rho_w =f(a_{pig}, a_d, a_g, b_p, b_w, angles, wind, T, S), which conform the training dataset for neural networks. They are designed to emulate the modelling of spectra themselves (forward neural network), calculating a water leaving reflectance spectrum from a set of IOPs.

Or they are trained to solve the inverse problem (backward neural network), estimating IOP values from a given reflectance spectrum. In either case, values of input and output of the neural network should be more or less uniformly distributed to allow for a successful learning process. Uniformity in IOPs can be achieved more easily and closer to real world measurements by logarithmic transformation. Therefore, during the selection process of IOP combinations, they are often transformed first.

2.2.1 Parameterization of particulate scattering

b_{tsm} and its variability in concentration and spectral slope is modelled by two components, the coloured part b_{p0} with a fixed spectral slope S=1.87 and a white scatterer b_w with spectral slope zero (at λ_0=440 nm). The advantage of this formulation with a white component (b_w) and a spectral component (slope S) is to model any other spectral slope (S_{tot}) with a linear combination. Hence, b_{p0} and b_w should not be individually related to physical quantities, only the sum makes sense. Strictly speaking, the sum of two power functions is not exactly a new power function. To have an idea, if the sum tries to fit a new power function at two extreme bands λ_0 and λ_1, a good approximation is:

$$b_{tsm}(\lambda) = b_{p0}\left(\frac{\lambda}{\lambda_0}\right)^{S} + b_w \approx b_{tsm}(\lambda_0)\left(\frac{\lambda}{\lambda_0}\right)^{S_{tot}} \tag{47}$$

with

$$\begin{cases} b_{tsm}(\lambda_0) = b_w * (1+r) \\ S_{tot} = \dfrac{log\left(\dfrac{1 + r * \left(\frac{\lambda_1}{\lambda_0}\right)^{S}}{1+r}\right)}{log\left(\frac{\lambda_1}{\lambda_0}\right)} \end{cases} \tag{48}$$

and r is the ratio between the two scattering components:

$$r = \frac{b_{p0}}{b_w} \tag{49}$$

This approximation is not the best fit over all wavelengths in term of least-squares but allow to quickly understand the issue of the mixing. The important aspect is that the slope of the mixing depends on the ratio $r = \frac{b_{p0}}{b_w}$. When $b_{p0} = 0$, $r = 0$ and we retrieve logically a white component with $S_{tot} = 0$. Theoretically, all slopes between 0 and S are reachable. Hence S should represent, physically, the maximum slope observed in the Baltic.

From in-situ measurements the distribution of S_{tot} is known to be centered around 0.8 with a standard deviation of 0.32, and the range of b_{tsm}.

Modelling takes the following steps:

1. Select $\boldsymbol{S_{tot}}$ from a **normal** distribution randomly and restrict the selected slope to the interval of minimum and maximum values (see Figure 2-10).
2. Select $\boldsymbol{\log_{10} b_{tsm}}$ from a **uniform** distribution from the interval of minimum, maximum=2.5 ($b_{tsm,max} =$ 316 mg/l).
3. Calculate the ratio **r** of b_{p0} and b_w from:

$$r = \frac{1 - \left(\frac{\lambda}{440}\right)^{S_{tot}}}{\left(\frac{\lambda}{440}\right)^{S_{tot}} - \left(\frac{\lambda}{440}\right)^{S}} \tag{50}$$

4. Calculate $b_w = \frac{b_{tot}(\lambda_0)}{1+r}$
5. Calculate $b_p = r * b_w$

This parameterization leads to the desired spectral slope S_{tot} in the addition of the two components with fixed slopes.

Backscattering ratio is chosen from a uniform distribution between values of 0.013 and 0.02, so that the Fournier-Forand phase function can be applied during simulations.

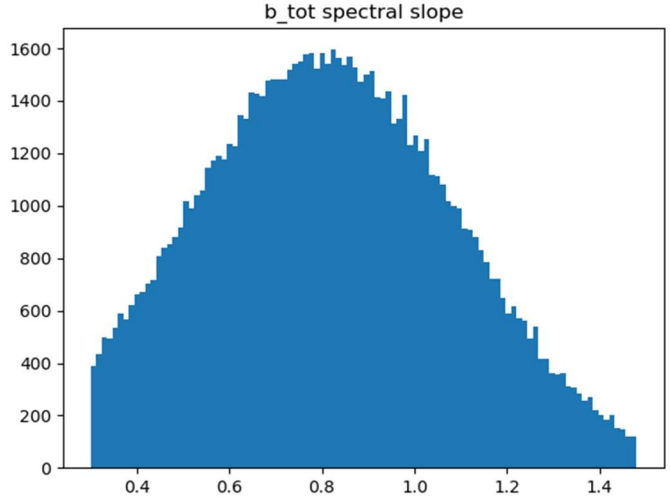

Figure 2-10. Distribution of spectral slopes of backscattering selected in the bio-optical model.

2.2.2 Parameterisation of detritus absorption

The absorption of detritus a_d (also labeled absorption of non-algae particles, a_{nap}) should naturally depend on the total suspended matter concentration, which is already defined in the first step of the bio-optical by b_{tsm} or its components b_p and b_w. A model of Doerffer (derived from investigations of the NOMAD in-situ dataset) provides a relationship between b_p and a_{nap}, which does not return values in the needed upper range. Therefore, the model of Ylöstalo has been combined with it, using a uniform random process to model the variability:

$$\log_{10} a_{nap}\,(442nm) = \log_{10}\left(0.079 * 10^{\log_{10} b_p * 1.1 + 0.12)}\right) - 2 * 0.245887 + random * 4 * 0.2458872 \quad (51)$$

If the variability in the slopes of a_d is to be modelled, the parameter will be split up into two components with no actual physical meaning and two fixed slopes (one of them 0). This approach is following the same rationale as in the modelling of b_{tsm}. From in-situ measurements the range of a_d is given.

Modelling takes the following steps:

1. Calculate $\log_{10} \boldsymbol{a_d}$ as a function of b_p.
2. If the variability of slopes of a_d is modelled, follow a similar scheme as for b_{tsm}:

   a) Select slope $\boldsymbol{k}$ from a **normal** distribution (mean 0.0101, standard deviation 0.002) randomly and restrict them to the interval of minimum, maximum values.

   b) Calculate the ratio **r** of a_{d1} (slope $k_1 = 0.014$) and a_{d0} (slope $k_0 = 0$) from:

$$r = \frac{1 - \exp(-k(\lambda - \lambda_0))}{\exp(-k(\lambda - \lambda_0)) - \exp(-k_1(\lambda - \lambda_0))}$$

   c) Calculate $a_{d0} = \frac{a_d(\lambda_0)}{1+r}$

   d) Calculate $a_{d1} = r * a_{g0}$

During the calculations of simulated water leaving reflectance spectra with Hydrolight both components are used so that the model includes a variability of slopes. Nevertheless, during training of the neural networks only the physically meaningful IOP a_d is used.

2.2.3 Parameterisation of gelbstoff absorption

Gelbstoff absorption is a part of the absorption $a_{dg} = a_d + a_g$, which is often measured as such. Therefore, a_g depends on the already chosen a_d, and the range of a_g is restricted by the range of $a_{dg}$and the already selected a_d.

If the variability in the slopes of a_g is to be modelled, the parameter will be split up into two components with no physical meaning and two fixed slopes (one of them 0).

Modelling takes the following steps:

1. Select log $\boldsymbol{a_g}$ from a **uniform** distribution randomly within the interval of minimum = min(a_g), maximum = max(a_{dg}) - a_d.
2. If the variability of slopes of a_g is modelled, follow the same scheme as for b_{tsm}:
   a) Calculate slope $\boldsymbol{k}$ [nm^{-1}] from Ylöstalo relationship with a_g and select those below 0.016 :
   $$k = \left(10.83 + \frac{45.92}{6.06 + a_g}\right) * \frac{1}{1000}$$
   b) If k>0.016, select randomly from normal distribution (mean=0.0185, sd=0.001).
   c) Calculate the ratio **r** of a_{g1} (slope $k_1 = 0.021$) and a_{g0} (slope $k_0 = 0$) from:
   $$r = \frac{1 - \exp(-k(\lambda - \lambda_0))}{\exp(-k(\lambda - \lambda_0)) - \exp(-k_1(\lambda - \lambda_0))}$$
   d) Calculate $a_{g0} = \frac{a_g(\lambda_0)}{1+r}$
   e) Calculate $a_{g1} = r * a_{g0}$

The two components of a_g are only used in the simulation processing, which allows for an easy modelling of the variability in spectral slope k. The neural network training uses the gelbstoff absorption directly.

2.2.4 Parameterisation of chlorophyll absorption

Investigating the Baltic Sea in-situ data leads to modelling a week linear relationship between a_{phi} and TSM (see Figure 2-9 top right). A conversion of TSM and b_p (Doerffer) is used at first:

$$\log_{10} TSM = \log_{10} b_p * 1.1 + 0.12 \quad (52)$$

A linear function, which expresses the correlation in the data and the scattering, is given by:

$$\log_{10} Chl = (\log_{10} TSM + 0.3738 - random * 4 * 0.19724) * 1/1.2307 \quad (53)$$

Conversion of chlorophyll concentration to pigment absorption is handled by the following expression (Ylöstalo):

$$\log_{10} a_{pig}(440nm) = \log_{10} 0.043 + (1 - 0.237) * \log_{10} Chl \quad (54)$$

The simulations use the specific pigment absorption as reported by Ylöstalo from measurements in the Baltic Sea.

2.2.5 Finalising the IOP selection

The bio-optical model uses several random processes during deriving a large set of combinations of IOPs. After that random sampling with the described dependencies, the IOPs are not uniformly distributed, as it would be beneficial for the neural network training. The combinations are filtered in several steps, so that the final selection of 80000 samples is close to uniformity within the given range for each IOP (Figure 2-11). Only the total backscattering coefficient is extended beyond the tabulated limits and some samples with higher btot are allowed.

The variability of spectral slopes in detritus and gelbstoff absorption and total backscattering is introduced (Figure 2-12). The cross-correlations of IOPs are evenly distributed within their ranges and their expected dependencies (Figure 2-13).

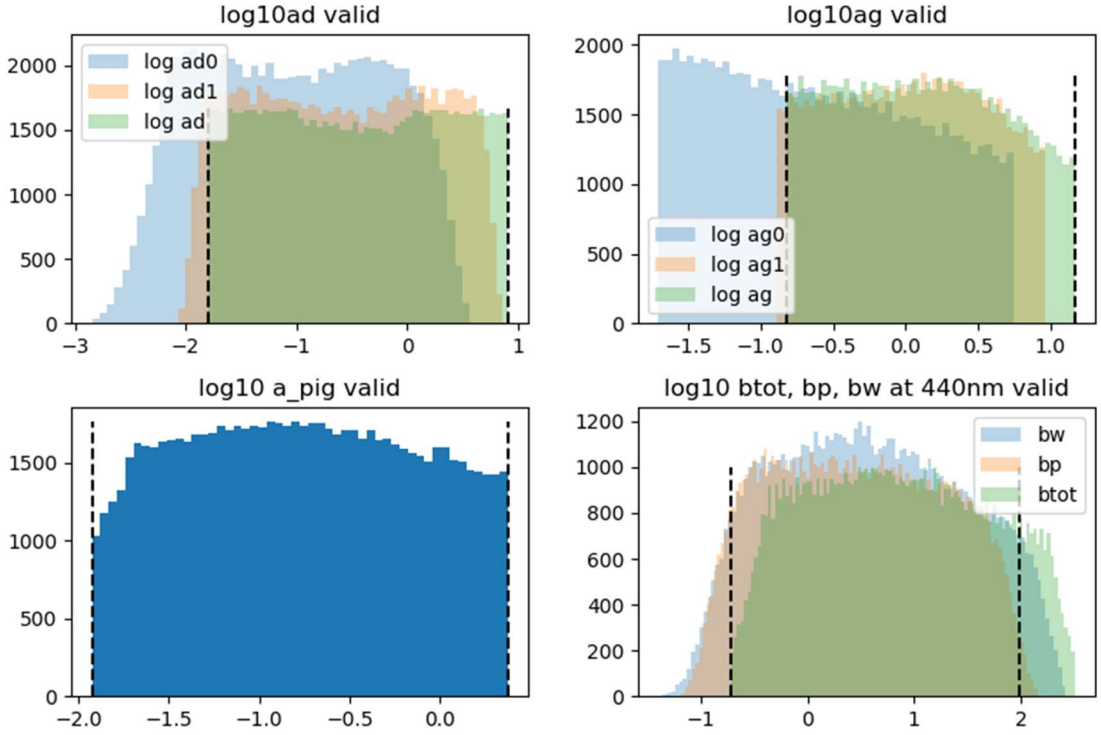

Figure 2-11. Distribution of log-transformed IOPs after filtering to achieve uniformity. This selection has been used as input to the simulation of water leaving reflectances. Desired ranges are indicated by vertical dashed lines.

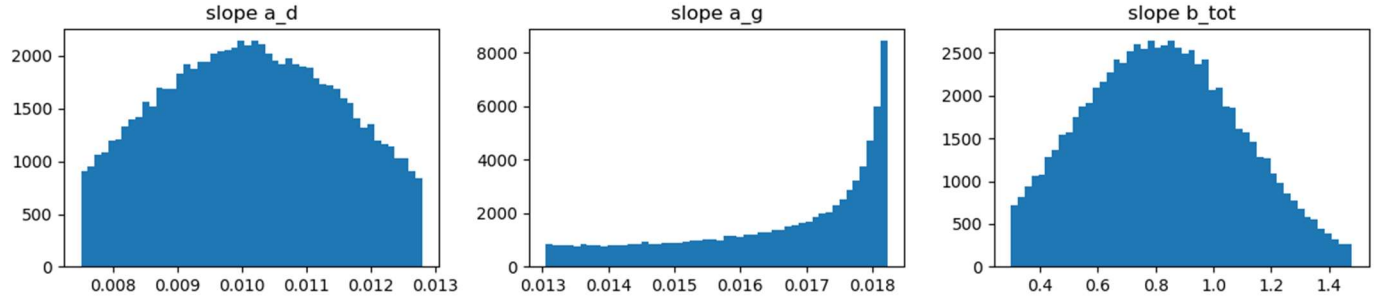

Figure 2-12. Distribution of spectral slopes of detritus absorption, gelbstoff absorption and total backscattering coefficient.

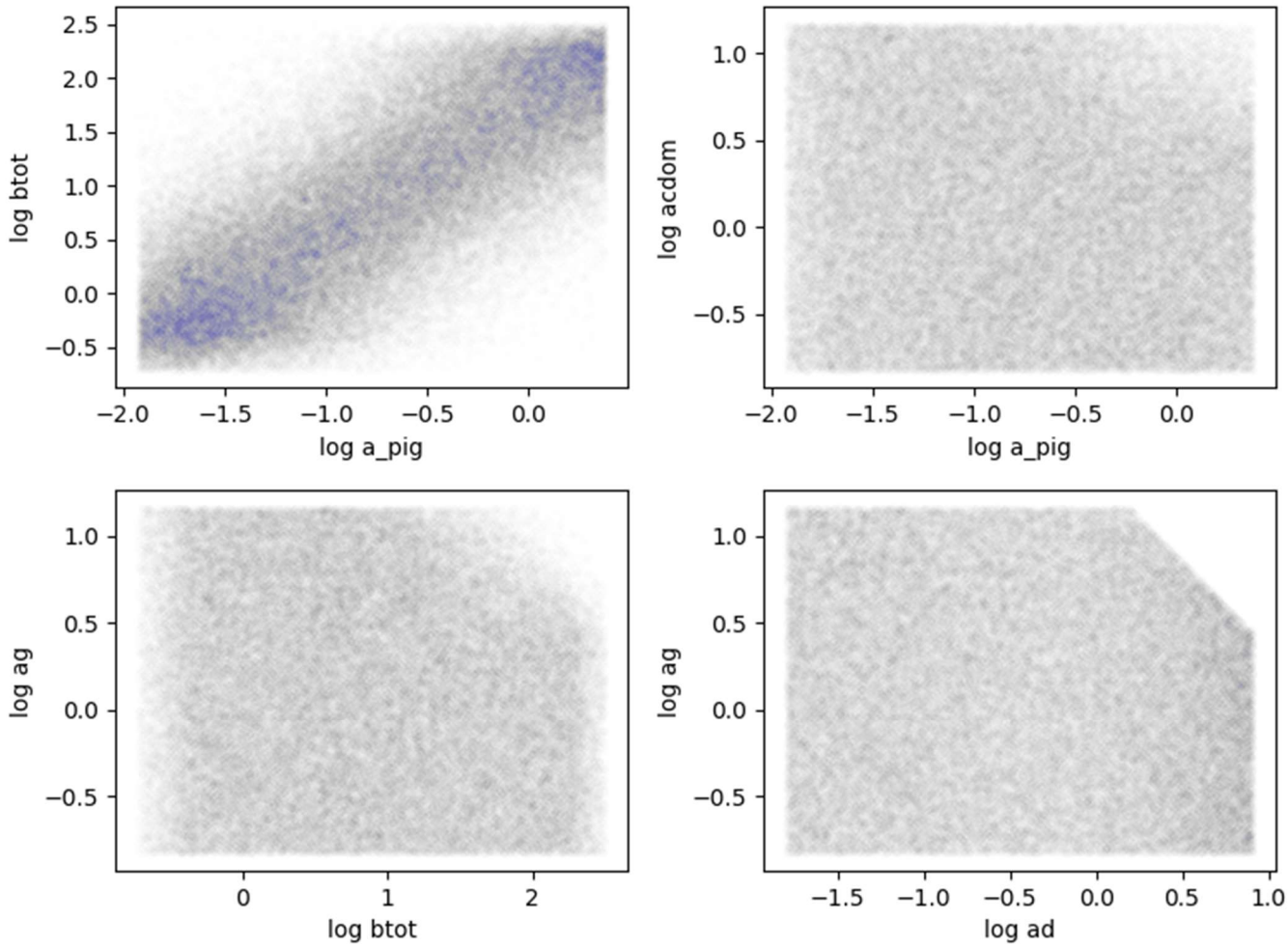

Figure 2-13. Cross-correlations of log-transformed IOPs. According to expectation apig and btot show a weak linear dependency. Other IOPs are evenly distributed within their limits and dependencies.

2.2.6 Simulations of water leaving reflectances

The water leaving reflectances are simulated with HydroLight using the IOP combinations of the bio-optical model. For each case out of 80000, the variables sun zenith, wind speed, salinity and temperature are randomly chosen (ranges: sun zenith 0-75°, windspeed 0-9 m/s, salinity 0-20 PSU and temperature 0-22° C) and held fixed. For each case 7 observation angles (view zenith 0-60°, view azimuth 0-180° in 10° steps) are selected randomly, leading to a total number of 560000 simulated spectra. The spectra are calculated at 31 wavelengths (in nm: 395, 400, 405, 412, 443, 465, 489, 500, 510, 520, 531, 551, 555, 560, 620, 632, 659, 665, 670, 674, 678, 681, 709, 748, 754, 765, 779, 865, 869, 885, 1020) to account for the central wavelengths of the bands of several ocean colour satellites (i.e. MERIS, MODIS, SeaWifS, Sentinel 3 OLCI-A and OLCI-B).

The training dataset is reduced to the wavelengths, which are central wavelengths of the Sentinel-3 OLCI bands and outside absorption of the atmosphere (water vapour, oxygen). The reflectance at band 1 at 400nm is calculated from the simulations at 395, 400, 405nm weighted with the spectral response function of OLCI-A. There remain 16 bands (for wavelengths, see Figure 2-14). Currently, no dedicated training dataset for S2 has been implemented: OLCI bands are used and, when necessary, interpolated to MSI bands. This leaves two bands (OLCI 709 -> MSI 704 and 779->783) with a 4nm difference between central wavelengths. At 740 nm a linear interpolation between 709 and 754 has been used as an approximation. Still, these spectra have more likely the correct spectral shape and the low values in the strongly absorbing water.

The bio-optical model leads to spectra, which have often a similar shape with the maximum of the spectrum at 560nm (Figure 2-14). Spectra with blue water are not part of the simulations. This behaviour is in accordance with published spectra of the Baltic Sea (Ficek et al 2011, Kowalczuk et al 2005).

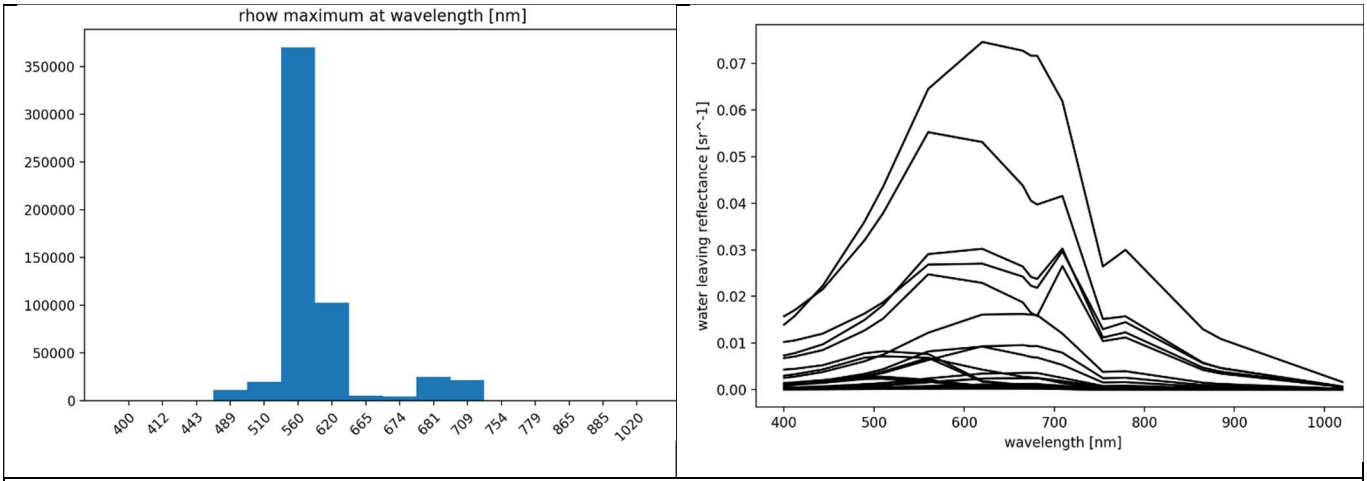

Figure 2-14. Distribution of the maxima of the water leaving reflectance spectra with respect to the OLCI bands' central wavelength (left). Most of the spectra have their maximum at 560nm, no spectra have been modelled with maxima in the blue. Example spectra (right).

The simulation dataset is split into two parts: the training dataset, which is used in the machine learning process, and the validation dataset, which is dedicated to testing and evaluating the trained model on an independent dataset.

2.2.7 Forward Neural Network

The forward neural network (fwNN) is trained to emulate the simulation process in a simplified manner. During the investigations accompanying the training process, it has been found that the learning process is much better, if the number of auxiliary variables is reduced to a minimum. Instead of the full set, which is needed for the Hydrolight simulations, only the three angles (sun zenith, view zenith and azimuth difference) are included in the input to the NN. The influence of wind, temperature and salinity is learned as natural variability in the spectra.

To avoid accumulation of specific rho_w values per band, which can lead to a tendency to reproduce this value in the output of the fwNN, the training data has been filtered, so that each band has more uniformly distributed values. Both input and output values are transformed: the reflectances and IOPs are log transformed, the angles are transformed by the cosine function.

In the semi-automatic training approach, several neural networks are trained for a fixed number of epochs, to find the most promising one at that stage of learning with the help of the validation data. The networks differ in architecture and activation function (sigmoid or relu), the batch size can vary as well. The loss function is defined as the mean square error of the transformed reflectances.

The selection criteria for the best neural network are evaluating the overall accuracy in terms of absolute median of the difference between estimated and reference rhow per band, sum over all bands, and the precision in terms of standard deviation per band.

The neural network with the architecture of 8 input neurons, three full connected hidden layers with 50x40x40 neurons and 16 output neurons, a batch size of 20000 samples, and sigmoid activation function returned the best statistics after 20000 epochs. It has been trained further until 60000 epochs. The median of the error is close to zero for all bands (Figure 2-15), the number of outliers varies and is particularly large for bands at 674 and 681nm, where the chlorophyll absorption can lead to a strong peak in the spectrum (see also example spectra, Figure 2-16).

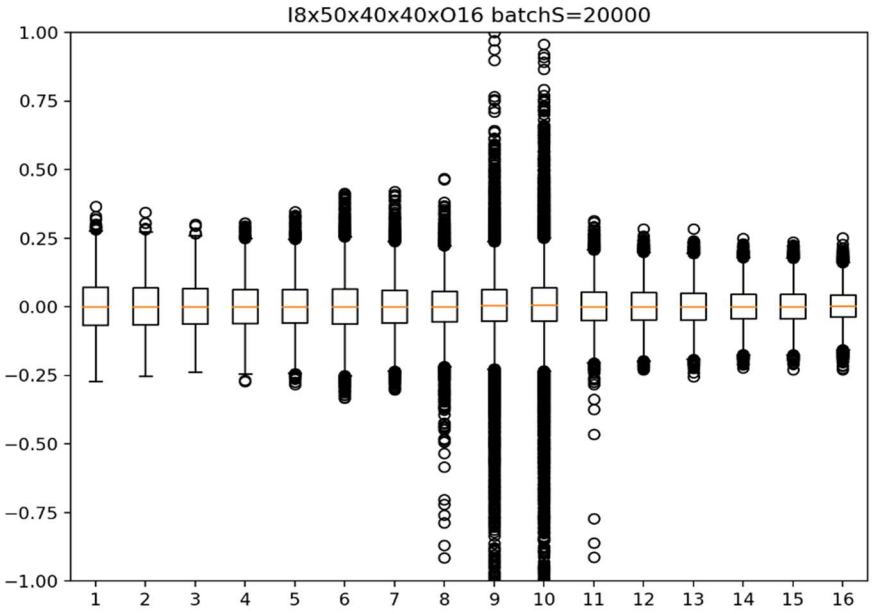

Figure 2-15. Difference of predicted to actual log rhow for 16 bands included in the training. The boxplot shows the median in orange, whiskers at Q1 – 1.5*(Q3-Q1) and Q3 + 1.5*(Q3-Q1), other points outliers, see matplotlib default. Q1 is the first quartile 25%, Q3 is the third quartile 75%. Best fwNN after 60000 epochs.

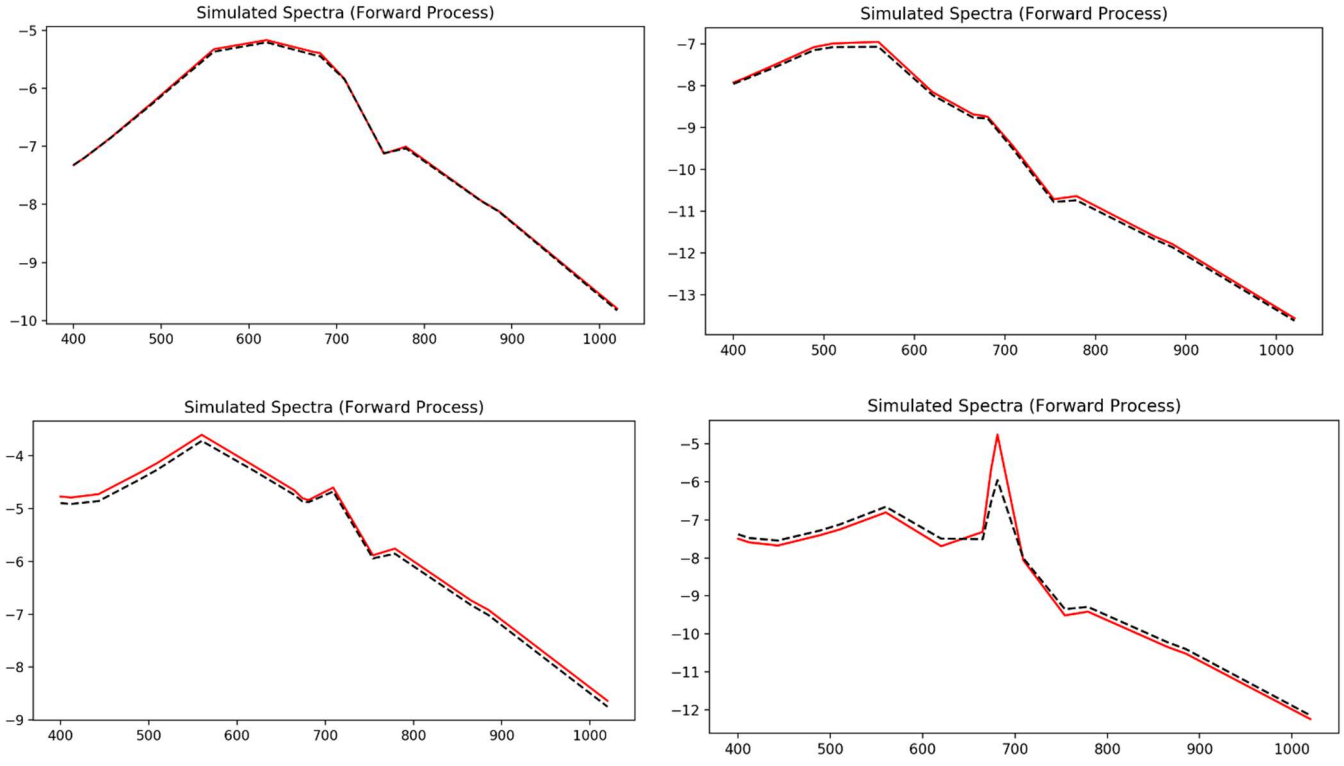

Figure 2-16. Examples of water leaving reflectance spectra (log-transformed, natural). The predicted spectrum (dashed) is capturing the shape of the reference spectrum (red) quite well, at extreme features (bottom right) the absolute values can be off.

2.2.8 Backward NN with minimization on rhow

The best fwNN becomes the basis of the backward NN training, when the goal is to achieve reciprocity between backward and forward NN.

The Hydrolight simulations with Baltic+ bio-optical model are subjected to the best fwNN and the output of water leaving spectra is used for the training. This way, the noise in the input of spectra to the backward NN can be reduced, as only the spectra known to the fwNN are used in the training. This might be disadvantageous, if the backward NN is supposed to work with any water leaving reflectance spectra; but it leads to better reciprocity.

The training approach is the same as before, the transformations for the variables remain the same as for the fwNN. The loss function is built on the water leaving reflectances, which are calculated with the forward NN out of the IOPs estimated by the backward NN: $rho_w^* = fwNN[bwNN[rho_w]]$

After 20000 training epochs the selection of the most promising architecture and batch size takes place, evaluating the water leaving reflectances. The best candidate is trained for a longer cycle and the best model is selected in the end. The best backward NN (with reciprocity) is found with an architecture of 19 input neurons (16 rhow, 3 angles), 3 hidden layers (77x77x77) and 5 output neurons representing the IOPs of the Baltic Sea bio-optical model. The batch size is set to 10000, activation function is sigmoid, the training finished after 200000 epochs.

Although the training is not focused on the minimisation of the error in IOPs, they are derived quite well (Figure 2-17). If the reciprocity is tested focusing on the reflectance spectra, it is very well met (Figure 2-18). By starting from the tabulated IOPs in the validation dataset, the baseline of reflectance spectra is calculated by subjecting them to the fwNN. Then, from these spectra IOPs are derived with the bwNN (trained on rho_w minimization) and these IOPs are again input to the fwNN, leading to the spectra, which are compared to the first fwNN output. This is the ideal case and it mirrors the minimization process during training.

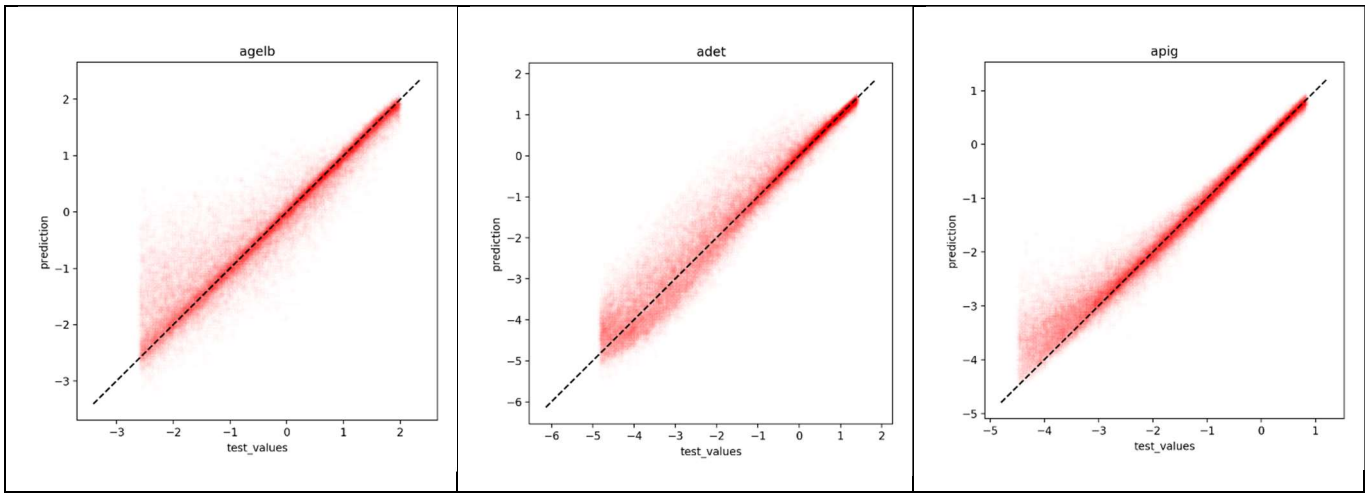

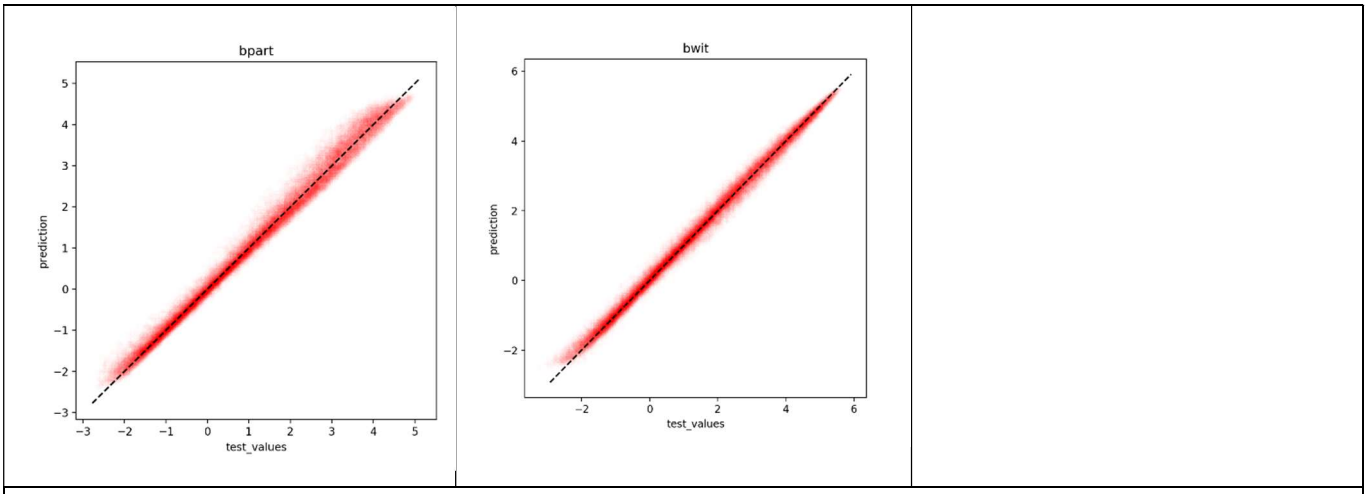

Figure 2-17. Comparison of IOPs (log-transformed). IOPs in the training dataset (x-axes) versus IOP predictions from bwNN[fwNN[IOP]].

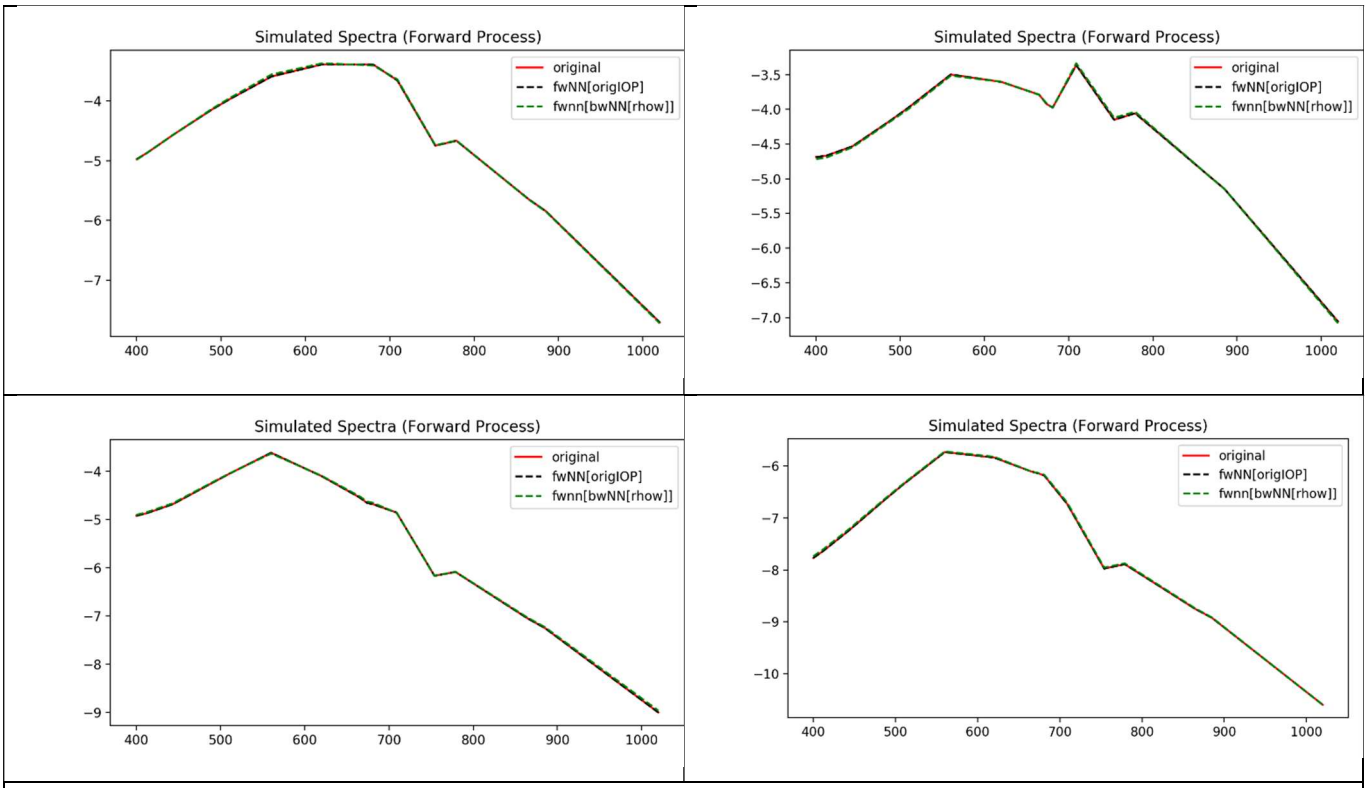

Figure 2-18. Example of reciprocity in the water leaving reflectance spectra. Original spectra and fwNN[original IOPs] (red, black dashed) are the same. Based on this spectrum from the fwNN, the bwNN is used to derive IOPs, which are again given to the fwNN (green dashed line). Reciprocity is nicely met.

2.3 In-water processing

The options for in-water processing include the in-water part of the C2RCC processor (Brockmann et al., 2016), the in-water part Case 2 Extreme (C2X, http://www.brockmann-consult.de/c2x/index.php/home/), band ratios calibrated with in situ data (e.g. Kallio et al., 2014) and the new in-water NN trained specifically for the Baltic Sea based on a bio-optical model optimized for the Baltic Sea during the SeaLaBio project.

2.3.1 Backward NN with minimization on IOPs

While the C2RCC processor contains among others a neural network, which derives IOPs, the underlying bio-optical model is based on observations in the North Sea and the globally distributed NOMAD dataset. The specifics of the Baltic Sea are not necessarily covered. The bio-optical model described above (see chapter 2.2) is dedicated to the conditions of the Baltic Sea including those near coast and estuaries.

The backward NN with minimization on rhow (see section 2.2.8) is not the most suitable to replace the neural network of C2RCC for deriving the optically active water constituents. So instead, another backward NN has been trained by minimizing the error on IOPs. After selecting a NN architecture and training it for a larger number of epochs, the best backward NN has been identified by its minimum of the sum of absolute differences of all IOPs (log-transformed).

The best NN based on the Hydrolight simulations has been trained with the 'softplus' activation function, a batch size of 20000 samples, 19 input neurons (cosine of three angles, log of rhow), three hidden layers with 77x77x77 densely connected neurons, and 5 output neurons (log IOPs). At epoch 162806 the best reproduction of the IOPs has been found (Figure 2-19). The prediction of pigment absorption and both the backscattering components works quite well, there is only a slight underestimation of a_pig between values of -2 to -3.5 log m^{-1} and an overestimation for values below -3.5 log m^{-1}. The gelbstoff absorption shows a higher density of validation samples close to the 1:1 line over the entire training range, but also some scattering. In the lower value range (below -2 log m^{-1}) the prediction can lead to an overestimation. Detritus absorption is still focused on the 1:1 line for upper half of the training range (above -0.5 log m^{-1}) but gets scattered rather broadly for lower values. In the very low range, the prediction overestimates the actual value.

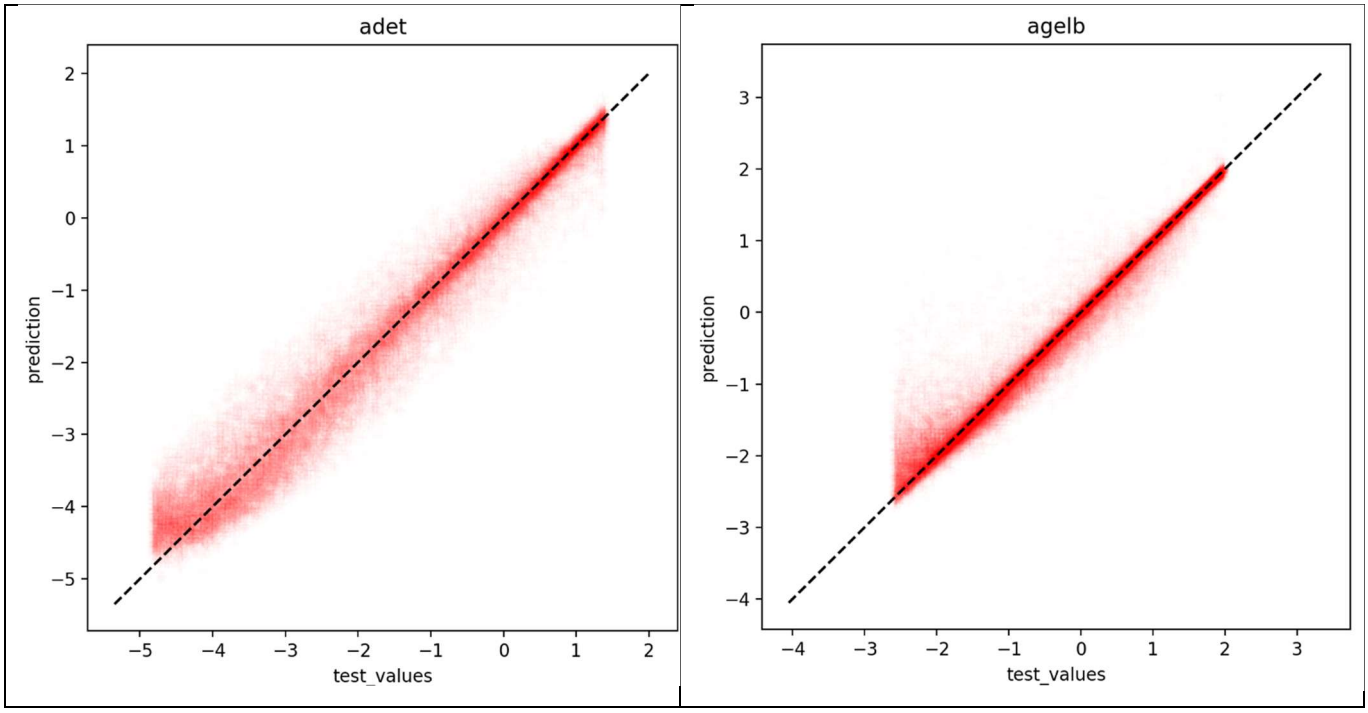

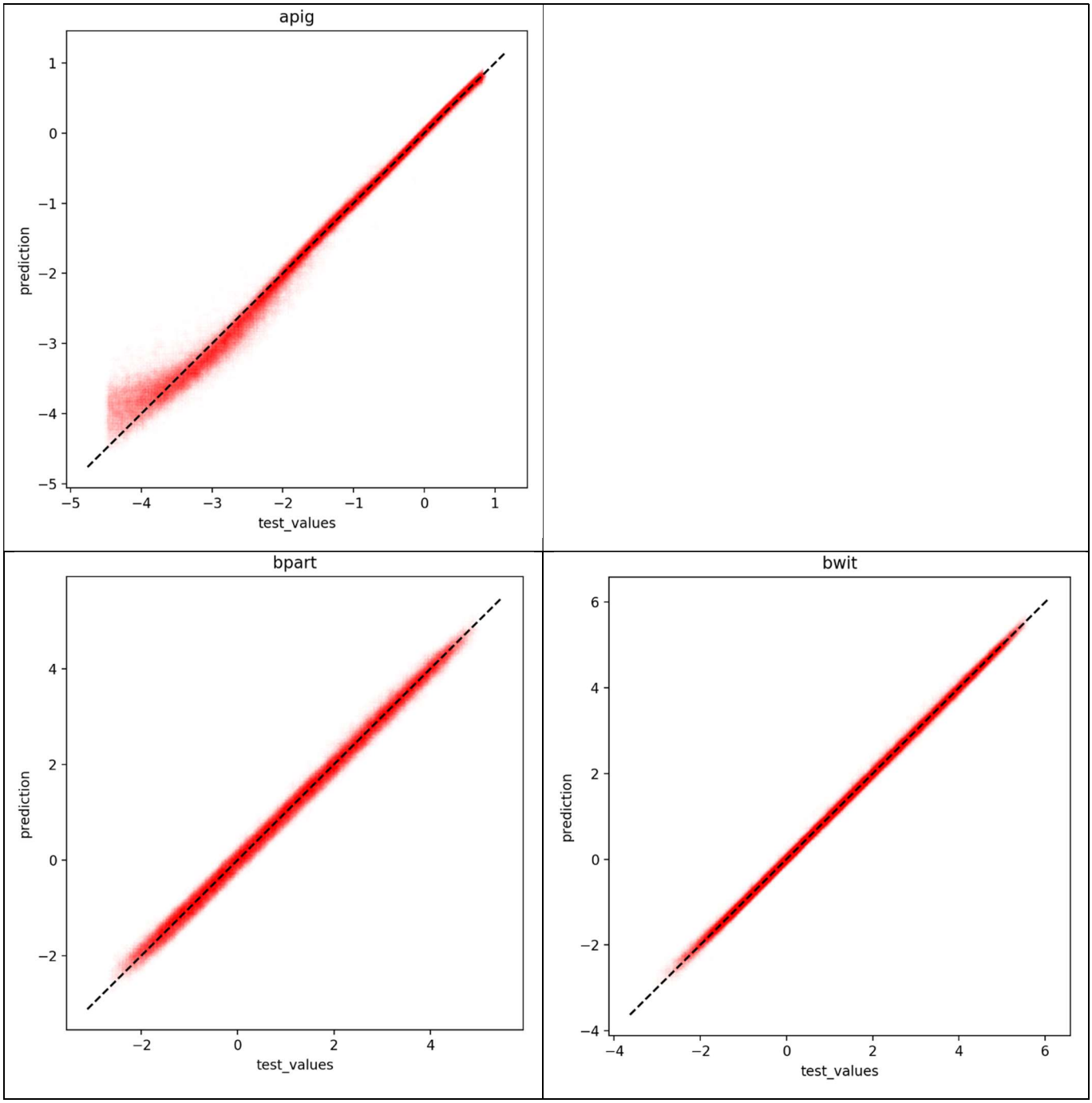

Figure 2-19. Validation of IOPs after training the backward NN, with reference values on x-axis and the bwNN predictions on y-axes. All retrieved IOPs show good agreement with the reference, with some minor issues in the lower ranges of the absorption components. (Further details can be found in the text.)

2.4 S2 and S3 data merging

2.4.1 Synergy approach

A synergistic use of the spectral measurements of S2 and S3 is difficult due to the differences in overpass time in combination with water as a rapidly changing object, and due to differences in spatial scales and viewing geometry. Instead, our approach consists in exploring synergy on product level, i.e. IOPs, Chl-a, TSM, CDOM, etc., which

are inherent water properties (i.e. they do not depend on how we optically observe them). Our methodology relies on two key ingredients:

- Product calibration. Any systematic error is removed by comparison of the EO products with our validation dataset. This is done separately for the whole time series of each sensor.
- Product uncertainties. Each marine product can be seen as an imperfect measurement of a real quantity (the measurand, corresponding to the truth), associated to an uncertainty. Consequently, we can combine different measurements of the same quantity and calculate averages, time series, etc., as far as we properly handle the output uncertainties of each product for each sensor. On a practical level, we will define areas near river mouths, extract CDOM-pixel values derived from satellite data (S2 and S3) from these areas, form a mean/median time series of all available measurements, and the use those as input data in the ERGOM model. Since S2 can cover areas closer to the river mount than S3, the extraction areas may be different. The results of using S2 data as ERGOM input are shown in the Impact Assessment Report of this project.

2.4.2 Algorithm calibration

It has been demonstrated that MSI can retrieve very well the variation and intensity of turbidity and CDOM absorption, after calibration with in situ data (Figure 2-20). Comparison of Chlorophyll-a computed by MSI and OLCI is also very good, within the range of uncertainty brought by in situ measurements Figure 2-21). The extensive validation dataset detailed in our proposal will thus first serve at checking the consistency between S2 and S3 products and applying inter-calibration if required. In this respect, we can make a strong analogy with the synergy product of Vanhellemont et al. (2014) between MODIS and SEVIRI sensor: SEVIRI has a very limited radiometric sensitivity and low spatial resolution, but high temporal frequency (every 15 minutes); MODIS has suitable radiometric and spatial specifications for OC, but limited revisit time. The synergy consists in taking the relative temporal variation of SEVIRI and applying to it an absolute scaling by the MODIS retrieval. In our case, assuming that OLCI will give the best Level-2 product (in absolute unit), a scaling of S2 retrieval can be applied to get a relevant product at high spatial resolution.

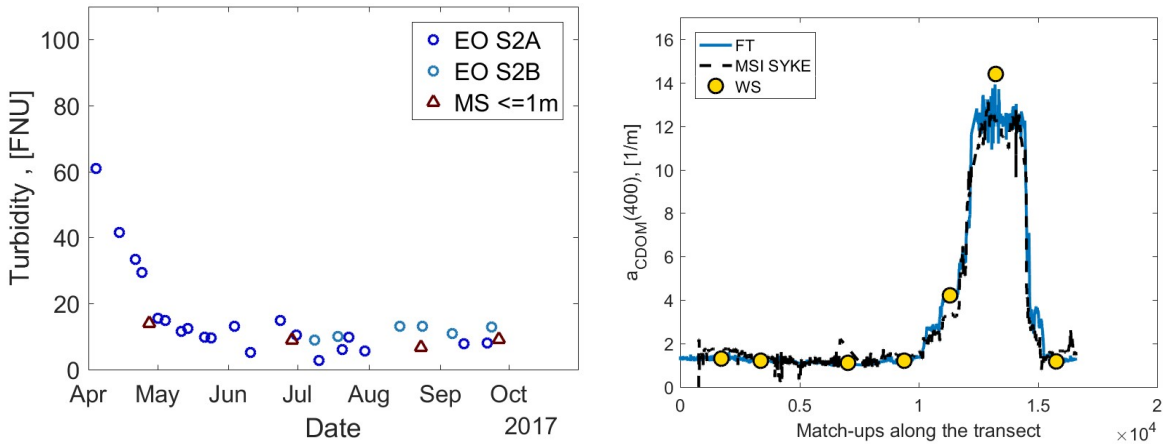

Figure 2-20. Left: Example of the correspondence between turbidity analysed via water samples and estimated via S2A and S2B (C2RCC-based) at a monitoring station (MS) location nearby a river estuary in Finland. Right: Correspondence of the absorption of CDOM as analysed via S2 (MSI SYKE, C2RCC-based algorithm) and field measured flow-through transect (FT) and water samples (WS) on a coastal estuary. In both cases in situ measurements have been used to calibrate the EO results. The origin of the spikes visible in the MSI SYKE data is not known.

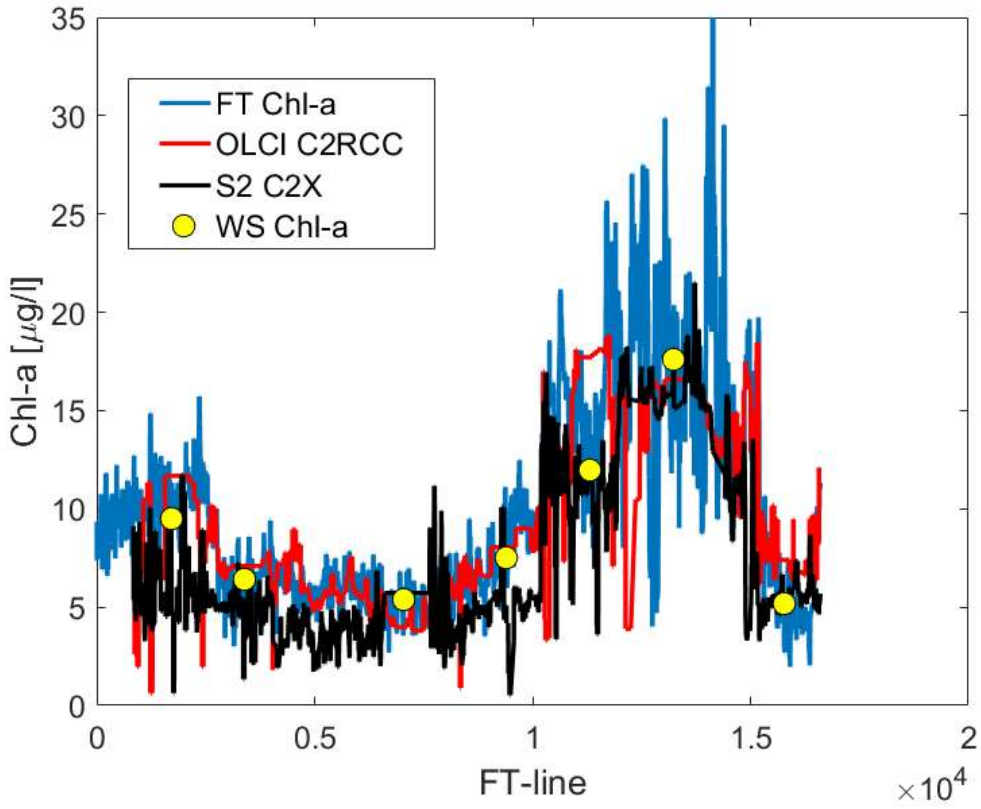

Figure 2-21. Initial experiments of using s3 OLCI and S2 MSI for determining Chl-a concentrations along a flow-through (FT) transect in an estuary (Helsinki, Finland). The data are processed using C2RCC-based approach (C2RCC and C2X-processors).

2.4.3 Level-3 generation

A Level-3 product is composed of several Level-2 products which are merged by weighting their per-pixel uncertainties. A monthly median/mean product is an example of this. The use of temporal aggregation reduces noise and the effects of cloud cover and facilitates the comparison with products from other sources.

2.5 BGC model

In general terms, the BGC model (Figure 2-22) simulates the marine nitrogen and phosphorus cycle. Three functional phytoplankton groups are involved in primary production (large cells, small cells, and cyanobacteria). A dynamically developing bulk zooplankton variable provides grazing pressure on the phytoplankton. Dead particles accumulate in the detritus state variable. In the sedimentation process, a portion of the detritus is mineralized into dissolved ammonium and phosphate. Another portion reaches the sea bottom, where it accumulates as sedimentary detritus and is subsequently buried, mineralized or resuspended into the water column, depending on the velocity of near-bottom currents. Under oxic conditions, some of the mineralized phosphate is bound by iron oxides and is thus retained in the sediment, becoming liberated when conditions become anoxic. Oxygen development in the model is coupled to biogeochemical processes via stoichiometric ratios, with oxygen levels in turn controlling processes such as denitrification and nitrification.

The inorganic carbon cycle is represented by total inorganic carbon and alkalinity. The organic carbon cycle includes, in addition to the above described organic components, dissolved and particulate organic matter (DOC, POC). DOC is produced by primary producers mainly under nutrient limitation. DOC eventually flocculates to POC and sinks down. POC and DOC allow for a flexible C:N:P ratio.

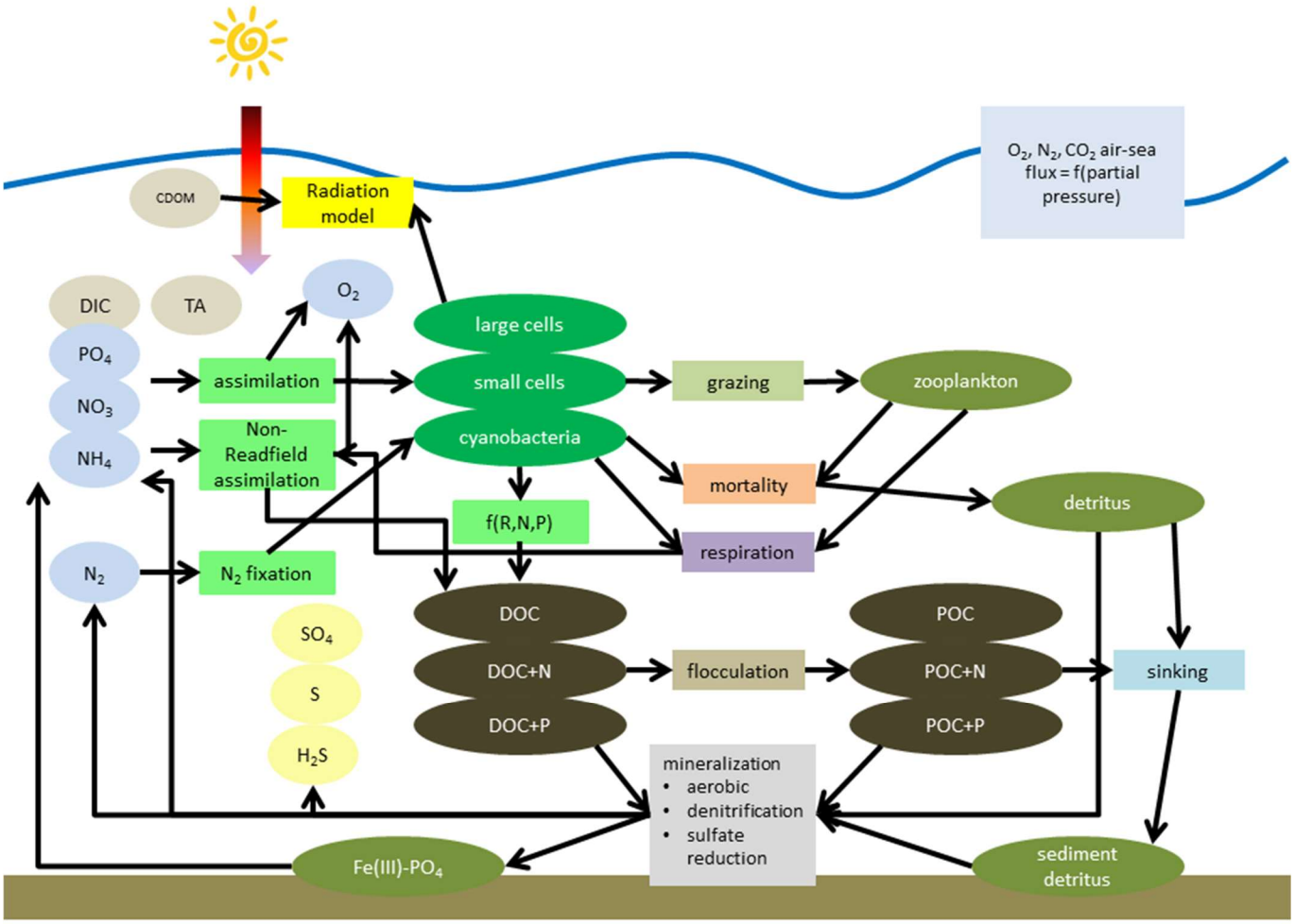

Figure 2-22. Schematic of the biogeochemical model.

The physical part of the model is based on the circulation model MOM (version 5.1) [Griffies, 2004] and has been adapted to the Baltic Sea with an open boundary condition to the North Sea, and riverine freshwater input. The MOM model is complemented with a sea ice model to estimate ice cover thickness and extent. The horizontal resolution of the model grid is three nautical miles, while vertically the model is resolved into 152 layers, with a layer thickness of 0.5m at the surface gradually increasing up to 2m. Both model components are coupled via advection-diffusion equations.

2.5.1 Spatial resolution

The standard setup of the BGC model used at IOW relies on 3 nautical miles (n.m.) horizontal resolution. While this resolution works efficiently for long-term simulations (>50y), the coast-open sea gradient is not sufficiently resolved for the objectives of SeaLaBio. Consequently, the horizontal resolution was increased from 3n.m. to 1n.m.

The new setup required:

- Adaptation of the bathymetry
- Re-gridding of runoff data and open boundary conditions
- Re-calibration of sub-grid parametrizations for horizontal and vertical mixing
- Domain decomposition for parallel computing

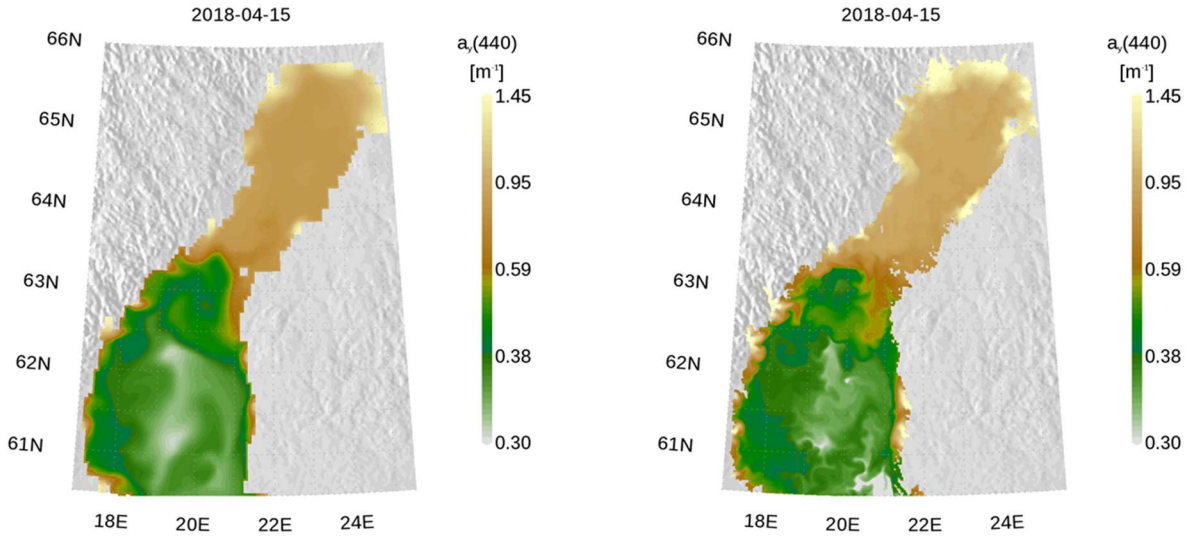

Figure 2-23. CDOM absorption as seen in 3n.m. resolution (left) and 1n.m. resolution (right).

In Figure 2-23, the simulated CDOM absorption is shown for 3n.m. und 1n.m. resolutions. The fine structures resolved in the higher horizontal resolution model are clearly seen. However, CDOM absorption in this model version is derived from salinity based on Neumann et al. (2015).

2.5.2 Explicit CDOM state variable

Salinity as proxy for CDOM is a rough estimate involving some uncertainties. This approach does not consider a CDOM decay which, although on longer time scales, disturbs the salt-CDOM relationship. Another source of uncertainties is the model error for salinity which has a direct impact on the salt-CDOM relationship.

Therefore, the biogeochemical model ERGOM has been extended with an additional state variable CDOM. For CDOM decay, we have implemented a "photobleaching". Ambient light in the water column will de-color CDOM and reduce the light absorption effect of CDOM. In the model, PAR as a measure for ambient light is available. The CDOM decay is:

$$\frac{dCDOM}{dt} = -r_0 * PAR * CDOM$$

A series of calibration simulations for the constant r_0 have been performed and a reasonable r_0 value is available.

The new approach allows for the estimate of land-sea carbon fluxes due to CDOM. A first result shows Figure 2-24. The strong annual cycle is caused by both the runoff cycle and the annual CDOM concentration (absorption) cycle.

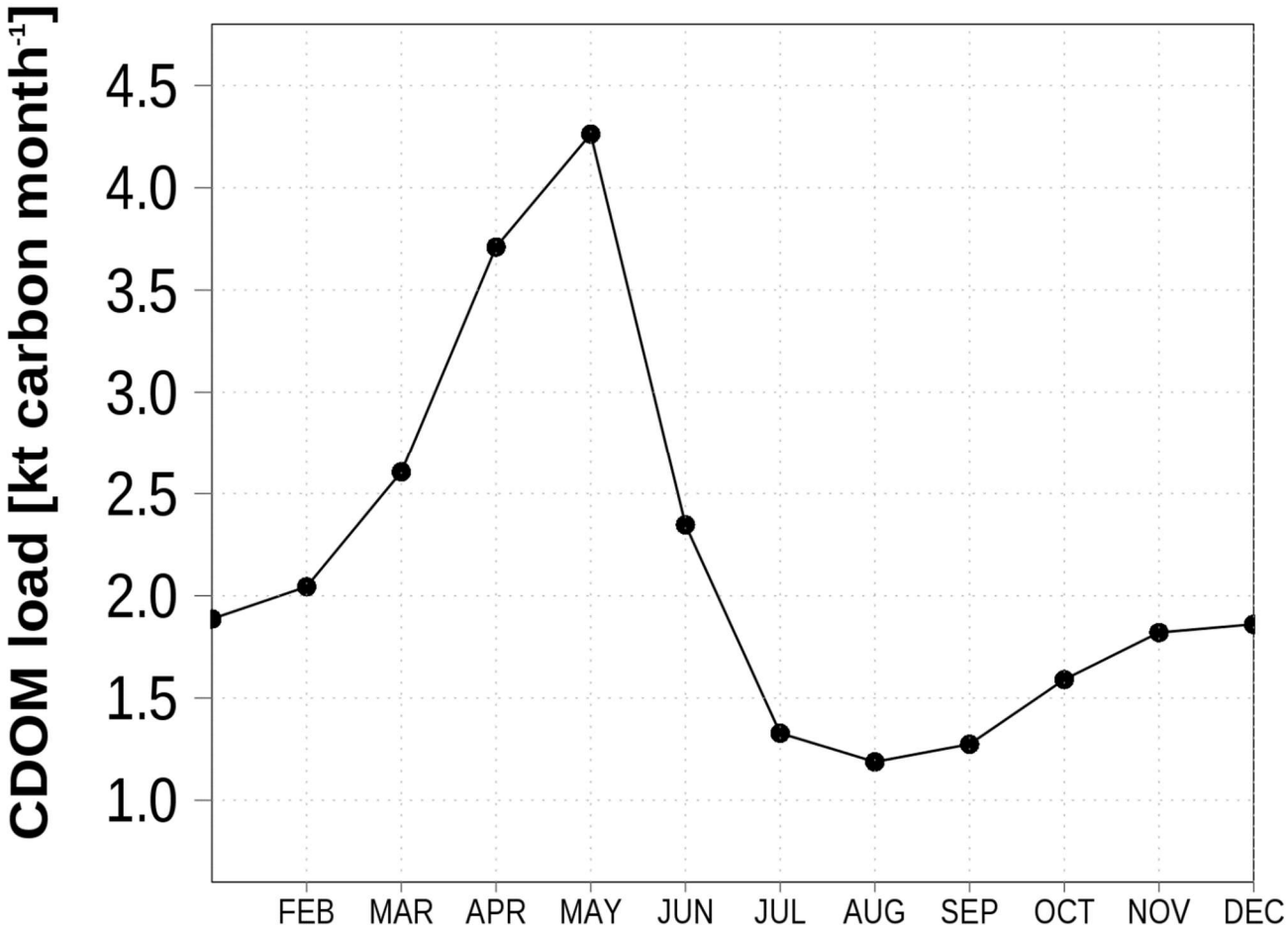

Figure 2-24. CDOM based carbon loads to the Baltic Sea.

The new CDOM variable needs a boundary condition in the river mouths. Therefore, a comprehensive data set for riverine CDOM including about 80 different rivers around the Baltic Sea and the seasonal cycle has been compiled from EO products.

3 Quality assessment and diagnostic

3.1 Quality flags

Currently, there are no quality flags implemented within the atmospheric correction processor. However, the neural network approach allows for simple definitions of quality flags. The input data is checked against the range of the training datasets; only if the data values are inside the defined range, the NN can produce sensible results. In order to allow for meaningful output, the input data is constrained to these ranges. E.g. for reflectances, these values are usually small negatives, which are changed to low positive values. If constraints are used, this should be reflected in a quality flag for each of the NNs (OOS: out of scope, out of training range). Currently, an estimate of the quality of the AC is provided by the reduced χ^2, at convergence. Ideally, when input uncertainties are used in the minimization (i.e. when residuals are scaled by these uncertainties), the χ^2 metrics can be compared to unity: values of the order or below unity mean a good fit between the observation and the model. However, when this

scaling by input uncertainties is not applied, as in the current version of the AC, the χ^2 cannot be directly compared to an absolute threshold. We have observed that the χ^2 is generally of the order of 10^{-6} and higher value occurs for complex situations with dubious spectra (near the shore, inland waters). Examples are provided in the scientific analysis hereafter.

In addition, the results of the pixel identification (especially the detection of clouds) can be added to the suit of flags.

3.2 Product uncertainty

Uncertainties of marine IOPs have not yet been defined. Currently, only uncertainty of the AC, i.e. of marine reflectance, are implemented, as described in section 2.1.10 and illustrated hereafter.

3.3 BGC model validation

In chapter 2.5, the impact of a higher spatial resolution on the reproduction of fine-scale features have been shown. The changed resolution made a re-calibration of sub-grid parametrizations (e.g. turbulence) necessary. Here we show the model performance for temperature and salinity at two stations in the northern Baltic.

Figure 3-1 shows salinity and temperature at HELCOM station F9 in the Bothnian Bay. Both variables are reasonably well reproduced by the model. However, the bottom water temperature in winter is overestimated in some cases by the model. A reason could be that inflow events in winter are not represented sufficiently. Otherwise, the simulated vertical salinity gradient shows that saline bottom water arrives at station F9. There also is a descending trend in the salinity observations (both at surface and at depth), which is not reproduced by the model. The reason for this bias in not known currently. Owing to restricted super computing resources, we are not able to investigate the physical model part for the origin of the bias. Since the bias is pronounced in the most norther model part and only in the last simulation years, we hypothesize that uncertainties in the freshwater runoff data might be a reason. Official runoff data by HELCOM are published with some time delay. Therefore, we use extrapolated data for the last simulation years.

Figure 3-2 shows salinity and temperature at HELCOM station SR5 in the Bothnian Sea. While the surface salinity fits well with observations, the bottom salinity is overestimated. Temperature of surface as well as bottom water is reasonable reproduced. Especially for the surface salinity, the model shows a good performance. This is important, since at the current model development state, CDOM estimates are based on salinity. The CDOM absorption is estimated as: $a_y(440) = 1.26*S^{-0.627}[m^{-1}]$ (Neumann et al., 2015).

Figure 3-3 shows the estimated CDOM absorption at station SR9 for model data and observations and provides an impression, how a salinity bias mirrors in the derived absorption.

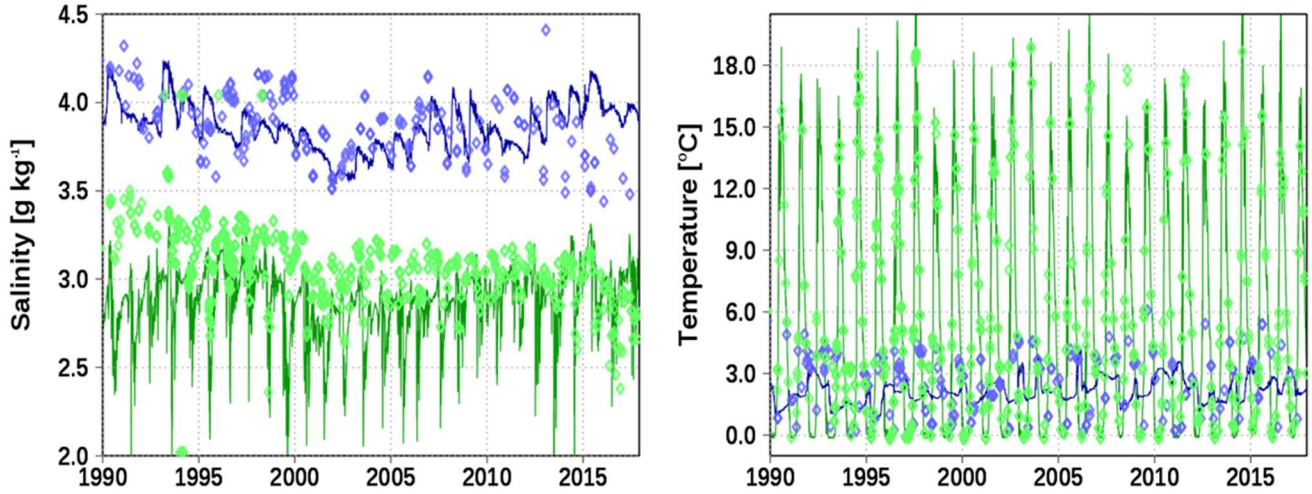

Figure 3-1. Bottom (blue) and surface (green) salinity (left) and temperature (right) at HELCOM station F9 (64.7N 22.03E, see Figure 2-23 for an orientation of stations position). Model data are shown as solid lines and observations as diamonds. Data source: ICES database (www.ices.dk).

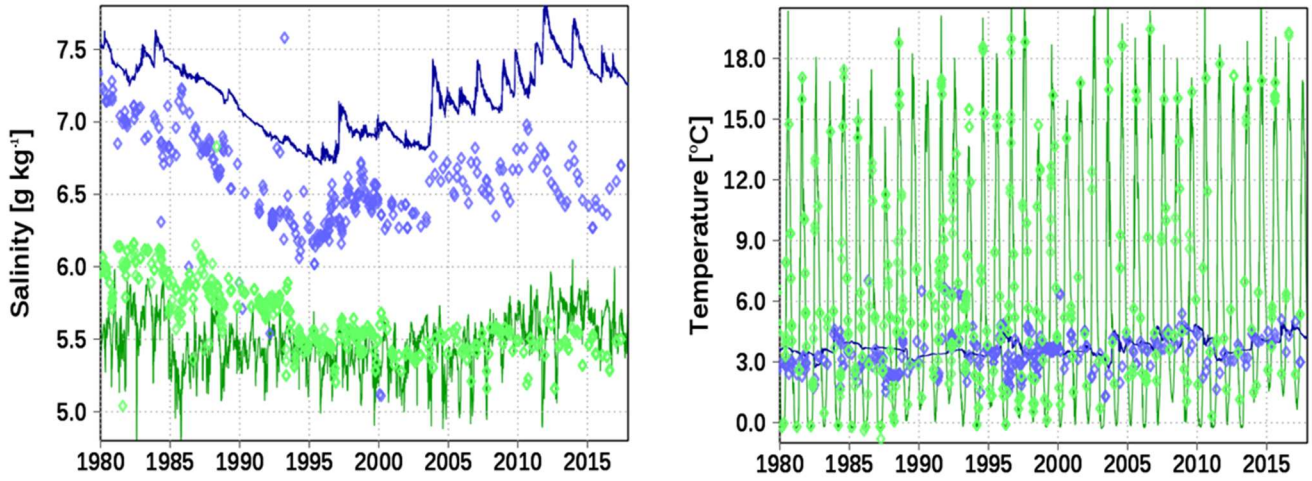

Figure 3-2. Bottom (blue) and surface (green) salinity (left) and temperature (right) at HELCOM station SR5 (61.07N 19.58E, see Figure 2-23 for an orientation of stations position). Model data are shown as solid lines and observations as diamonds. Data source: ICES database (www.ices.dk).

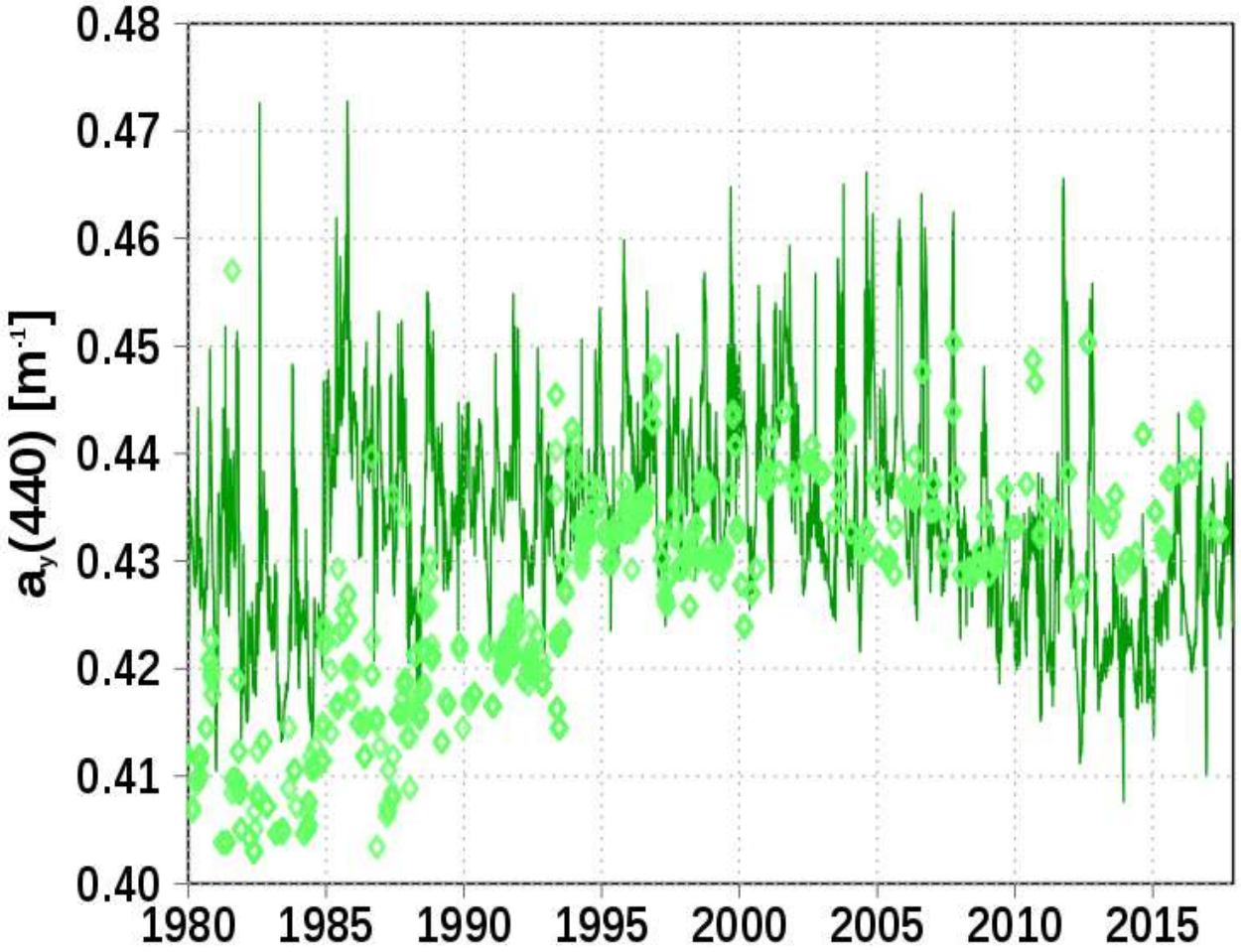

Figure 3-3. CDOM absorption of surface water estimated from salinity at station SR5 in the Bothnian Sea. Solid line: Salinity from model simulation. Diamonds: Salinity from observations.

First simulations with an explicit CDOM state variable are shown in Figure 3-4. We have to note, that the model is not finally calibrated. The relatively higher absorption in the Gulf of Finland due to high CDOM loads from the Neva River is obvious. The salinity approach cannot account for this. In addition, the vicinity of the river estuaries is influenced by the individual CDOM concentration of the specific river.

Figure 3-5 shows an example for the absorption structures in the northern Baltic Sea developing in the 1 n.m. model. Compared to Figure 2-23 (salinity-based approach), the coast – open sea gradient is stronger.

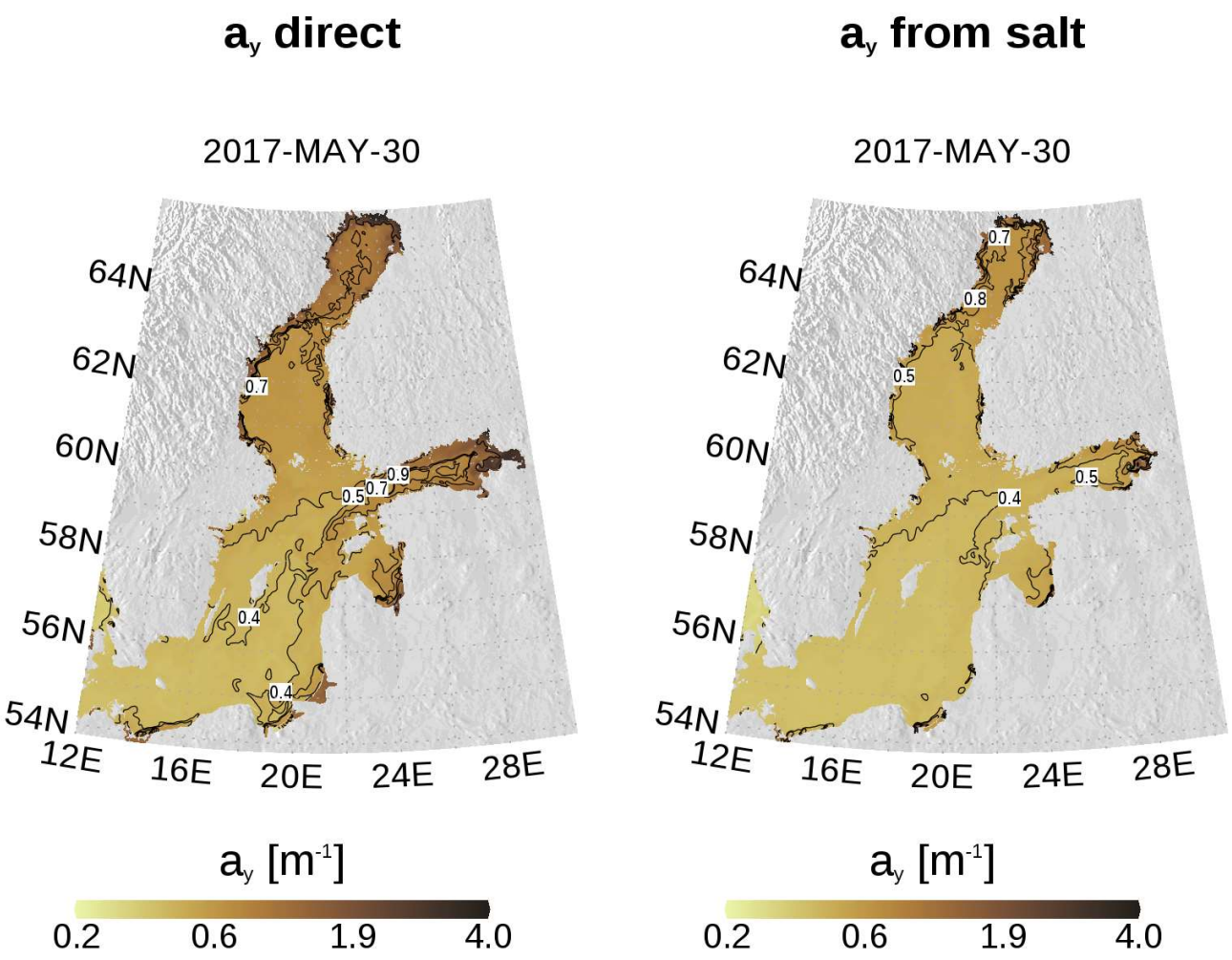

Figure 3-4. CDOM absorption (440nm) in the surface water with an explicit CDOM variable (left) and estimated from a salt-a_y relation (right) simulated with a 1 n.m. resolution model.

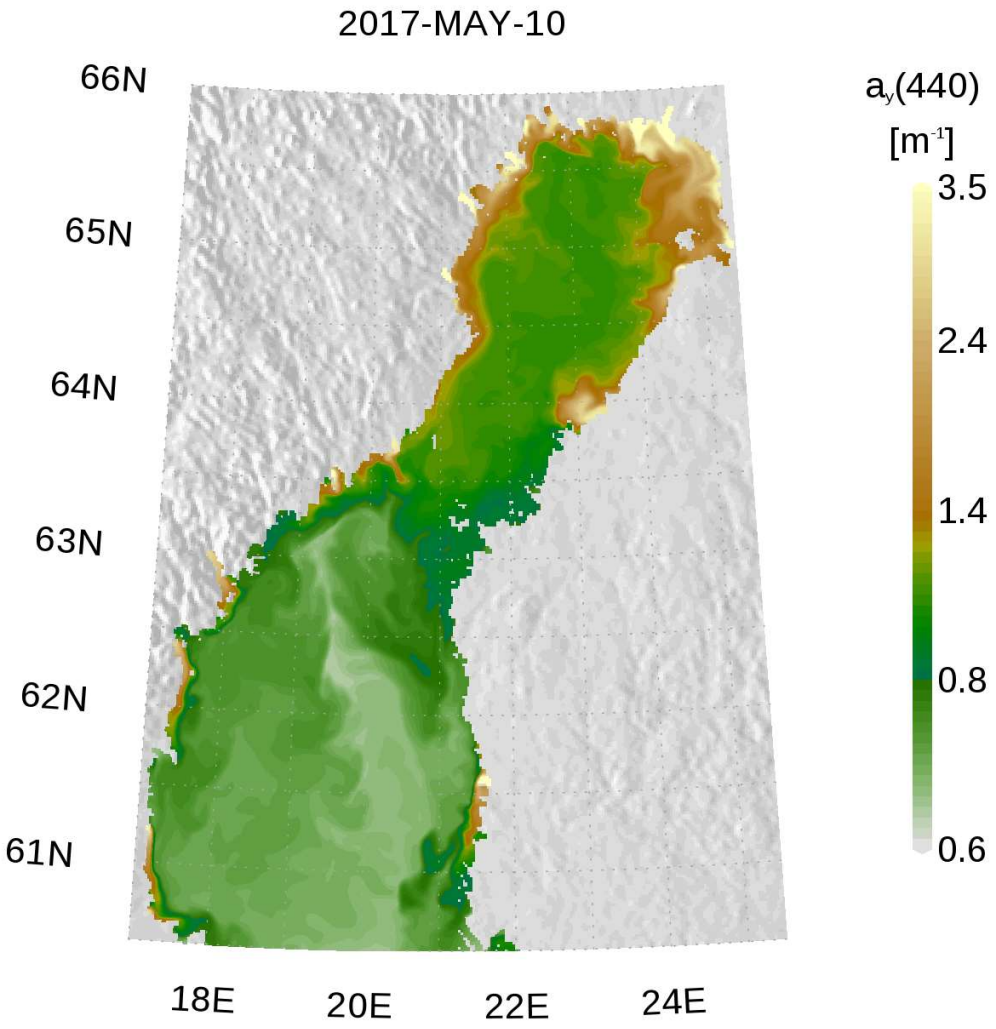

Figure 3-5. CDOM absorption (440nm) in the northern Baltic Sea derived from simulated CDOM concentration (1n.m. model version).

Figure 3-6 shows CDOM absorption time series at 3 central stations. Variations may be due to a direct impact of river plumes or to different water masses. Especially, the absorption increase in summer in the Gotland Sea is the result of less vertical mixing and increasing impact of surface water. A validation is planned after the calibration has been finished and we will report about it in the Impact Assessment Report.

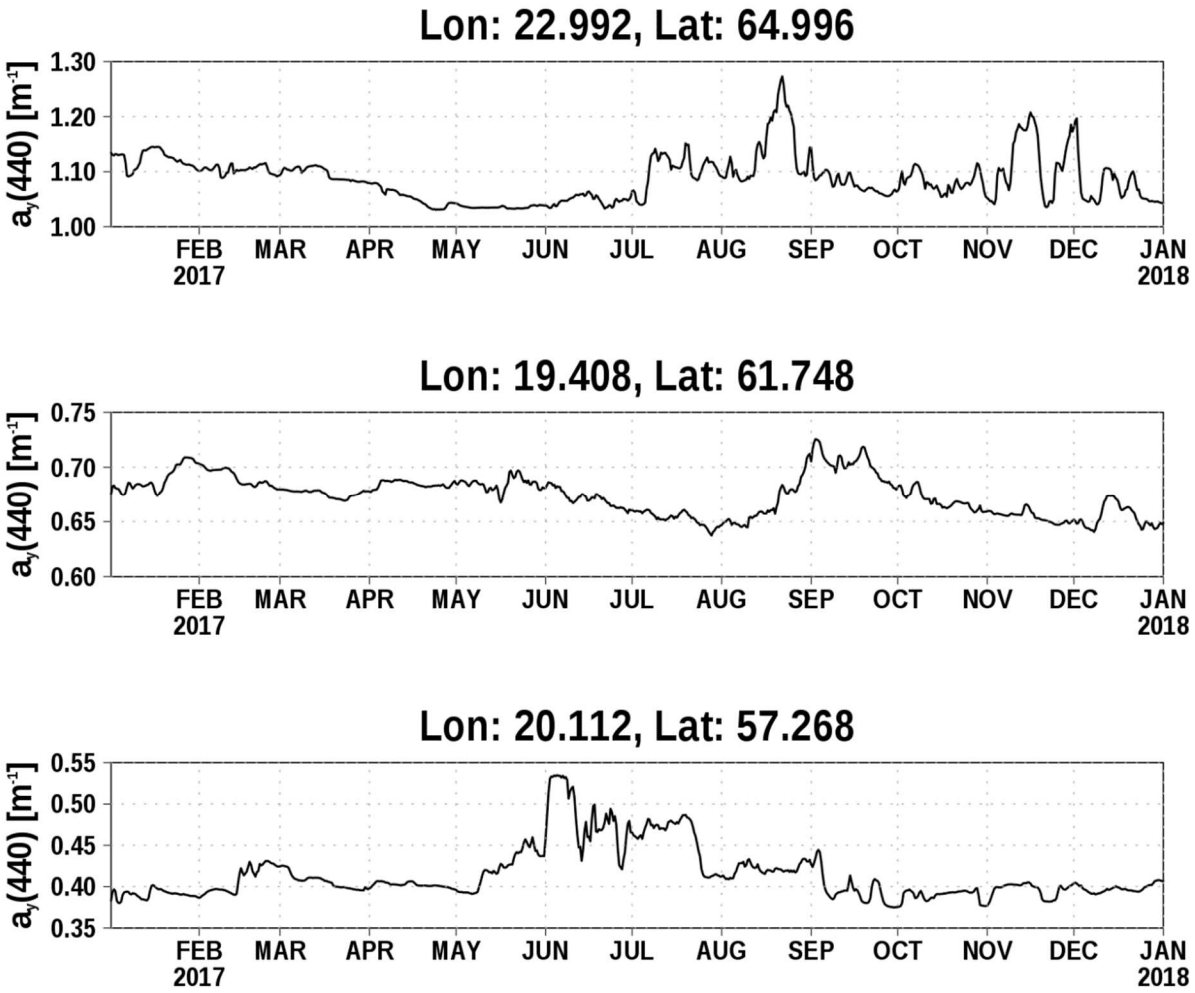

Figure 3-6. Time series of CDOM absorption (440nm) at 3 central stations: Bothnian Bay (upper panel), Bothnian Sea (middle panel), and Gotland Sea (lower panel).

4 Scientific analysis

Note: the detailed description of the error and validation analysis as well as the cross-comparison experiment exercise are reported in the Validation Report of the project.

4.1 Atmospheric correction

Various analyses have been performed to justify and check relevance of the AC scheme.

4.1.1 OLCI match-ups analysis

Comparison of the OLCI marine reflectance processed by Baltic-AC with in situ data from three AERONET-OC sites relevant for Baltic+ are shown in Figure 4-1 (Gustav Dalen Tower, Helsinki Lighthouse and Palgrunden). Vertical lines represent the uncertainty (+/- one sigma) computed in the AC. A systematic overestimation at 412 nm is observed, a behavior also occurring for other ACs (see Validation Report for a more detailed comparison). Interestingly, the issue is confirmed by the relatively large uncertainties for that band. In the green and red bands, the AC is performing reasonably well, considering the low signal of these waters. It should be emphasized that the inverse problem solved by the AC is sensitive to the marine model (forward NN) and also to IOPs identified in the first guess. To illustrate this sensitivity, the same validation plots are given on Figure 4-2 when considering another backward NN in the first guess. Data are more scattered, yielding a reduced number of match-ups and increased uncertainty, but the systematic bias is generally reduced (marine reflectance at 665 nm is no longer underestimated).

4.1.2 Representativity of the marine model

The marine model ρ_w^{mod} has a key role in the AC since it constrains the aerosol reflectance during the minimization process. Application of the AC in other water types than those used to build the forward NN shows degraded results. On the example given in Figure 4-3 for the Venice site in the North Adriatic Sea, the performance of the AC is reduced over the totally different range of radiometry from 412 to 560 nm. It is likely that the marine model trained in the Baltic is not suitable to such waters. One may wonder about the representativity of this model even in the Baltic Sea, from a theoretical point of view, independently of the AC. Ideas for such analysis are

- Inversion of the marine signal only, without atmosphere, from in-situ measurements;
- Tests with various versions of the forward NN

4.1.3 Chi-square and uncertainty analysis

Maps and plots of χ^2 and of marine reflectance uncertainties are illustrated for two different regions and water types on Figure 4-4, Figure 4-5 and Figure 4-6. χ^2 is generally as low as 10^{-6}, but much higher value appears in small complex areas where the AC fails (typically negative reflectance). Hence χ^2 can be used as a measure of the quality of the inversion. It is also well related to the uncertainty map, this latter having however the advantage to give a spectral information on the trustiness of the inversion. The absolute value of the uncertainty is strongly related to the level of the marine signal. In the northern Gulf of Bothnia, where the radiometry is extremely low, the absolute uncertainty is below $5*10^{-4}$, except at 443 were it is below 10^{-3} and further in the blue bands where it increases. These are very small values. Uncertainties are significantly higher along the south west coast of Finland, especially over the turbid plume of the river Kokemäenjoki. As shown previously on the match-ups, higher uncertainties do not necessarily mean that the marine reflectance are biased. The uncertainty estimate is a valuable metric to investigate the relevance of the marine model and the spectral fit. Uncertainties on retrieved marine reflectance would likely be reduced if the input uncertainties on ρ_w^{mod} would be known and handled in the minimization (typically, with higher uncertainties in the blue band).

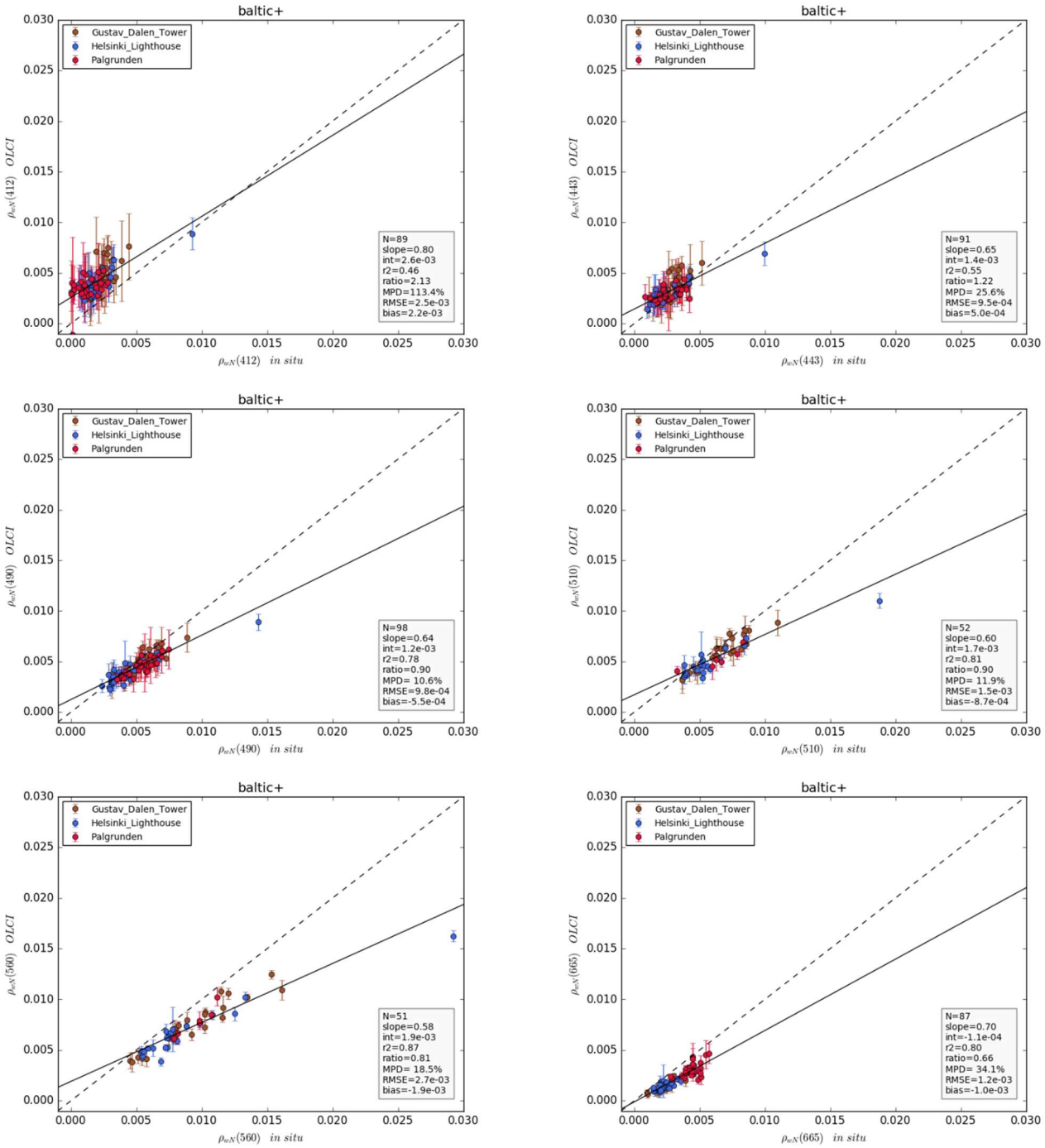

Figure 4-1. Comparison of Baltic-AC marine reflectance (y-axis) with AERONET-OC measurements (x-axis).

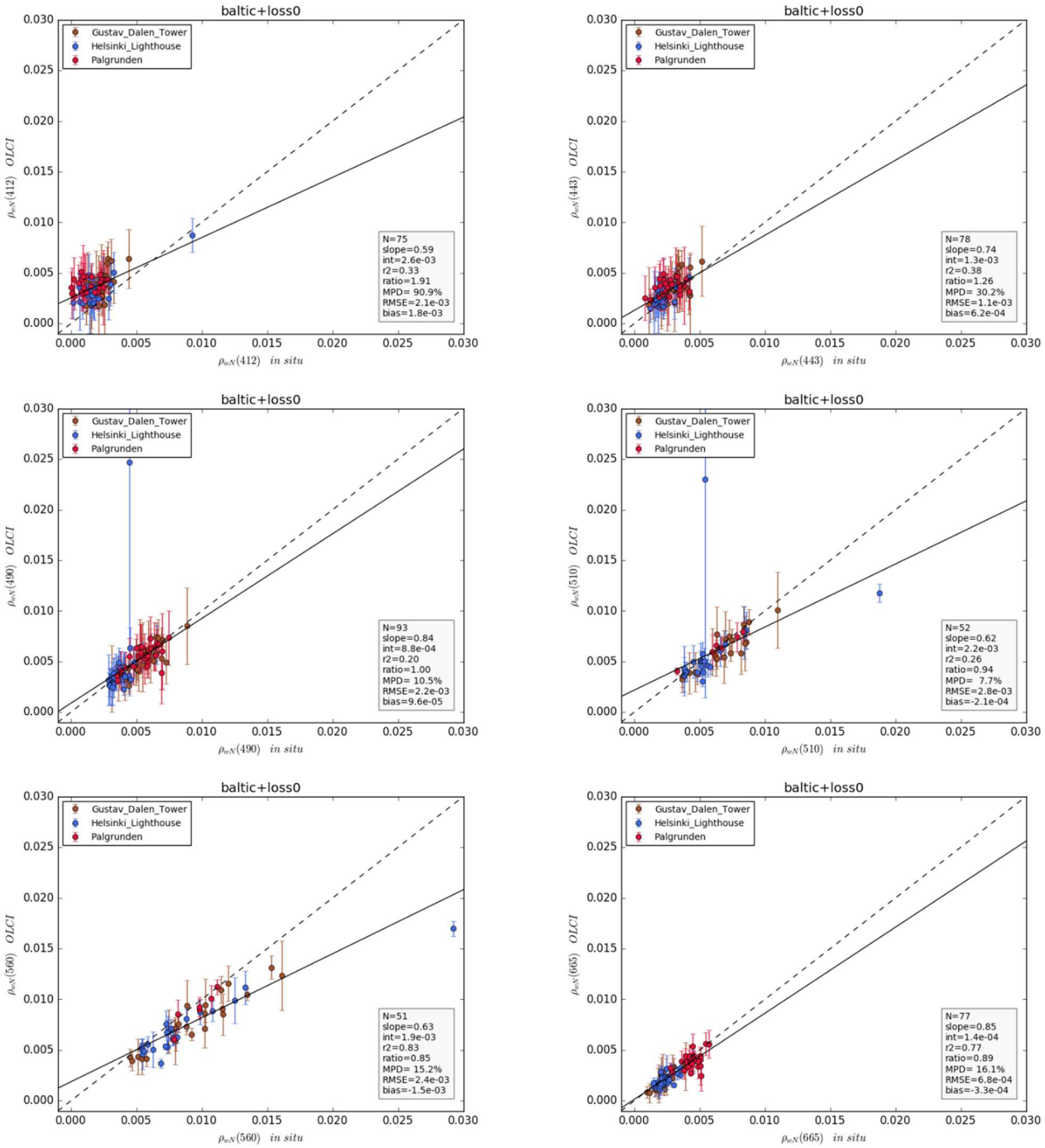

Figure 4-2. Same as Figure 4-1 but for another tentative backward NN used in the first guess.

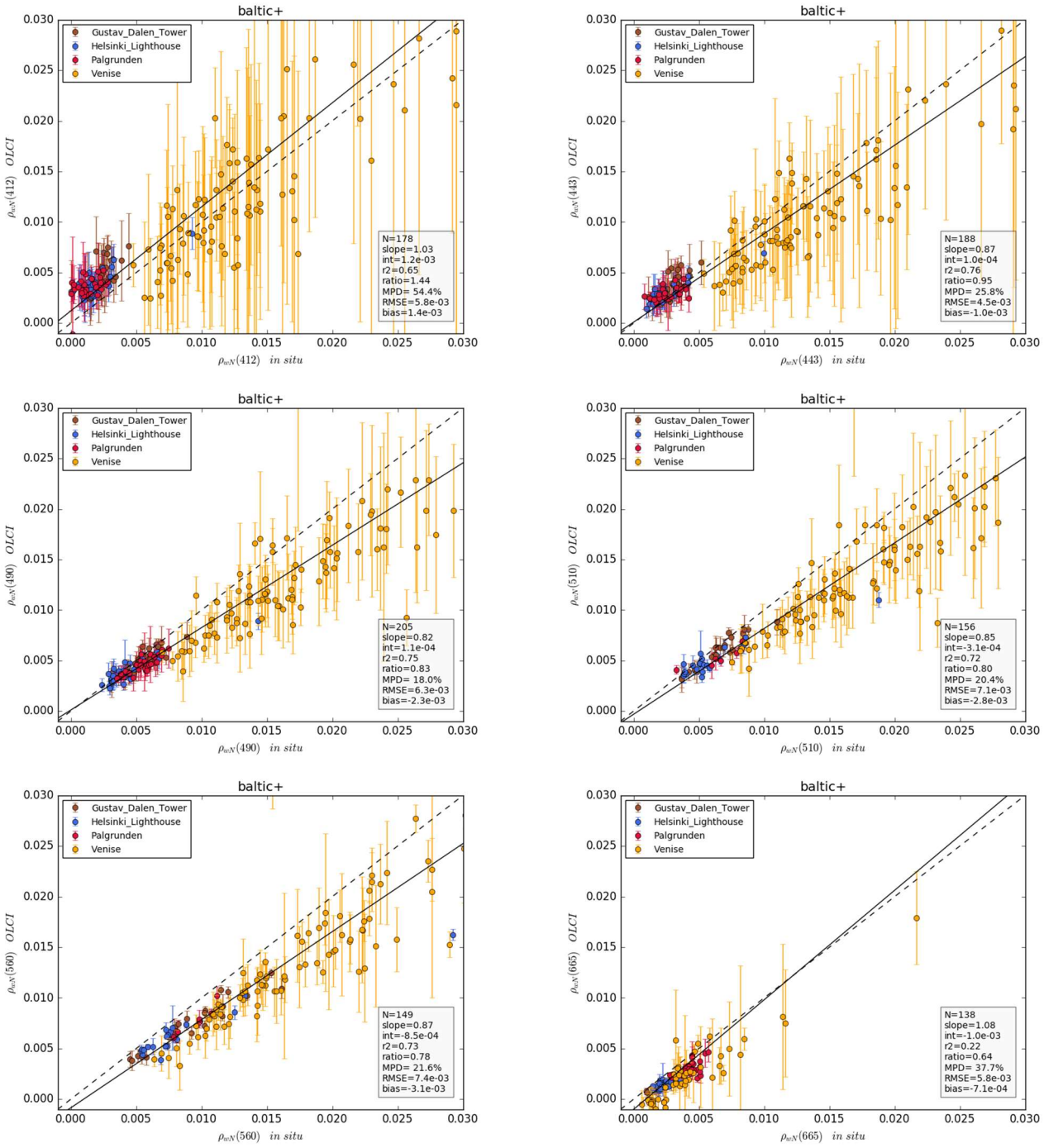

Figure 4-3. Same as Figure 4-2 with another site in the North Adriatic Sea (Venise).

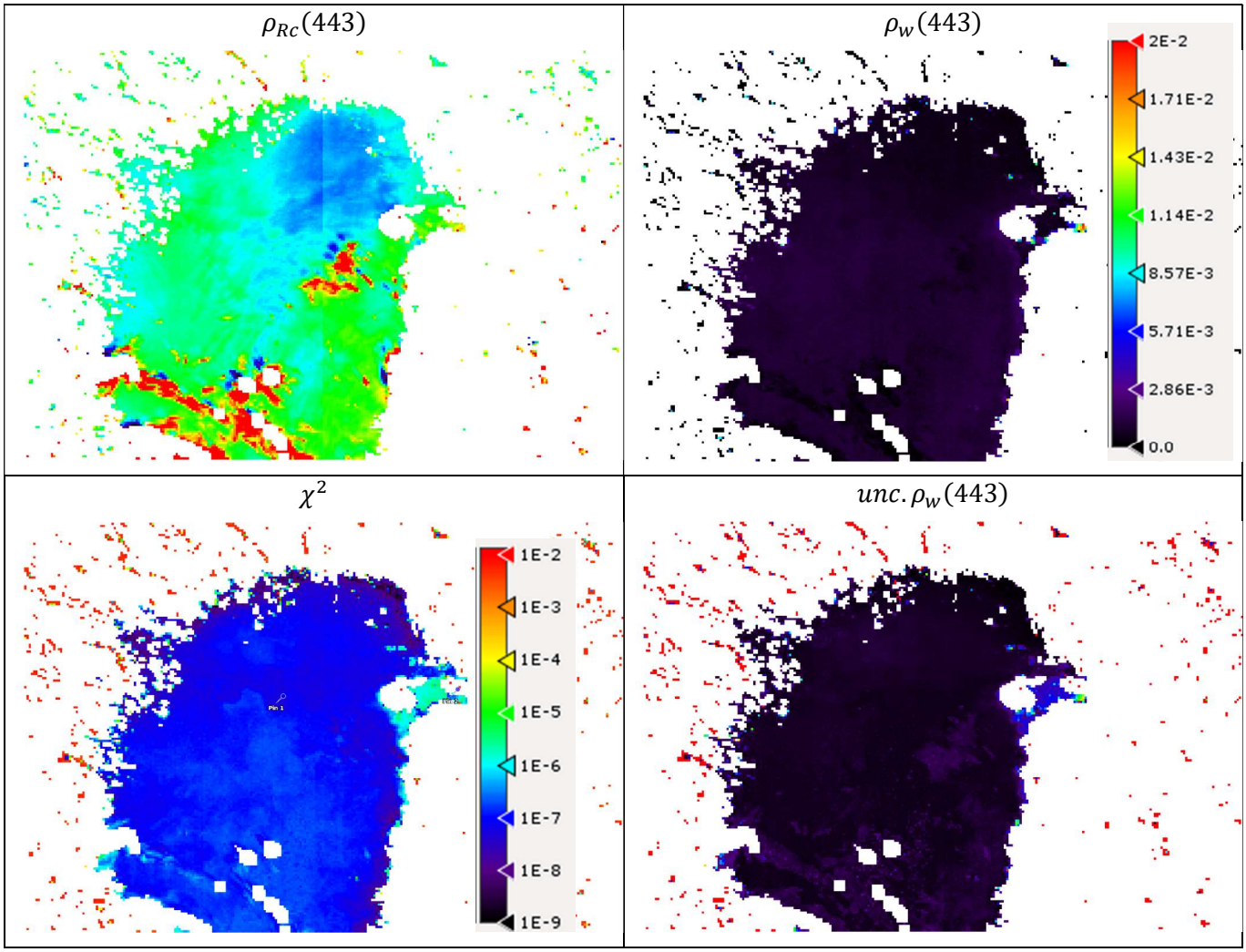

Figure 4-4. Analysis of Baltic+ AC in northern Gulf of Bothnia (OLCI-A, 20180602). Same colour scale for ρ_{Rc}, ρ_w and $unc.\,\rho_w$ (top right colour bar).

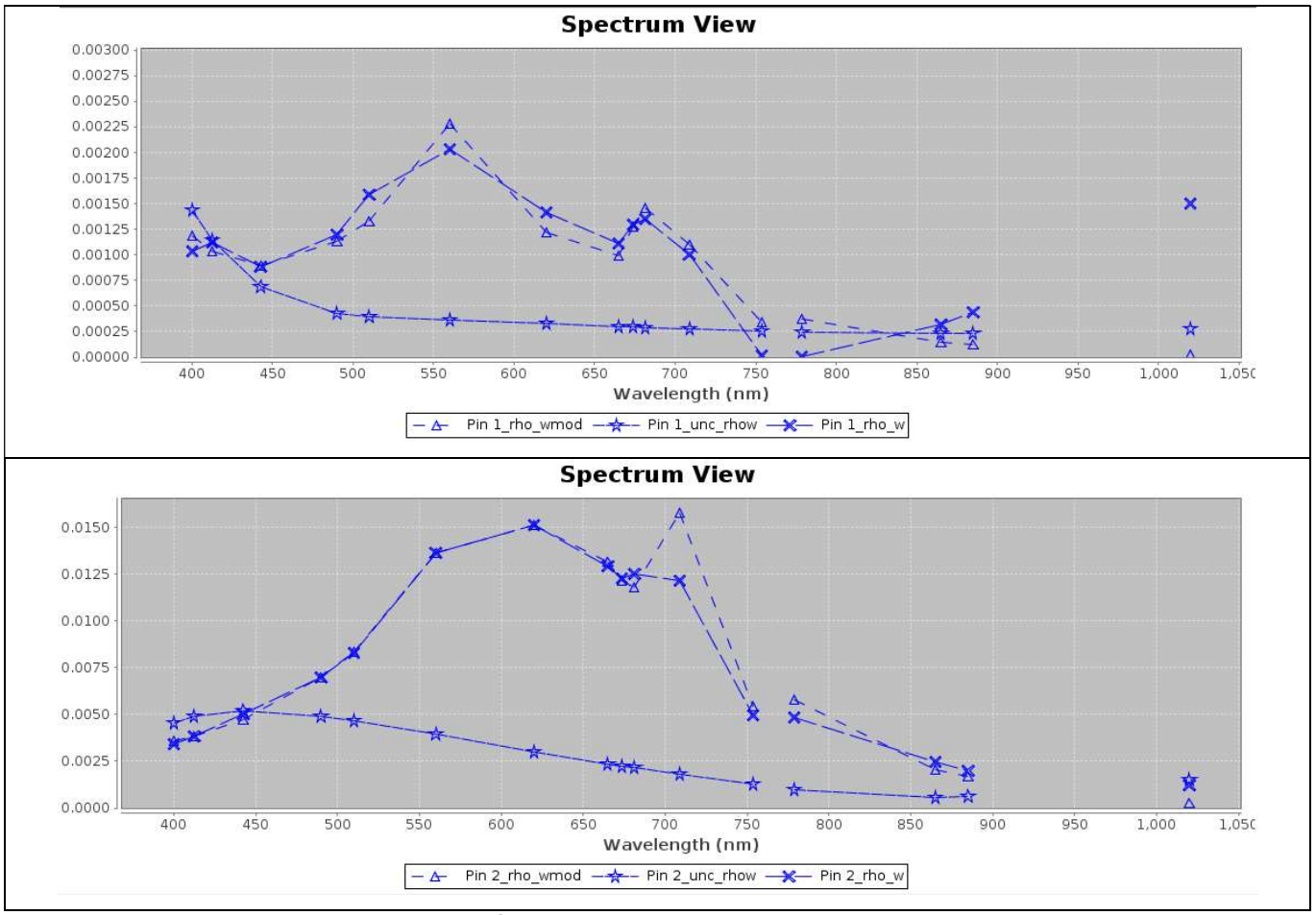

Figure 4-5. Spectral plot of ρ_w (crosses), ρ_w^{mod} (triangles) and uncertainty of ρ_w (stars) over two pixels in the Gulf of Bothnia: absorbing water pin the middle of the Gulf (top graph) and bright waters near the shore (bottom graph).

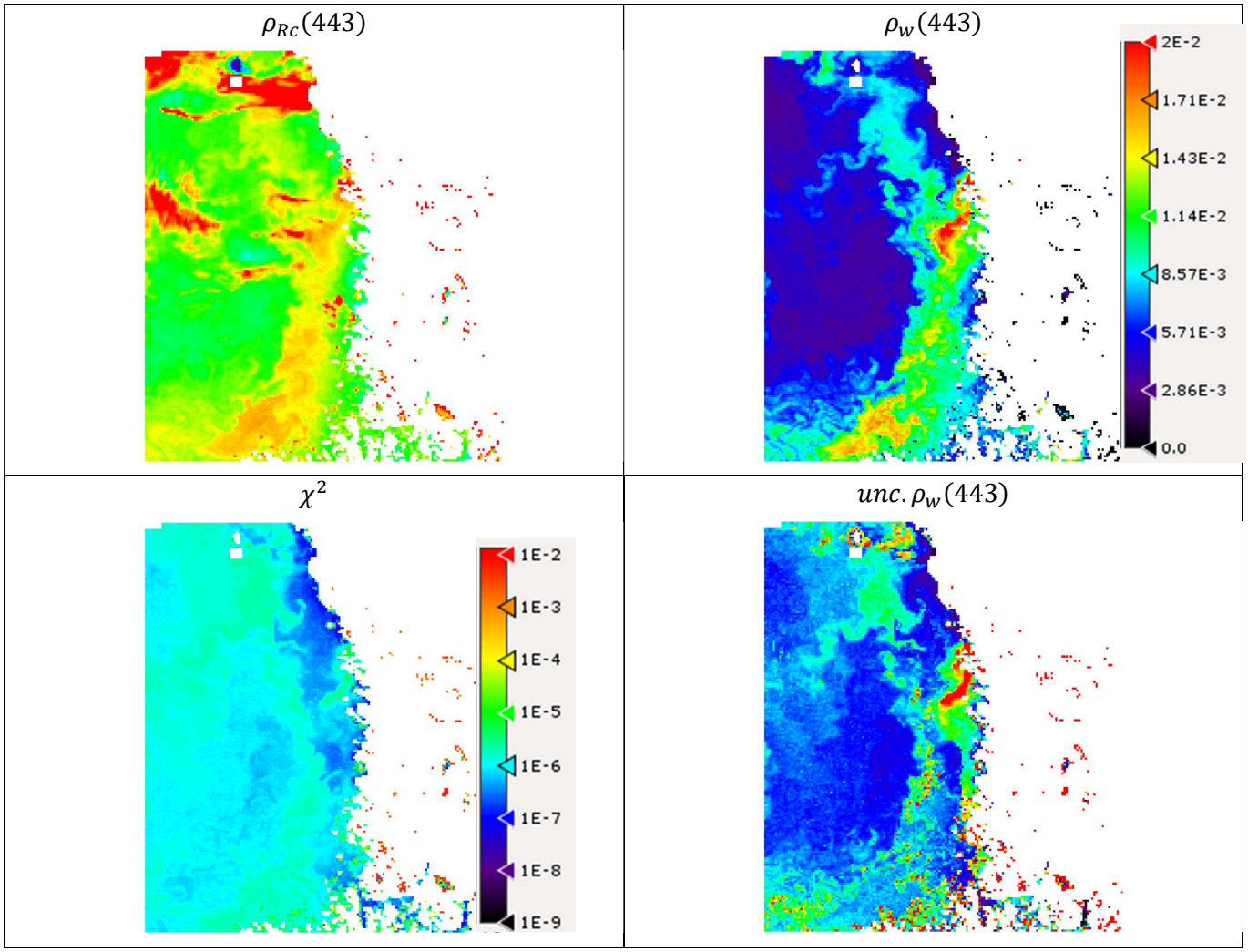

Figure 4-6. Analysis of Baltic+ AC on the estuary of the Kokemäenjoki river (OLCI-B, 20190415). Same colour scale for ρ_{Rc}, ρ_w and $unc.\,\rho_w$ (top right colour bar).

4.1.4 Consistency of Baltic+ AC for S2

Applicability of the spectral matching AC to S2 is more challenging due to the limited number of bands of the sensor, and lower signal-to-noise ratio, compared to OLCI. The consistency of the results for S2 are analysed at two levels:

- Internally, by comparing the output ρ_w provided by the AC with the best ρ_w^{mod} identified in the inversion; we remind that the principle of the AC is to minimize the discrepancy between both spectra. On Figure 4-7 we see that the minimization method works well over a large range of radiometry and spectral shapes.
- By comparing the normalized marine reflectance of OLCI and MSI over common acquisitions (possibly with a few hours delay). Figure 4-8 illustrates the spectra at 560 and 655 nm, which are the two bands considered in the project to compute CDOM (see Validation Report). The S2 data, while noisy, allows to see small patterns unreachable on the OLCI image (reduced resolution) but both data are very consistent in term of level of radiometry, for the coastal and more off-shore regions. In comparison, S2 reflectance provided by C2RCC at these bands is totally different and likely overestimated if we trust the OLCI data.

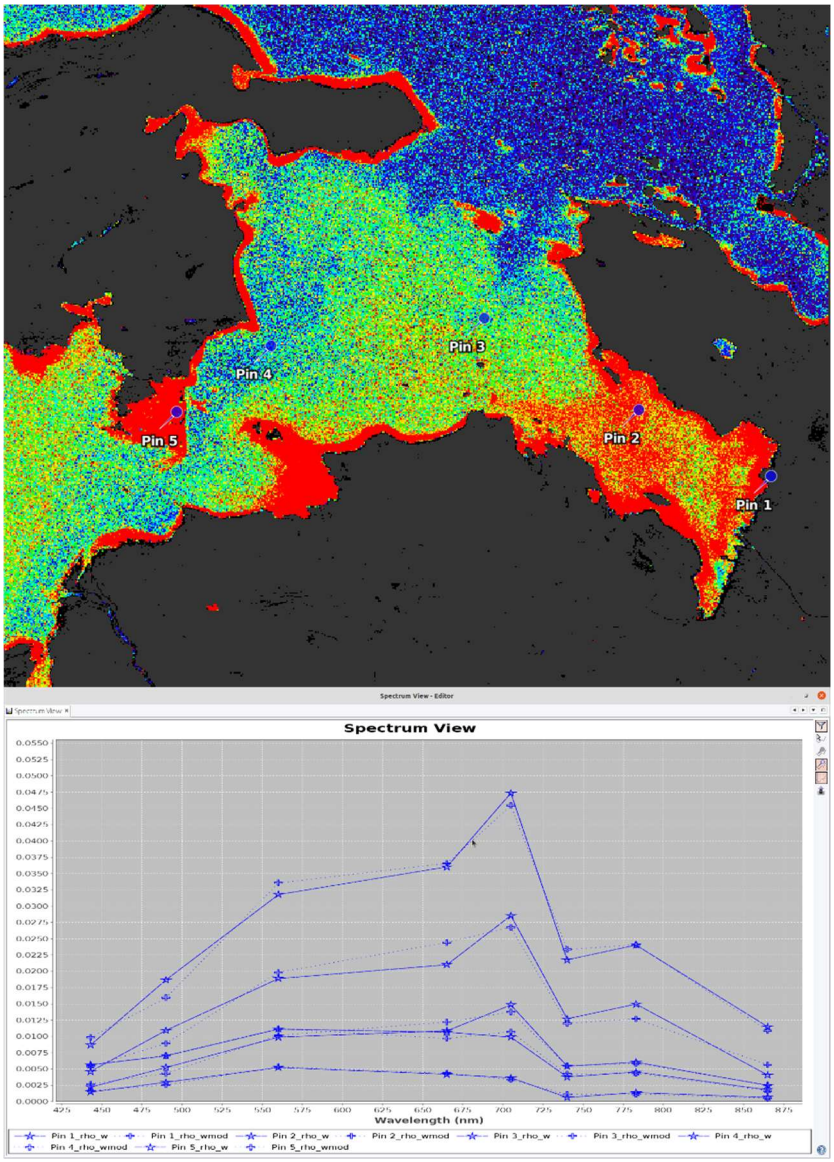

Figure 4-7. Analysis of Baltic+ inversion for S2 acquisition in Gulf of Bothnia (14.05.2018). Top: positions of 5 reference points (pins1 to pins 5). Bottom: marine spectra ρ_w (star) and best model ρ_w^{mod} (crosses) provided by the Baltic+ processor over the five points.

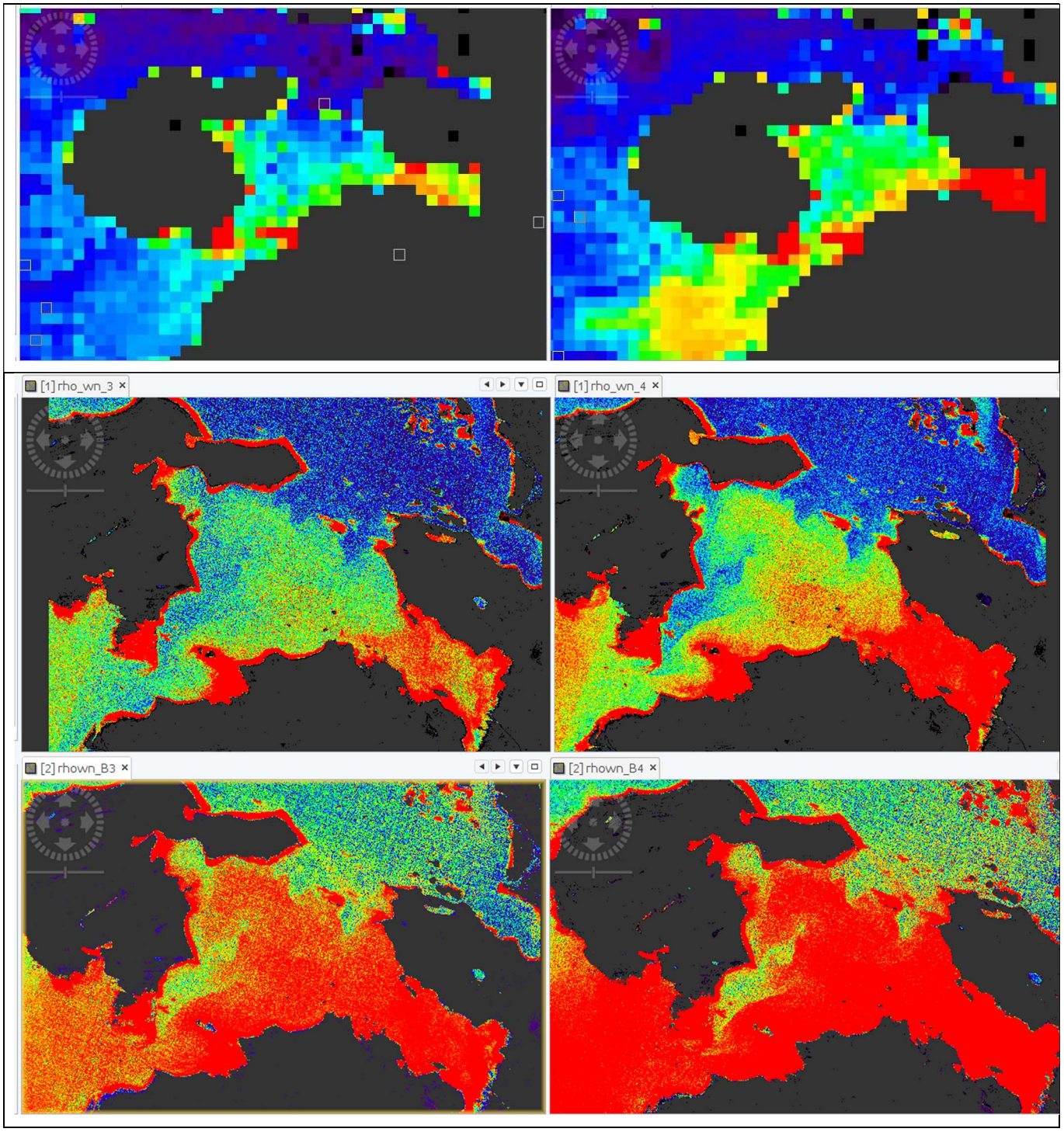

Figure 4-8. Normalized marine reflectance at 560 nm (left) and 665 nm (right) over the Gulf of Bothnia on 14.05.2018, by three processors (top to bottom): OLCI processed by Baltic+, S2 processed by Baltic+ and S2 processed by C2RCC.

4.2 Bio-optical model simulations

4.2.1 Validating simulation spectra of water leaving reflectance against in-situ spectra

The analysis of band ratios in in-situ data showed strong correlations to CDOM absorption. These relationships can be utilized as tests for the simulated spectra, which are computed based on IOP combinations generated according to the Baltic Sea bio-optical model and the radiative transfer model implementation in Hydrolight.

The angle dependent simulation spectra are normalized by applying the ratio of predictions from the fwNN with the angles set to nadir view and zenith sun or the given observation geometry. The normalized spectrum is then:

$$\rho_w^{Norm} = \rho_w(\theta_s, \theta_v, \Delta\phi) * \frac{\text{fwNN(IOP, 0,0,0)}}{\text{fwNN(IOP, }\theta_s, \theta_v, \Delta\phi)}$$

The IOPs are taken from the Hydrolight simulations and they have been the input in the simulation process. That way, the test of the band ratio algorithms is performed entirely in the simulation world.

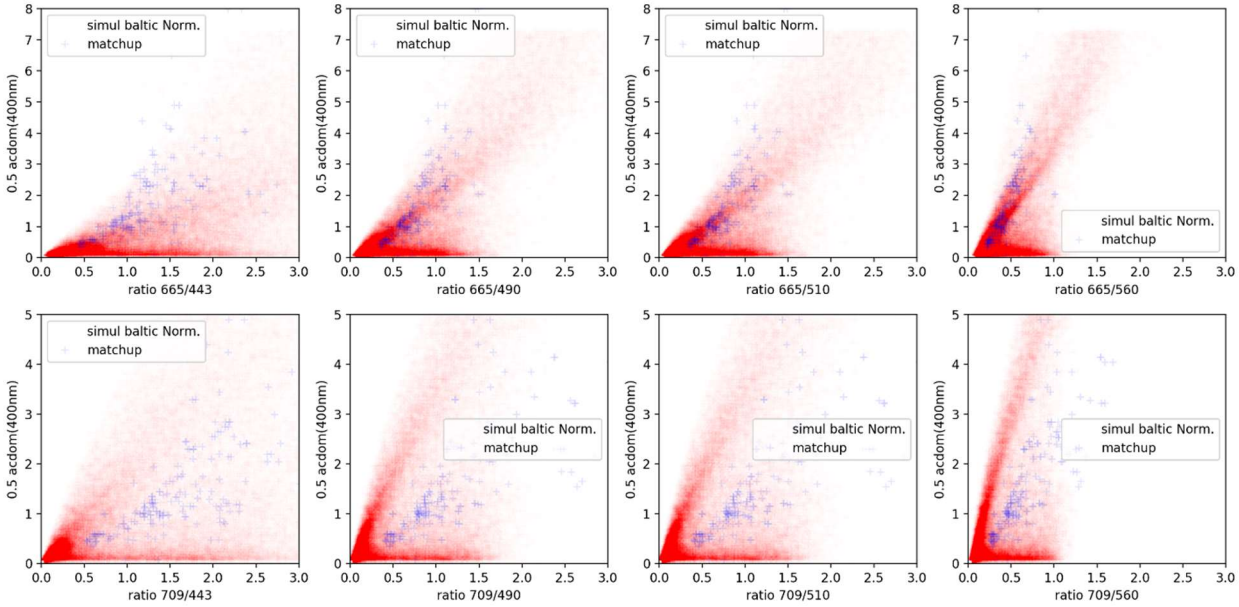

Figure 4-9. Band ratios of normalized water leaving reflectances of simulation data (red) in comparison with in-situ match-up data of OLCI rho_w processed with the Baltic+AC (blue).

The water leaving reflectances of simulation data (see Figure 4-9, red) and the in-situ match-up data of OLCI processed with the Baltic+AC (blue) are both normalized by using the ratio of modelled rho_w spectra (see formula above). The pair of reciprocal neural networks is used to derive with the backwardNN an estimate of IOPs from the in-situ spectra, which are in turn the input to the forwardNN. The spectra are predicted for this set of IOPs and two geometries, the one representing the fully normalized conditions with all angles set to zero and the observation conditions. With the simulations IOPs are given, which are input to the normalization procedure.

The band at 709nm is not part of the minimization process in the AC, due to uncertainties in the water vapour correction. There is a systematic difference between the ratios of simulated spectra and AC-corrected OLCI spectra, if the band at 709nm is considered (bottom row).

Similar to the match-up data, the simulated band ratio 665/560 shows the clearest dependency between normalized rhow and the CDOM absorption. The match-up data and the simulations are showing similar relationships in the upper branch of the cases covered in the simulations (upper right).

The lower branch in the ratios originates in IOP combinations with high chlorophyll concentration and high total backscattering with at the same time low CDOM absorption. These cases do not occur in the Baltic Sea.

4.2.2 Validating the normalisation approach based on simulation data

During the simulation process, spectra have been calculated, which model the observation in nadir view, while the sun geometry does not change. With these spectra, the quality of the normalisation procedure by the fwNN predictions can be analysed.

The validation uses the spectra in nadir view as reference and compares the (partly) normalized spectra with them, leaving the sun angle unchanged, but setting view zenith and azimuth difference to zero.

$$\rho_w^{Norm*} = \rho_w(\theta_s, \theta_v, \Delta\phi) * \frac{fwNN(IOP, \theta_s, 0,0)}{fwNN(IOP, \theta_s, \theta_v, \Delta\phi)}$$

IOPs are taken from the HL table of simulations directly.

The normalisation works quite well (Figure 4-10), as the example spectra show. The angle dependent spectrum (red line) can be successfully transformed into an estimate of the spectrum in nadir view (green), which catches shape and absolute values of the simulated nadir view spectrum (blue) quite well. Exceptions in the quality arise at bands with 674 and 681 nm central wavelength. These bands have known larger uncertainties in their prediction with the fwNN (see Figure 2-15, Figure 2-16) so that the normalisation might not work as well here as at other wavelengths.

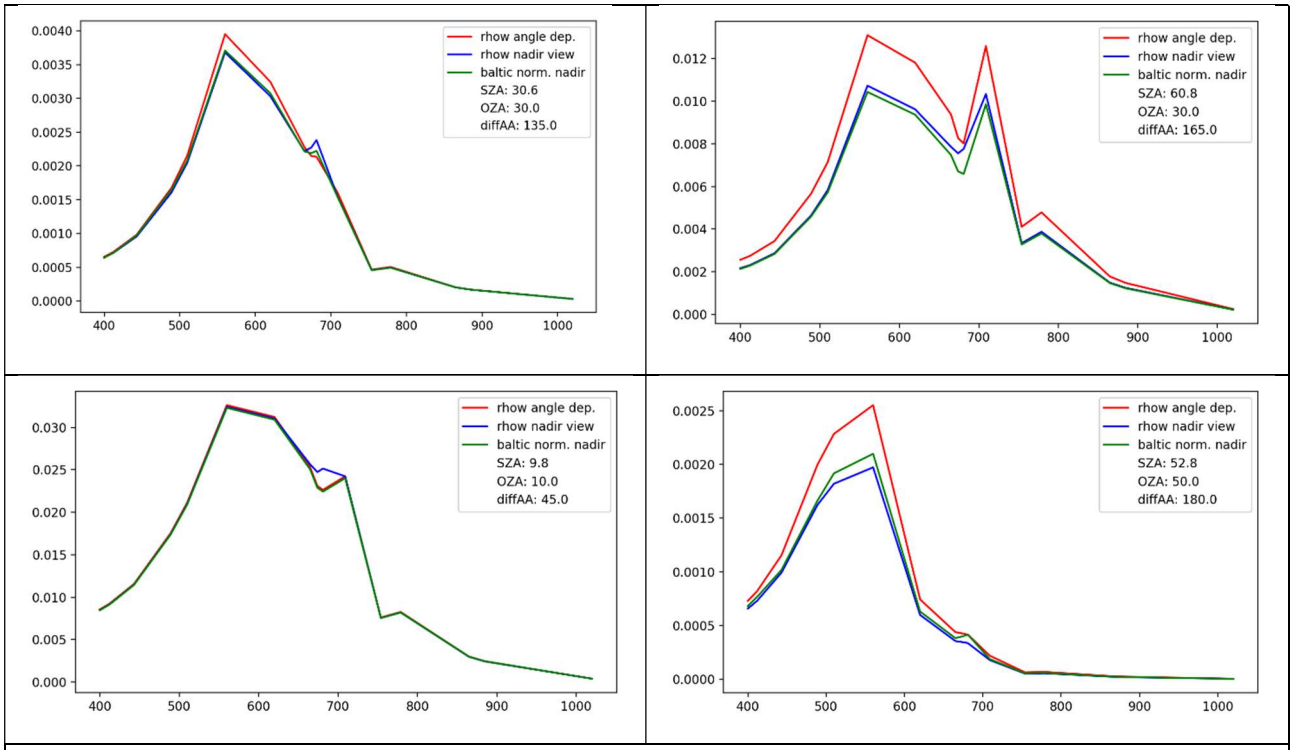

Figure 4-10. The normalized spectrum (to Nadir view, green) should agree with the simulated spectrum in Nadir view (blue). The angle dependent spectrum (red) is multiplied with the ratio of fwNN spectra. The procedure works quite well, with the exception of the bands at 674 and 681 nm.

4.3 In-water processing

See the Validation Report.

4.4 BGC model

Figure 2-23 clearly shows the improved representation of small-scale features by applying a higher horizontal model resolution. The added value is that the model results potentially become more comparable with EO products. This is important for validation and calibration of models with EO products. Furthermore, strong coast-open sea gradients are reproduced more realistically and improve the model performance in coastal areas.

At the beginning of the project, the BGC model estimated CDOM based on a salinity-CDOM correlation. With the projects progress, it becomes obvious that the BGC model benefits from EO derived CDOM data. Therefore, CDOM was explicitly implemented in the BGC model. The technical implementation is completed, CDOM forcing data (riverine loads) have been prepared, and calibration simulations have been finished.

5 Practical considerations

5.1 Input and output description

5.1.1 Atmospheric correction

The table for input/output description is given below. Inputs and outputs are defined per pixel for the satellite sensor. Ancillary data come from external sources possibly at coarser resolution (e.g. meteo data), and are interpolated at pixel level, either already in the Level 1 product (e.g. OLCI) or in the preprocessing of the AC (e.g. MSI).

Table 2: Input (i), ancillary (a) and output (o) data of the AC.

Type (i/o)	Variable	Description
i	λ	Wavelength (integrated for SRF)
i	θ_s	Solar zenith angle
i	θ_v	View zenith angle
i	$\Delta\varphi$	Relative azimuth angle
i	lat	latitude
i	lon	longitude
i	Lt	TOA radiance (OLCI)
i	$\rho_t(\lambda)$	TOA reflectance (MSI)
a	H2O	Water vapour content
a	NO2	Dioxide nitrogen content
a	O3	Ozone content
a	P	Pressure at sea level
a	w_u	Zonal wind speed
a	w_s	Longitudinal wind speed
o	$\rho_a(\lambda)$	Aerosol reflectance, including multiple scattering with Rayleigh
o	ρ_{path}	Path reflectance ($\rho_a + \rho_R$)
o	$\rho_w(\lambda)$	Marine reflectance
o	$unc\_\rho_w(\lambda)$	Uncertainty of marine reflectance
o	$t(\lambda)$	Total diffuse transmittance, accounting for aerosol and Rayleigh contribution, downward + upward
o	χ^2	Cost function of the NLLSQ minimization
o	flag	Quality flag – to be described

5.1.2 BGC model

Forcing data (chap. 5.2.2) are needed in NetCDF format. Output format of the model is also NetCDF. Usually, all state variables and the main process rates are diagnosed as monthly means. At selected stations daily/hourly means are available. However, MOM (see also chap. 5.3.2) has the possibility to adapt the output easily to the needs.

5.2 Auxiliary data

5.2.1 Atmospheric correction

LUTs for OLCI gaseous correction and Cox & Munk reflectance model come from ADF of OLCI Level-2 ground segment (available on EUMETSAT data portal). Rayleigh LUTs come from POLYMER code (Steinmetz et al., 2011), computed by the Successive Order of Scattering radiative transfer code (Lenoble et al., 2007). Meteorological data for S2-MSI come from NCEP.

5.2.2 BGC model

For atmospheric forcing, a dynamical downscaling of the NCEP/NCAR reanalysis is used (https://cera-www.dkrz.de/WDCC/ui/cerasearch/entry?acronym=coastDat-2_COSMO-CLM). Runoff data, riverine nutrient loads, and atmospheric depositions are derived from HELCOM data and assessments (http://www.helcom.fi/helcom-at-work/projects/completed-projects/plc-5-5/, http://www.helcom.fi/baltic-sea-trends/environment-fact-sheets/hydrography/total-and-regional-runoff-to-the-baltic-sea/). The bathymetry is derived from www.io-warnemuende.de/topography-of-the-baltic-sea.html.

5.3 Software implementation

5.3.1 Atmospheric correction

The AC is developed in Python, using the SNAP API for Python (snappy module). The input/output operations on S2 and S3 data, as well as the NN operators, are thus handled in a generic way. The algorithm can process both raster data (image) and text extractions (match-ups files). The core optimization of the AC uses the Nelder-Mead method, specifically coded to handle all pixels of an image at once.

5.3.2 BGC model

The hydrodynamic part of the model is based on MOM5.1 (www.gfdl.noaa.gov/mom-ocean-model). MOM is a widely used model for global and regional applications. The FORTRAN code is available from (github.com/NOAA-GFDL/MOM6). The biogeochemical part is the model ERGOM (**E**cological **Re**G**i**onal **O**cean **M**odel). Code and the development tool CGT (code generation tool) is available from www.ergom.net.

5.4 CPU time

5.4.1 Atmospheric correction

The i/o functions should theoretically be fast but current implementation has to be reconsidered for OLCI in FR mode (memory issue). The pre-corrections (gas, glint, Rayleigh…) are processed by array operations in a negligible amount of time. The most consuming part relates to the Nelder-Mead optimization of the IOPs (AC with forward NN). However, the matrix multi-pixel implementation can process a full scene independently of its size, i.e. the CPU time does not dependent on the number of pixels. With 300 iterations, the processing of a scene requires less than 5 min on a single core.

S2 processing takes a slightly longer time due to resampling and meteo data reading. It is advised to resample all S2 data offline, once for all.

5.4.2 BGC model

The spatial resolution increase from 3n.m. to 1n.m. increased the computational effort 27-fold. In the current configuration at an Atos system (http://www.hlrn.de), the model needs at 2200 cores a wallclock time of 8h for one simulation year of the full spatial domain of the Baltic Sea. Available resources at high performance computing facilities clearly restrict the number of simulations. Especially for test and development simulations, the 3nm resolution is the preferred option.

6 Assumptions and limitations

6.1 Atmospheric correction

- The algorithm has been essentially designed and tested over the Baltic Sea and its performance over other marine and atmospheric corrections has not been assessed in this project.
- The correction for NO_2 is based on a climatology and should ideally be improved with concurrent NO_2 data (see Tzortziou et al., 2018). To our knowledge this is a general problem for any ocean colour processing, not solved to date. Using satellite observations of atmospheric NO_2 (e.g., TEMPO, TROPOMI, GEMS, Sentinel-4, Sentinel-5) has been very recently proposed but never tested so far (see proceedings of the IOCS 2019 meeting). Currently we advise to include the small case variability of NO_2 in the uncertainty formalism.
- The sun glint correction neglects effects of aerosols in the direct transmittance. This correction could be moved to the iterative retrieval of aerosol for improved performance.

6.2 BGC model

Uncertainties in CDOM estimates owing to an absorption – salinity relationship have been eliminated by introducing an explicit CDOM state variable. However, some limitations remain: CDOM decrease towards the North Sea is due to dilution and a decay process. Decay has been implemented in the model as a light dependent process. Beyond this dominating process other processes like bacterial activity or in situ production change the CDOM concentration. Furthermore, uncertainties in freshwater runoff and riverine CDOM load data propagate into the model domain.

7 References

B. A. Bodhaine, B.A., N. Wood, E. Dutton, J. Slusser (1999) On Rayleigh Optical Depth Calculations. J. Atmos. Ocean. Technol., 16, 1854–1861.

M. A. Branch, T. F. Coleman, and Y. Li (1999). A Subspace, Interior, and Conjugate Gradient Method for Large-Scale Bound-Constrained Minimization Problems. SIAM Journal on Scientific Computing, Vol. 21, Number 1, pp 1-23.

C. Brockmann, Doerffer, R., Peters, M., Stelzer, K., Embacher, S., Ruescas, A. (2016). Evolution of the C2RCC neural network for Sentinel 2 and 3 for the retrieval of ocean colour products in normal and extreme optically complex waters. European Space Agency, (Special Publication) ESA SP, SP-740

C. Cox, W. Munk (1954a). Measurement of the roughness of the sea surface from photographs of the Sun's glitter. J. Opt. Soc. Am. 44 (11), 838–850.

C. Cox, W. Munk (1954b). Statistics of the sea surface derived from sun glitter. J. Mar. Res. 13 (2), 198–227.

D. Ficek, T. Zapadk, J. Dera (2011). Remote sensing reflectance of Pomeranian lakes and the Baltic* doi:10.5697/oc.53-4.959, OCEANOLOGIA, 53 (4), pp. 959–970

J. Fischer, R. Preusker, R. Lindstrot (2010). OLCI ATBD Correction of the impact of the absorption of atmospheric gases. Issue 2.2, 04/08/2010, ref. S3-L2-SD-03-C03-FUB-ATBD_GaseousCorrection.

N. Fox (2010). A guide to expression of uncertainty of measurements. QA4EO-QAEO-GEN-DQK-006

S.M. Griffies (2004), Fundamentals of Ocean Climate Models, Princeton Univ. Press, Princeton, N. J.

L. Han, and Neumann, M. (2006). Effect of dimensionality on the Nelder–Mead simplex method. Optimization Methods & Software, Vol. 21, No 1, pp. 1-16.

T. Harmel, M. Chami, T. Tormos, N. Reynaud, P.A. Danis (2018). Sunglint correction of the Multi-Spectral Instrument (MSI)-Sentinel-2 imagery over inland and sea waters from SWIR bands. Remote Sensing of Environment 204, 308-321.

JCGM (2008). Evaluation of measurement data – Guide to the expression of uncertainty in measurement (GUM), Report, JCGM 100:2008

K. Kallio, Sampsa Koponen, Jenni Attila, Mikko Kervinen, Timo Pyhälahti, Carsten Brockmann, Tonio Fincke, Lena Kritten (2014). Sentinel-2 MSI in the Monitoring of Lakes and Coastal Waters in Finland: Spectral and Spatial Resolution Considerations. Sentinel-2 for Science Workshop, ESRIN, May 20-22 2014. http://seom.esa.int/S2forScience2014/files/02_S2forScience-WaterII_KALLIO.pdf

P. Kowalczuk, J. Olszewski, M. Darecki and S. Kaczmarek (2005). Empirical relationships between coloured dissolved organic matter (CDOM) absorption and apparent optical properties in Baltic Sea waters. International Journal of Remote Sensing, Vol. 26, No. 2, 20 January 2005, 345–370

J. C. Lagarias, Reeds, J.A., Wright, M.H., and Wright, P.E. (1998), Convergence Properties of the Nelder-Mead Simplex Method in Low Dimensions. SIAM J. Optim. 9, pp. 112–147.

J. Lenoble, M. Herman, J. Deuze, B. Lafrance, R. Santer, and D. Tanre (2007). A successive order of scattering code for solving the vector equation of transfer in the earth's atmosphere with aerosols. J. Quant. Spect. Radiat. Transf. 107, 479-507

S. Maritorena, , Fanton d'Andon, O.H., Mangin, A., Siegel, D.A (2010). Merged satellite ocean color data products using a bio-optical model: characteristics, benefits and issues. Remote Sens. Environ. 114, 1791–1804

Morel, A., Antoine, D. and B. Gentili (2002). Bidirectional reflectance of oceanic waters: Accounting for Raman emission and varying particle phase function, Appied Optics, 41, 6289-6306.

J. A. Nelder, and Mead, R., A Simplex Method for Function Minimization. The Computer Journal, 1965, 7, 308-313.

T. Neumann, Siegel, H., Gerth, M. (2015): A new radiation model for Baltic Sea ecosystem modelling. Journal of Marine Systems, Volume 152, December 2015, Pages 83-91, ISSN 0924-7963, http://dx.doi.org/10.1016/j.jmarsys.2015.08.001.

Sentinel-3 OLCI Marine User Handbook (2018), ref. EUM/OPS-SEN3/MAN/17/907205, available at https://www.eumetsat.int/website/wcm/idc/idcplg?IdcService=GET_FILE&dDocName=PDF_DMT_907205&RevisionSelectionMethod=LatestReleased&Rendition=WebF. Steinmetz, Deschamps, P.-Y., and Ramon, D. (2011). Atmospheric correction in presence of sun glint: application to MERIS. Optics Express, Vol. 19, Issue 10: 9783-9800.

M. Tzortziou, O. Parker, B. Lamb, J. R. Herman, L. Lamsal, R. Stauffer, N. Abuhassan (2018). Atmospheric trace gas (NO2 and O3) variability in South Korean coastal waters, and implications for remote Sensing of coastal ocean color dynamics. Remote Sensing, 10, 1587.

Van der Woerd, H. J., and R. Pasterkamp (2008). HYDROPT: A fast and flexible method to retrieve chlorophyll-a from multispectral satellite observations of optically complex coastal waters. Remote Sens. Environ. 112: 1795–1807

Q. Vanhellemont, G. Neukermans, K. Ruddick (2014). Synergy between polar-orbiting and geostationary sensors: Remote sensing of the ocean at high spatial and high temporal resolution. Remote Sensing of Environment 146, 49-62

P.J. Werdell, B.A. Franz, S.W. Bailey, G.C. Feldman, E. Boss, V.E. Brando, M. Dowell, T. Hirata, S.J. Lavender, Z-P Lee, H. Loisel, S. Maritorena, F. Mélin, T. S. Moore, T.J. Smyth, D. Antoine, E. Devred, O.H. Fanton d'Andon, and A. Mangin (2013). Generalized ocean color inversion model for retrieving marine inherent optical properties. Applied Optics vol. 52, no. 10.

J. Wolberg, (2006). Data Analysis Using the Method of Least Squares. Extracting the Most Information from Experiments. Springer-Verlag Berlin Heidelberg